Heat Generation and Transfer in Additive Friction Stir Deposition

Kendall P. Knight

Dissertation Submitted to the faculty of the Virginia Polytechnic Institute and State University in partial fulfillment of the requirements for the degree of

Doctor in Philosophy

In

Materials Science and Engineering

Hang Z. Yu, Chair

William T. Reynolds

Thomas Diller

Scott Huxtable

April 24, 2024

Blacksburg, VA

Keywords: Additive Friction Stir Deposition, Inverse Heat Transfer, Moving Heat Source, AA7050, Structural Repair

Heat Generation and Transfer in Additive Friction Stir Deposition

Kendall P. Knight

ABSTRACT

Additive friction stir deposition (AFSD) is an emerging solid-state additive manufacturing process that leverages the friction stir principle to deposit porosity-free material. The unique flow of material that allows for the transformation of bar stock into a near-net shape part is driven by the non-linear heat generation mechanisms of plastic deformation and sliding frictional heat generation. The magnitude of these mechanisms, and hence the total applied thermal power, implicitly depend on the thermal state of the system, forcing power input to become a dependent variable. This is not the case in other 3D printing methods; thermal power can be controlled independently. In this work, the heat generation in AFSD is explored, and its transfer is quantified. In particular, the time-dependent ratio between the amount of conduction into the AFSD tool versus into the substrate is quantified. It was found for the conditions tested with a single-piece AFSD tool, conduction up the tool was on the order of the conduction into the stir. For a more modern three-piece tool, the ratio between the tool and the substrate varied between 0.3-0.1. It was also found that traversing faster resulted in more heat flux into the substrate as would be expected by moving heat source modeling. The total heat generated was also quantified as being equal to between 60% and 80% of the mechanical spindle power depending on the tool type and the exact process conditions. That ratio was found to be time-invariant. At the same time, this changing heat flux ratio was shown to dramatically alter thermocouple measurements in the tool, showing the uncertainty of that method of process control. The contact state between the stir and the tool was treated as a thin conductive layer and a contact heat transfer coefficient was calculated on the order of 20 $\frac{kW}{m^2K}$. The limitations of this treatment were found to occur when a significant amount of the heat generation came from frictional heating rather than plastic deformation. This implies that any measurement conducted in the tool is related to the stir by a complex function driven by the state of the stir; showcasing the need for more well-understood in-situ monitoring. Finally, some of the ideas about thermal control are applied to a case study on the repair of corroded through holes using AFSD to restore fatigue life. It was found that modifying the thermal boundary conditions and applying active cooling at the end of the repair could improve the fatigue life drastically. This was due to less time spent in a thermally active region leading to less heterogeneous nucleation and less grain boundary nucleation. This more preferred microstructure morphology led to a change in the fracture mode and increased the number of cycles to crack initiation and the number of cycles after crack initiation.

Heat Generation and Transfer in Additive Friction Stir Deposition

Kendall P. Knight

GENERAL AUDIENCE ABSTRACT

Metal 3D printing of industrially relevant aluminum alloys is plagued with problems. Additive friction stir deposition seems well posed to overcome some of the problems associated with aluminum printing. Being able to 3D print these alloys with properties that are as good as traditional manufacturing offers a large potential cost and time savings over traditional manufacturing for the aerospace industry (e.g. Boeing, Lockheed Martin, U.S. Navy). For these components to be part of a plane, the manufacturer must prove the components were made the same way print-to-print regardless of the actual shape of the component being made. This dissertation focuses on the key metallurgical variable of temperature and explores how thermal energy is generated and where that energy goes in to the system. The key takeaway is, that without precise knowledge of the total heat generated and the entire thermal system, assurances about processing temperature cannot be made. An exploration of heat generation and metrics about its dispersion are presented. This is followed by a study on repairing structural components while changing the thermal system to understand its effects.

DEDICATION

This work is dedicated to my family and friends who supported me every step of the way.

ACKNOWLEDGMENTS

I would like to thank my advisor Dr. Hang Yu, associate professor of Materials Science and Engineering at Virginia Tech, for letting me explore ideas without reassurance of what they might bring. I appreciate the freedom and support I have been given throughout my time working with you.

I would like to thank my parents, Sarah Knight, and Pat Knight. Thank you for supporting me in whatever goal I selected.

There is no doubt I need to thank my good friend and colleague Greg Hahn. Nearly all this work, and plenty more that is not shown, was completed alongside him. Both of our dissertations benefited from the unknowable hours of brainstorming and bouncing ideas around.

I would like to thank the members of the Yu group at Virginia Tech who were always ready to help in whatever work needed to be done in the lab. I look forward to your continued success.

Table of Contents

1 Chapter 1: Introduction 1

1.1 Fundamentals of Conductive Heat Transfer 1

1.1.1 Introduction 1

1.1.2 Boundary Condition Types 1

1.1.3 Direct Solution 2

1.1.4 Inverse Heat Transfer 2

1.2 Additive Friction Stir Deposition 3

1.2.1 Methodology 3

1.2.2 Key Process Variables 4

1.2.3 Fundamental Metallurgy of 7xxx Series Aluminums 4

1.3 Dissertation Overview 4

Chapter 1 References 6

2 Chapter 2: A Simplified Heat Transfer System 13

1.1 Manuscript 1: Temperature Measurement of the Additive Friction Stir Deposition Through Inverse Heat Transfer 13

Abstract 13

Introduction 13

Theory 15

Materials and Methods 19

Results 21

Conclusions 30

Manuscript 1 References 31

3 Chapter 3: Unveiling Real-World Heat Transfer Dynamics 38

3.1 Manuscript 2: Traversal Heat Generation and Transfer in Additive Friction Stir Deposition of Aluminum Alloys 38

Abstract 38

Introduction 38

Materials and Methods 40

Results 43

Discussions 49

Conclusions 53

Manuscript 2 References 55

4 Chapter 4: Thermal Control of Solid-State Repair 62
4.1 Manuscript 3: Effect of Support Geometry on the AFSD Repair of Corroded AA7050 Through Holes 62
Abstract 62
Introduction 62
Materials and Methods 63
Results 66
Discussions 76
Conclusions 78
Manuscript 3 References 80
Appendix 1 87
5 Chapter 5: Conclusions and Future Work 88
5.1 Temperature Measurement 88
5.2 Tool Considerations 88
5.3 Heat Generation 89
5.4 Structural Repair and Active Cooling 90
5.5 Future Work 91

Attributions

Manuscript 1: *Temperature Measurement of the Additive Friction Stir Deposition Through Inverse Heat Transfer*

Author Contributions:

Kendall P. Knight wrote the original draft, performed relevant experiments, and conducted the analysis.

Greg D. Hahn assisted in experiments and data presentation.

Hang Z. Yu edited the manuscript.

Manuscript 2: *Traversal Heat Generation and Transfer in Additive Friction Stir Deposition of Aluminum Alloys*

Author Contributions:

Kendall P. Knight wrote the original draft, performed relevant experiments, and conducted the analysis.

Greg D. Hahn assisted in experiments and data presentation.

Hang Z. Yu edited the manuscript.

Manuscript 3: *Effect of Support Geometry on the AFSD Repair of Corroded AA7050 Through Holes*

Author Contributions:

Kendall P. Knight wrote the original draft, performed relevant experiments, and conducted the analysis.

Greg D. Hahn assisted in experiments and data presentation.

Luke Hagedorn assisted in experiments and edited the manuscript.

Mark Pandol assisted in experiments and edited the manuscript.

Hang Z. Yu edited the manuscript.

1 Chapter 1: Introduction

1.1 Fundamentals of Conductive Heat Transfer

1.1.1 Introduction

Thermodynamic theory in its simplest form expresses that a body can interact with its surroundings through the exchange of work and heat. The study of thermodynamics however is the study of end conditions, answering the question "What state does a process finish in?" The study of *how* a process exchanges heat energy with its surroundings along the accompanying rates is termed heat transfer [1]. Heat is transferred between bodies or within a body when a spatial temperature difference exists.

The amount of heat energy transferred per unit time per unit area is referred to as the heat flux. For a given spatial temperature field, if a family of iso-thermal contours is generated, the greatest temperature gradient at a point is normal to one of these curves. The fundamental law of heat conduction states that the heat flux is proportional to this gradient through a constant of proportionality known as thermal conductivity [2]. This quantity is a property of a given material and is expressed in metric units as $\frac{W}{mK}$. This value can vary from 0.17 $\frac{W}{mK}$ for gypsum board, 200 $\frac{W}{mK}$ for aluminum alloys, and 2300 $\frac{W}{mK}$ for diamond [1].

This temperature difference can either be termed steady or transient, where a transient temperature field varies through time. Thus, in a transient problem, the resulting heat transfer rates will also vary over time. Considering these transient effects forces consideration of the capacity of a material to store internal energy per unit mass. This is the material's specific heat capacity, specifically its specific heat at constant pressure C_p. It can be stated that the heat flux is proportional to the gradient of internal energy per unit volume [2]. With this consideration, the temperature distribution in one dimension through time can be expressed with the differential equation:

$$\frac{\partial^2 T}{\partial x^2} = \frac{1}{\alpha}\frac{\partial T}{\partial t} \tag{1}$$

Where T is the temperature, t is the time, x is the spatial coordinate, and α is the thermal diffusivity defined to be:

$$\alpha = \frac{k}{\rho C_p} \tag{2}$$

Where ρ is the density, k is the thermal conductivity and C_p is the specific heat capacity at constant pressure. The solution to Eq. 1 describes the function $T(x,t)$. To solve this boundary value problem, initial conditions and boundary conditions must be enforced. In many practical cases, the initial condition is taken to be uniform and at room temperature.

1.1.2 Boundary Condition Types

In heat transfer analysis, there are four kinds of boundary conditions.

1) Prescribed boundary temperature

In this condition, the solution is held to a particular value at the boundary. This is the simplest type of boundary condition but can be practically troubling since it implicitly applies enough energy to the system to make it true. This can lead to spurious results when analyzing things with a defined temperature, but limited capacity to hold themselves there (i.e. filament heaters).

2) Prescribed boundary heat flux
   The second type of condition is where the heat flux at a boundary is specified, often as a function of time. This condition is useful when describing known power input sources (e.g. power limited conduction heaters, laser heating).
3) Heat flux proportional to a temperature difference
   Conditions of the third kind correspond to situations where the heat flux is driven by a temperature difference between two mediums. This is often used in convection where the proportionality constant is the convection coefficient or in radiation problems where the heat flux is non-linearly proportional.
4) A temperature and heat flux equality
   The final condition is that of true body-to-body conduction where the contact surface is the same temperature, i.e. a "zero jump condition [3]" and the heat flux entering and exiting the boundary must be equivalent. In practice, this is modeled by numerically simulating the second contacting object whereas the first three conditions can be applied to a single object.

Of particular interest in this work are boundary conditions of the second kind, where the energy input per unit time on a body's face can be specified.

1.1.3 Direct Solution

Once boundary and initial conditions have been specified, the problem can be solved for the spatial temperature distribution through time. This can be accomplished either analytically for specific geometries and boundary conditions or numerically through the use of difference methods. In analytical cases, the solutions quickly become unwieldy. For example, the solution to one-dimensional conduction along a semi-infinite plane with a uniform initial temperature and a single prescribed temperature boundary condition is given as [2]:

$$T(x,t) = erf\left(\frac{x}{2\sqrt{(\alpha t)}}\right)(T_0 - T_b) + T_b \tag{3}$$

Where T_0 is the initial, uniform temperature, T_b is the constant boundary temperature that is greater than T_0, and *erf*() is the error function. For arbitrarily complex 3D geometries, the corresponding analytical solution becomes too cumbersome. From here the wanting analyst turns to numerical difference methods; in practice, the finite element method or the finite difference method are both implemented with automatic mesh generation available as commercial software codes such as COMSOL, or ANSYS. From here, using the code's implementation of the boundary conditions described above, the time-resolved temperature field is calculated. However, a very hard question to answer many times, is "What are the values of the boundary conditions?"

1.1.4 Inverse Heat Transfer

Many times, values of the temperature versus time are available for one or many points in the domain of interest without knowledge of the boundary conditions. The question then becomes

how can samples of the solution be used to estimate the boundary conditions that drove them. The process of reversing the heat equation is known as inverse heat transfer [4]. The problem is typically phrased as how can the time-dependent parameter of a known boundary condition type be estimated given that the other boundary conditions are known, and the temperature has been sampled at one or more locations through time. The methods for solving this problem vary widely from sequential methods [5] like the one used in this work, to digital filters [6], convolutions [7], neural networks [8], PID algorithms [9], and more [10]. Most often the boundary condition of interest is a heat flux versus time.

In this work the sequential method from Beck [5], [7] is employed, in 1, 2, and 3 dimensional cases. To paraphrase the method simplistically:

1) A temperature-time history is measured at one or more points.
2) A model of the geometry is constructed and run based on a guessed, constant, heat flux magnitude q. The model temperature at the points and times that have corresponding measurements is recorded and denoted T_q.
3) The model is re-run with the constant heat flux multiplied by $1 + \epsilon$ where ϵ is a small number on the order of 0.001. The temperatures at the relevant points and times are recorded again and denoted $T_{(1+\epsilon)}$.
4) A heat flux sensitivity is calculated based on the temperature change between the two runs. This sensitivity is defined generally as $\Phi = \frac{T_{(1+\epsilon)} - T_q}{\epsilon * q}$.
5) With this sensitivity calculated the heat flux can be estimated as $q_{(est)} = \frac{T_m - T_q}{\Phi} \Phi^2$

Essentially, the geometry's temperature response to a unit heat flux is quantified, and based on its actual temperature response the heat flux is estimated. This method proved to be somewhat computationally taxing but was extendable to two and three dimensions and gave answers that were able to be rectified with reality.

1.2 Additive Friction Stir Deposition

1.2.1 Methodology

A case where heat transfer plays a large role, is that of additive manufacturing (AM), especially metal AM where the process temperature is a key variable to the strength of the finished component. Of particular interest in this work is the novel solid-state AM process known as additive friction stir deposition (AFSD). This process leverages the friction stir principle to deposit fully solid material layer by layer without melting. This enables the deposition of materials that are susceptible to hot cracking, like 7xxx series aluminums [11], [12]. This process works by using a rotating tool with a square channel. Material is loaded into the channel and the tool is brought near a substrate to be printed on with an offset corresponding to the layer height. The material in the tool is forced downward into contact with the substrate while the tool is spinning at a rate on the order of 300 RPM. The downward pressure combined with the rotation generates frictional heat between the feedstock and the substrate. This heat leads to thermal softening and yielding of the feedstock. Once enough material has been yielded under the tool, the rate at which the feedstock is fed is increased and the tool begins moving along the substrate depositing material like fused filament fabrication.

Significant work has been undertaken to understand the thermal and metallurgical effects of AFSD [12], [13], [14], [15], [16], [17], [18], [19], [20], [21]. In short, the material under the tool exhibits a non-linear flow and heat generation response that is fully coupled to the tool and current state conditions such as strain rate and temperature. This complex processing causes many metallurgical effects such as embrittlement [12], abnormal grain growth [22], and anisotropy [23].

1.2.2 Key Process Variables

For a given material system, AFSD is controlled through a few different independent variables. These are:

1) Spindle rotation rate
2) Traversal velocity
3) Layer height
4) Feedstock input velocity

Through the fully coupled thermomechanical process, these variables in different, non-independent ways govern process outputs like the temperature field, thermal power, layer width, feedstock force, and spindle torque. The key distinction between AFSD and other AM processes like laser powder bed fusion, directed energy deposition, and fused filament fabrication is that the input thermal power is not an independent variable. There is a direct coupling of the current process's thermal state and the heat generation. In previous works, this coupling has been simplified to only consider the spindle rotation rate as the power input control variable [14], [24] but this assumption has other processing side effects such as too much total strain imparted to the work being deleterious to the properties [12]. Regardless of the degree of simplification used the fully coupled aspect presents a unique challenge to the control and monitoring of the process.

1.2.3 Fundamental Metallurgy of 7xxx Series Aluminums

Current military and civilian aviation is enabled by high strength-to-weight alloys used to construct the structural components of aircraft. The most prevalent metallic alloys are 7xxx series aluminums composed of Al, Mg, Zn, and Cu with other minor alloying additions[25]. The main alloy considered in this work is AA7050 which is composed of the main alloying elements with the addition of Zr. This precipitation hardened alloy utilizes a hierarchical microstructure with particles existing on several length scales. This alloy has a large fracture toughness and is fatigue resistant in its most common forms [26]. AA7050 is commonly deployed in a T7X temper giving it some corrosion resistance making it a prime candidate for aerospace structures for Naval aircraft [27].

1.3 Dissertation Overview

This dissertation aims to quantitatively investigate the heat generation and heat dispersion that takes place within the AFSD process and understand some of the effects of thermal control on a high-strength aerospace alloy.

Chapter 2 (Manuscript 1) shows the first application of inverse heat transfer on the AFSD process using a specially designed geometry. This work compares the heat generated to the spindle power, the effect of tool face type on the heat generated, and the time-dependent

conduction path. These ideas are combined into an operational understanding based on the contact heat transfer coefficient to estimate a bulk stir temperature from a calculated tool heat flux. This method provides a substrate and material agnostic method to begin to understand the actual processing temperature.

Chapter 3 (Manuscript 2) shows an extension of the ideas of Ch.2 to state-of-the-art tooling and more realistic printing scenarios. The effect of the tooling and its interplay with the processing variables is discussed, along with an analysis of the current state-of-the-art control scheme for AFSD. Finally, insights about heat generation mechanisms and bounds on the understanding of tool-stir friction are shown. It was found that a more modern tool with a modular design massively affects the thermal state of a print along with the distribution of heat energy. It was also found that embedded thermocouple was an unreliable way of understanding the thermal state of the stir.

Chapter 4 (Manuscript 3) focuses on a practical application of thermal control along with the use of AFSD for the repair of corroded through holes in AA7050 plate. It was found that the repair of this plate was agnostic to its flow boundaries but that active cooling of the print directly following deposition allowed for a highly extended fatigue life in the R=-1 loading condition. This work is compared with work completed by Hahn et. al. where active cooling was not used. Using TEM imaging, along with EBSD and optical imaging it was found that the material flow of the samples was nearly unchanged, but the precipitate morphology retained a more favorable configuration.

Chapters 2-4 have all been presented in a manuscript style in preparation for journal submission pending advisory review and publication of preceding papers.

Chapter 5 summarizes and draws overarching conclusions from this body of work. Future work to investigate the tool-stir friction states and material understanding are proposed and discussed.

Chapter 1 References

[1] F. P. Incropera and D. P. De Witt, “Fundamentals of heat and mass transfer, 2nd edition,” 1990. [Online]. Available: https://api.semanticscholar.org/CorpusID:94205714

[2] A. V. Lykov, *Analytical Heat Diffusion Theory*. Academic Press, 1968.

[3] R. Komanduri and Z. B. Hou, “Analysis of heat partition and temperature distribution in sliding systems,” *Wear*, vol. 251, no. 1–12, pp. 925–938, Oct. 2001, doi: 10.1016/S0043-1648(01)00707-4.

[4] “Inverse Heat Transfer: Fundamentals and Applications - Helcio R.B. Orlande - Google Books.” Accessed: Feb. 11, 2024. [Online]. Available: https://books.google.com/books?hl=en&lr=&id=xEMiEAAAQBAJ&oi=fnd&pg=PP1&ots=WDtHUe5bnd&sig=IfUktFDZnxIJf9XeOKco5BHMK8c#v=onepage&q&f=false

[5] J. V. Beck, B. Litkouhi, and C. R. S. Clair, “EFFICIENT SEQUENTIAL SOLUTION OF THE NONLINEAR INVERSE HEAT CONDUCTION PROBLEM,” *Numeri Heat Transf A Appl*, vol. 5, no. 3, pp. 275–286, 1982, doi: 10.1080/10407788208913448.

[6] N. Daouas and M. S. Radhouani, “A new approach of the Kalman filter using future temperature measurements for nonlinear inverse heat conduction problems,” *Numerical Heat Transfer, Part B: Fundamentals*, vol. 45, no. 6, pp. 565–585, Jun. 2004, doi: 10.1080/10407790490430598.

[7] J. V Beck, B. Blackwell, and C. R. S. C. Jr, *Inverse Heat Conduction: Ill-Posed Problems*, 1st edition. New York: Wiley-Interscience, 1985.

[8] H. Najafi and K. A. Woodbury, “Online heat flux estimation using artificial neural network as a digital filter approach,” *Int J Heat Mass Transf*, vol. 91, pp. 808–817, Dec. 2015, doi: 10.1016/J.IJHEATMASSTRANSFER.2015.08.010.

[9] S. Wan, P. Xu, K. Wang, J. Yang, and S. Li, “Real-time estimation of thermal boundary of unsteady heat conduction system using PID algorithm,” *International Journal of Thermal Sciences*, vol. 153, p. 106395, Jul. 2020, doi: 10.1016/J.IJTHERMALSCI.2020.106395.

[10] M. Zálešák, L. Klimeš, P. Charvát, M. Cabalka, J. Kůdela, and T. Mauder, “Solution approaches to inverse heat transfer problems with and without phase changes: A state-of-the-art review,” *Energy*, vol. 278, p. 127974, Sep. 2023, doi: 10.1016/J.ENERGY.2023.127974.

[11] H. Z. Yu, “Additive Friction Stir Deposition,” *Additive Friction Stir Deposition*, pp. 1–333, Jan. 2022, doi: 10.1016/C2020-0-01505-7.

[12] J. K. Yoder, H. Z. Yu, W. T. Reynolds, W. Cai, L. Li, and V. Blacksburg, “Origins of Embrittlement of an Al-Zn-Mg-Cu Alloy Post Additive Friction Stir Deposition,” Jan. 2023, Accessed: Sep. 15, 2023. [Online]. Available: https://vtechworks.lib.vt.edu/handle/10919/113012

[13] W. D. Hartley *et al.*, “Solid-state cladding on thin automotive sheet metals enabled by additive friction stir deposition,” *J Mater Process Technol*, vol. 291, 2021, doi: 10.1016/j.jmatprotec.2021.117045.

[14] J. K. Yoder, D. J. Erb, R. Henderson, and H. Z. Yu, “Closed-loop temperature controlled solid-state additive manufacturing of Ti-6Al-4V with forging standard out-of-plane tensile properties,” *J Mater Process Technol*, vol. 322, p. 118201, Dec. 2023, doi: 10.1016/J.JMATPROTEC.2023.118201.

[15] D. Z. Avery *et al.*, “Influence of Grain Refinement and Microstructure on Fatigue Behavior for Solid-State Additively Manufactured Al-Zn-Mg-Cu Alloy,” *Metall Mater Trans A Phys Metall Mater Sci*, vol. 51, no. 6, 2020, doi: 10.1007/s11661-020-05746-9.

[16] G. G. Stubblefield, K. Fraser, B. J. Phillips, J. B. Jordon, and P. G. Allison, “A meshfree computational framework for the numerical simulation of the solid-state additive manufacturing process, additive friction stir-deposition (AFS-D),” *Mater Des*, vol. 202, 2021, doi: 10.1016/j.matdes.2021.109514.

[17] B. J. Phillips *et al.*, “Microstructure-deformation relationship of additive friction stir-deposition Al–Mg–Si,” *Materialia (Oxf)*, vol. 7, p. 100387, Sep. 2019, doi: 10.1016/J.MTLA.2019.100387.

[18] K. C. Kincaid, D. W. MacPhee, G. G. Stubblefield, J. B. Jordon, T. W. Rushing, and P. G. Allison, “A Finite Volume Framework for the Simulation of Additive Friction Stir Deposition,” *J Eng Mater Technol*, vol. 145, no. 3, Jul. 2023, doi: 10.1115/1.4056642.

[19] N. Gotawala and H. Z. Yu, “Material flow path and extreme thermomechanical processing history during additive friction stir deposition,” *J Manuf Process*, vol. 101, pp. 114–127, Sep. 2023, doi: 10.1016/J.JMAPRO.2023.05.095.

[20] P. C. Metz *et al.*, “Heterogeneous microstructure development in additive friction-stir deposited Al-Mg-Si alloy,” 2024, doi: 10.1016/j.addma.2024.103989.

[21] B. A. Rutherford *et al.*, “metals Effect of Thermomechanical Processing on Fatigue Behavior in Solid-State Additive Manufacturing of Al-Mg-Si Alloy”, doi: 10.3390/met10070947.

[22] G. D. Hahn, K. P. Knight, N. Gotawala, and H. Z. Yu, “Additive friction stir deposition of AA7050 achieving forging-like tensile properties,” *Materials Science and Engineering: A*, vol. 896, p. 146268, Mar. 2024, doi: 10.1016/J.MSEA.2024.146268.

[23] M. B. Williams *et al.*, “Towards Understanding the Relationships between Processing Conditions and Mechanical Performance of the Additive Friction Stir Deposition Process,” *Metals 2023, Vol. 13, Page 1663*, vol. 13, no. 10, p. 1663, Sep. 2023, doi: 10.3390/MET13101663.

[24] G. R. Merritt, M. B. Williams, P. G. Allison, J. B. Jordon, T. W. Rushing, and C. A. Cousin, “Closed-Loop Temperature and Force Control of Additive Friction Stir

Deposition," *Journal of Manufacturing and Materials Processing*, vol. 6, no. 5, 2022, doi: 10.3390/jmmp6050092.

[25] R. Sanders and J. Staley, "A History of Wrought Aluminum Alloys and Applications," in *Properties and Selection of Aluminum Alloys*, ASM International, 2019, pp. 157–201. doi: 10.31399/asm.hb.v02b.a0006516.

[26] Battelle Memorial Institute., "Metallic Materials Properties Development and Standardization (MMPDS-2023)".

[27] E. A. Starke and J. T. Staley, "Application of modern aluminium alloys to aircraft," in *Fundamentals of Aluminium Metallurgy: Production, Processing and Applications*, Elsevier Ltd., 2010, pp. 747–783. doi: 10.1533/9780857090256.3.747.

[28] H. Z. Yu *et al.*, "Non-beam-based metal additive manufacturing enabled by additive friction stir deposition," *Scr Mater*, vol. 153, pp. 122–130, Aug. 2018, doi: 10.1016/j.scriptamat.2018.03.025.

[29] H. Z. Yu and R. S. Mishra, "Additive friction stir deposition: a deformation processing route to metal additive manufacturing," *Mater Res Lett*, vol. 9, no. 2, 2021, doi: 10.1080/21663831.2020.1847211.

[30] J. K. Yoder, R. J. Griffiths, and H. Z. Yu, "Deformation-based additive manufacturing of 7075 aluminum with wrought-like mechanical properties," *Mater Des*, vol. 198, Jan. 2021, doi: 10.1016/j.matdes.2020.109288.

[31] A. M. Vest, D. R. St-Pierre, S. Rock, A. M. Maniatty, D. J. Lewis, and S. J. A. Hocker, "Thermocouple Temperature Measurements in Selective Laser Melting Additive Manufacturing", Accessed: Feb. 11, 2024. [Online]. Available: http://www.sti.nasa.gov

[32] B. Müller, ; U Renz, B. Mü Ller, and U. Renz, "Development of a fast fiber-optic two-color pyrometer for the temperature measurement of surfaces with varying emissivities," *Review of Scientific Instruments*, vol. 72, no. 8, pp. 3366–3374, Aug. 2001, doi: 10.1063/1.1384448.

[33] A. Lerner *et al.*, "Laser Powder Bed Fusion thermal monitoring using optical fiber sensors: in situ measurements and modelling," *2023 Conference on Lasers and Electro-Optics Europe and European Quantum Electronics Conference, CLEO/Europe-EQEC 2023*, 2023, doi: 10.1109/CLEO/EUROPE-EQEC57999.2023.10232209.

[34] C. Krishna, P. Vallabh, and X. Zhao, "Melt pool temperature measurement and monitoring during laser powder bed fusion based additive manufacturing via single-camera two-wavelength imaging pyrometry (STWIP)," *J Manuf Process*, vol. 79, pp. 486–500, 2022, doi: 10.1016/j.jmapro.2022.04.058.

[35] B. Bevans *et al.*, "Heterogeneous sensor data fusion for multiscale, shape agnostic flaw detection in laser powder bed fusion additive manufacturing," *Virtual Phys Prototyp*, vol. 18, no. 1, Dec. 2023, doi: 10.1080/17452759.2023.2196266.

[36] J. Petrich, Z. Snow, D. Corbin, and E. W. Reutzel, “Multi-modal sensor fusion with machine learning for data-driven process monitoring for additive manufacturing,” *Addit Manuf*, vol. 48, p. 102364, Dec. 2021, doi: 10.1016/J.ADDMA.2021.102364.

[37] P. K. Rao, J. Liu, D. Roberson, Z. Kong, and C. Williams, “Online Real-Time Quality Monitoring in Additive Manufacturing Processes Using Heterogeneous Sensors,” *Journal of Manufacturing Science and Engineering, Transactions of the ASME*, vol. 137, no. 6, Dec. 2015, doi: 10.1115/1.4029823/374977.

[38] K. J. Colligan and R. S. Mishra, “A conceptual model for the process variables related to heat generation in friction stir welding of aluminum,” *Scr Mater*, vol. 58, no. 5, pp. 327–331, Mar. 2008, doi: 10.1016/j.scriptamat.2007.10.015.

[39] W. D. Hartley and S. W. Case, “Processing Mechanics of Additive Friction Stir Deposition.”

[40] S. H. Mousavi Anijdan, H. R. Madaah-Hosseini, and A. Bahrami, “Flow stress optimization for 304 stainless steel under cold and warm compression by artificial neural network and genetic algorithm,” *Mater Des*, vol. 28, no. 2, pp. 609–615, Jan. 2007, doi: 10.1016/J.MATDES.2005.07.018.

[41] K. A. Fraser, “Robust and efficient meshfree solid thermo-mechanics simulation of friction stir welding,” 2017.

[42] K. Kumar, C. Kalyan, S. V. Kailas, and T. S. Srivatsan, “An Investigation of Friction During Friction Stir Welding of Metallic Materials,” *Materials and Manufacturing Processes*, vol. 24, no. 4, pp. 438–445, Apr. 2009, doi: 10.1080/10426910802714340.

[43] A. F. Hasan, C. J. Bennett, P. H. Shipway, S. Cater, and J. Martin, “A numerical methodology for predicting tool wear in Friction Stir Welding,” *J Mater Process Technol*, vol. 241, pp. 129–140, Mar. 2017, doi: 10.1016/J.JMATPROTEC.2016.11.009.

[44] S. Mandal, J. Rice, G. Hou, K. M. Williamson, and A. A. Elmustafa, “Modeling and simulation of a donor material concept to reduce tool wear in friction stir welding of high-strength materials,” *J Mater Eng Perform*, vol. 22, no. 6, pp. 1558–1564, Jun. 2013, doi: 10.1007/S11665-012-0452-4/FIGURES/10.

[45] J. Zhang, P. Upadhyay, Y. Hovanski, and D. P. Field, “High-Speed Friction Stir Welding of AA7075-T6 Sheet: Microstructure, Mechanical Properties, Micro-texture, and Thermal History”, doi: 10.1007/s11661-017-4411-4.

[46] G. R. Merritt, M. B. Williams, P. G. Allison, J. B. Jordon, T. W. Rushing, and C. A. Cousin, “Closed-Loop Temperature and Force Control of Additive Friction Stir Deposition,” *Journal of Manufacturing and Materials Processing*, vol. 6, no. 5, Oct. 2022, doi: 10.3390/jmmp6050092.

[47] Z. T. Niu, H. Qi, Y. K. Ji, S. Wen, Y. T. Ren, and M. J. He, “Real-time reconstruction of thermal boundary condition of porous media via temperature sequence,” *International Journal of Thermal Sciences*, vol. 177, Jul. 2022, doi: 10.1016/j.ijthermalsci.2022.107570.

[48] D. Lu and C. Wang, “Three-dimensional temperature field inversion calculation based on an artificial intelligence algorithm,” *Appl Therm Eng*, vol. 225, May 2023, doi: 10.1016/j.applthermaleng.2023.120237.

[49] S. Motahar, “Experimental study and ANN-based prediction of melting heat transfer in a uniform heat flux PCM enclosure,” 2020, doi: 10.1016/j.est.2020.101535.

[50] C. Fieberg and R. Kneer, “Determination of thermal contact resistance from transient temperature measurements,” *Int J Heat Mass Transf*, vol. 51, no. 5–6, pp. 1017–1023, Mar. 2008, doi: 10.1016/j.ijheatmasstransfer.2007.05.004.

[51] A. Bejan and A. D. Kraus, *Heat transfer handbook*. J. Wiley, 2003.

[52] M. Nouari, B. Haddag, A. Moufki, and S. Atlati, “Investigation on the built-up edge process when dry machining aeronautical aluminum alloys,” *Machining of Light Alloys*, pp. 35–48, Aug. 2018, doi: 10.1201/B22153-2.

[53] R. Nandan, T. Debroy, and H. K. D. H. Bhadeshia, “Recent advances in friction-stir welding-Process, weldment structure and properties”, doi: 10.1016/j.pmatsci.2008.05.001.

[54] R. Nandan, G. G. Roy, T. J. Lienert, and T. Debroy, “Three-dimensional heat and material flow during friction stir welding of mild steel,” *Acta Mater*, vol. 55, no. 3, pp. 883–895, Feb. 2007, doi: 10.1016/J.ACTAMAT.2006.09.009.

[55] K. Fraser, L. I. Kiss, L. St-Georges, and D. Drolet, “Optimization of friction stir weld joint quality using a meshfree fully-coupled thermo-mechanics approach,” *Metals (Basel)*, vol. 8, no. 2, Feb. 2018, doi: 10.3390/MET8020101.

[56] S. Solhjoo, “Revisiting the Common Practice of Sellars and Tegart’s Hyperbolic Sine Constitutive Model,” *Modelling 2022, Vol. 3, Pages 359-373*, vol. 3, no. 3, pp. 359–373, Aug. 2022, doi: 10.3390/MODELLING3030023.

[57] G. G. Stubblefield *et al.*, “Ballistic Evaluation of Aluminum Alloy (AA) 7075 Plate Repaired by Additive Friction Stir Deposition Using AA7075 Feedstock,” *Journal of Dynamic Behavior of Materials*, vol. 9, no. 1, pp. 79–89, Mar. 2023, doi: 10.1007/s40870-022-00363-6.

[58] C. J. T. Mason *et al.*, “Process-structure-property relations for as-deposited solid-state additively manufactured high-strength aluminum alloy,” *Addit Manuf*, vol. 40, Apr. 2021, doi: 10.1016/j.addma.2021.101879.

[59] R. S. Mishra, R. S. Haridas, and P. Agrawal, “Friction stir-based additive manufacturing,” *Science and Technology of Welding and Joining*, vol. 27, no. 3. Taylor and Francis Ltd., pp. 141–165, 2022. doi: 10.1080/13621718.2022.2027663.

[60] R. S. Mishra and M. Komarasamy, *Physical Metallurgy of 7XXX Alloys*. Elsevier, 2016. doi: 10.1016/b978-0-12-809465-5.00002-7.

[61] M. Schöbel, P. Pongratz, and H. P. Degischer, "Coherency loss of Al 3(Sc,Zr) precipitates by deformation of an Al-Zn-Mg alloy," *Acta Mater*, vol. 60, no. 10, pp. 4247–4254, Jun. 2012, doi: 10.1016/j.actamat.2012.04.011.

[62] A. Zubelewicz, "Century-long Taylor-Quinney interpretation of plasticity-induced heating reexamined," *Scientific Reports 2019 9:1*, vol. 9, no. 1, pp. 1–7, Jun. 2019, doi: 10.1038/s41598-019-45533-0.

[63] V. L. Popov, "Thermal Effects in Contacts," *Contact Mechanics and Friction*, pp. 199–205, 2010, doi: 10.1007/978-3-642-10803-7_13.

[64] B. H., "Theoretical Study of Temperature Rise at Surfaces of Actual Contact under Oiliness Lubricating Conditions," *Proc. Instn. Mech. Engrs. (General discussion on lubrication and lubricants)*, vol. 2, pp. 222-, 1937, Accessed: Mar. 11, 2024. [Online]. Available: https://cir.nii.ac.jp/crid/1573668924965107328

[65] J. C. Jaeger and J. C. Jaeger, "Moving sources of heat and the temperature at sliding contacts," *Journal and proceedings of the Royal Society of New South Wales*, vol. 76, no. 3, pp. 203--224, May 1943, doi: 10.5962/p.360338.

[66] K. J. Zwick and M. Tate, "Flash Temperature Theory," *Encyclopedia of Tribology*, pp. 1182–1194, 2013, doi: 10.1007/978-0-387-92897-5_1312.

[67] D. G. Bansal and J. L. Streator, "A method for obtaining the temperature distribution at the interface of sliding bodies," *Wear*, vol. 266, no. 7–8, 2009, doi: 10.1016/j.wear.2008.08.019.

[68] M. Akbari, D. Sinton, and M. Bahrami, "Moving heat sources in a half space: Effect of source geometry," *Proceedings of the ASME Summer Heat Transfer Conference 2009, HT2009*, vol. 3, pp. 685–694, 2009, doi: 10.1115/HT2009-88562.

[69] R. Mendoza, "In-service Corrosion Issues in Sustainment of Naval Aircraft," 2012.

[70] R. Joey Griffiths, D. T. Petersen, D. Garcia, and H. Z. Yu, "Additive friction stir-enabled solid-state additive manufacturing for the repair of 7075 aluminum alloy," *Applied Sciences (Switzerland)*, vol. 9, no. 17, Sep. 2019, doi: 10.3390/app9173486.

[71] M. E. J. Perry, R. J. Griffiths, D. Garcia, J. M. Sietins, Y. Zhu, and H. Z. Yu, "Morphological and microstructural investigation of the non-planar interface formed in solid-state metal additive manufacturing by additive friction stir deposition," *Addit Manuf*, vol. 35, Oct. 2020, doi: 10.1016/j.addma.2020.101293.

[72] M. E. J. Perry *et al.*, "Tracing plastic deformation path and concurrent grain refinement during additive friction stir deposition," *Materialia (Oxf)*, vol. 18, Aug. 2021, doi: 10.1016/j.mtla.2021.101159.

[73] C. C. De Castro *et al.*, “Tool wear mechanisms and effects on refill friction stir spot welding of AA2198-T8 sheets,” *Journal of Materials Research and Technology*, vol. 20, pp. 857–866, Sep. 2022, doi: 10.1016/J.JMRT.2022.07.092.

[74] Q. Chu *et al.*, “On visualizing material flow and precipitate evolution during probeless friction stir spot welding of an Al-Li alloy,” *Mater Charact*, vol. 144, pp. 336–344, Oct. 2018, doi: 10.1016/J.MATCHAR.2018.07.026.

[75] “Wrought Aluminum Alloys: Atlas of Fractographs,” in *Fractography*, ASM International, 2018, pp. 414–439. doi: 10.31399/asm.hb.v12.a0000621.

2 Chapter 2: A Simplified Heat Transfer System

In this chapter, a study is presented that attempts the first measurement of the thermal power generation and heat energy distribution in AFSD. This is done through a simplified geometry with some assumptions about the tool and stir. The key assumption in this work is that the stir can be treated as 1) a direct thermal continuation of the substrate and 2) a thermal mass that is in static contact with the tool. With these assumptions and inverse heat transfer, several insights can be gained.

1.1 Manuscript 1: Temperature Measurement of the Additive Friction Stir Deposition Through Inverse Heat Transfer

Kendall P. Knight, Greg D. Hahn, Hang Z. Yu

Abstract

Additive Friction Stir Deposition (AFSD) is a novel solid-state manufacturing technique that combines aspects of additive manufacturing and friction stir welding, offering robust material deposition capabilities. The thermal dynamics within AFSD significantly influence as-printed and heat-treated material properties. The contact heat transfer coefficient (CHTC), a key parameter governing heat exchange at the tool-material interface, is vital for understanding these thermal dynamics. This paper makes the first reported measurement of the CHTC and investigates its relationship with processing parameters, tool geometry, and material system. Our findings indicate that the CHTC is approximately $10^4 \frac{W}{m^2 k}$ and remains unaffected by factors such as rotation rate or the choice between 6xxx and 7xxx series aluminums. Furthermore, the data obtained from these experiments can be utilized as input for both global-scale thermal models and control systems.

Keywords: Additive Friction Stir Deposition, thermal contact, heat generation, inverse heat transfer

Introduction

Additive manufacturing (AM) has revolutionized the production of complex and customized components, offering a promising avenue for enhancing material properties and structural integrity. Among the diverse array of AM techniques, Additive Friction Stir Deposition (AFSD) stands out as a formidable approach, as a novel solid-state process merging the advantages of both friction stir welding and additive manufacturing [28], [29]. AFSD allows for the layer-wise addition of material, imparting exceptional control over microstructure and mechanical properties [15]. These material properties are as good or better than forging standards providing a large impetus to understand and control the process [30].

In fusion-based additive manufacturing, understanding, and controlling sub-microsecond variations in melt pool temperature is crucial for optimizing processing parameters and predicting the formation of defects. This has been addressed by applying advanced monitoring techniques and tools, including ultra-fast thermocouple readings [31], high speed two wavelength pyrometry [32], and optical fiber sensing [33], mostly during laser powder bed fusion (LPBF). These methods have been designed to overcome LPBF's biggest challenges, specifically ultra-fast thermal changes, and the presence of vapor in the build chamber obscuring

IR images [34] and much work has been done to integrate them into a method to detect defects and wayward behavior [35], [36], [37]. In the same way, work must be done to create measurement methods tailored to overcome AFSD's major measurement challenges. These challenges include the small amount of emitted infrared radiation due to the low print temperature compared to LPBF and other fusion-based processes, the constantly changing surface emissivity of a deposition due to the free edge, and the large forces, torques, and deformation involved force thermocouples to be suitably removed from the region of interest to prevent damage.

In the realm of AFSD, understanding and optimizing the thermal aspects of the process are imperative for achieving high-quality depositions with good mechanical properties [12], [17], [21]. Much effort has been focused on simulating and understanding the thermo-mechanical conditions in the stirring material [16], [18], [19], [38], [39]. One of the central issues in modeling the stir, besides choosing the correct material model parameters which much study has been devoted to [40], [41], is the sensitivity to flow and thermal boundary conditions. Due to the fully coupled, non-linearity of the AFSD stir, a misunderstanding of a boundary condition can propagate into large changes in the rest of the model. When thermal boundary conditions change, the resulting energy balance can lead to nonlinear responses in the flow field and dependent variables such as power and torque. In the comparatively more mature process of friction stir welding (FSW) considerable effort has been devoted to understanding and modeling the metallurgical effects on temperature [20], [42], [43], [44]. One of the most crucial steps has been the introduction of a thermocouple into the welding tool [45]. This has allowed for sustained temperature measurements in the areas of interest during real welding trials.

In AFSD, putting a thermocouple into a tool has been replicated [46]. Central to understanding this measurement is the boundary condition of the deposit in contact with the tool. This is the contact heat transfer coefficient, a fundamental parameter that governs the heat transfer dynamics at the tool-material interface during deposition. The contact heat transfer coefficient is a key determinant influencing the thermal behavior of the system, affecting the amount of heat transferred out of the stir into the tool. This conduction, along with the conduction into the substrate, accounts for the vast majority of the thermal energy in the AFSD process for aluminum and copper alloys. The exception to this is titanium alloys, where the high deposition temperature makes radiation from the free side of the stir non-negligible.

In many models, conduction into the substrate is accounted for either by considering a large non-stirring heat sink with a convection coefficient [16], [39] or by directly applying a temperature-dependent convection coefficient to the stir, aiming for computational efficiency [19]. However, conduction into the tool is often not treated [16], [39] or simplified to a single convection coefficient [19]. This approach may not be accurate as any heat generated at the interface or in the stir can conduct into the tool or the substrate, with the ratio of the two only determined by external boundary conditions (i.e. those on the larger substrate and those at the tool), and material properties. Furthermore, an accurate understanding of the total power conduction into the tool and substrate is the only way to directly relate thermal power to mechanical power imparted by the tool.

In addition to these modeling practicalities, the amount of heat energy flowing into the tool is what drives the measured temperature for existing closed-loop control systems [24]. Therefore, understanding this heat transfer is imperative to understanding the dynamics of a control system. Additionally, the temperature of the stir heavily influences material properties and microstructure morphology [12], [14], [24].

To understand the unknown boundary conditions of the AFSD process the inverse heat transfer method is employed. The inverse heat transfer method consists of many techniques from a broad range of categories designed to estimate an unknown parameter of the heat transfer system based on other knowledge of the system and the temperature field [4], [10], [47]. These techniques include the use of sequential and exact matching techniques [5], digital filters [6], and machine learning approaches [8], [48], [49]. Some of these techniques have been adapted for use in online systems [9], [47] to estimate real-time data for process control. In general, these inverse techniques must use more sophisticated algorithms than the direct solution counterparts to contend with the ill-posed nature of the inverse heat transfer problem.

This paper aims to provide a measurement of the contact heat transfer coefficient in the context of AFSD, delving into its significance, influencing factors, measurement techniques, and implications on the final product. By examining the interplay between process parameters, material characteristics, and the heat transfer coefficient, this study seeks to shed light on avenues for optimizing AFSD control processes, improving material properties, and expanding the potential applications of this innovative additive manufacturing technique.

Theory

In the stationary AFSD process, the tool-substrate system can be simplified to a 1-dimensional heat transfer problem. This problem is shown graphically in Figure 1a. While there are predicted to be 3D temperature gradients in the stir it is useful to consider an effective temperature (T_e) that is the volumetric average temperature [18]. This effective temperature is useful as it represents the total driving force for heat flux into the tool and substrate. In this system, heat is generated in the stir by plastic deformation and friction. Heat can then flow into the substrate through conduction. Since the substrate and the stir are metallurgically bonded, the bottom boundary condition is uninhibited conduction [1], [2]. On top of the stir, heat can flow into the tool through conduction as well. Due to the lack of metallurgical bonding between the stir and the tool, conduction is inhibited by contact resistance. This contact resistance can be considered as an equivalent thin layer with a contact heat transfer coefficient (CHTC) h_f [50], [51]. Heat also dissipates from the stir through natural or forced air convection at its free edges, although this effect is much smaller compared to conduction, primarily due to the limited area of the stir exposed to the air. Radiation from the free faces of the stir also occurs; however, for aluminum, this is considered to be negligible. For materials like titanium and steel this can start to play a role, but this can be easily compensated for by using an iterative scheme.

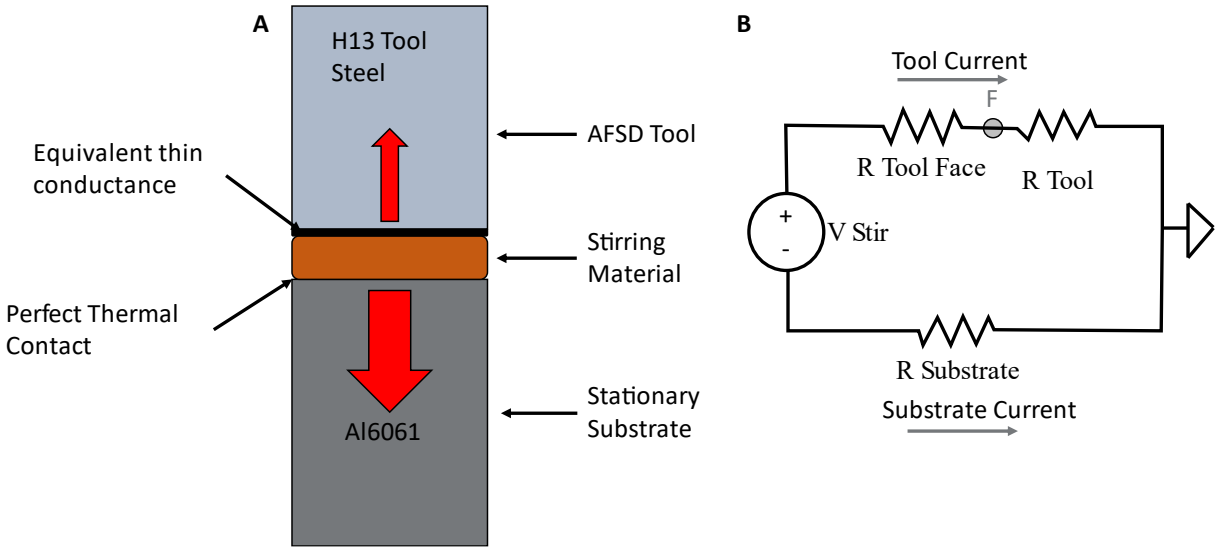

Figure 1 A) Diagram showing the 1D heat transfer simplification and physical orientation. Red arrows denote heat flux. B) Circuit analogy of the system shown in A.

The parallel conduction paths of the stir can be represented as a circuit diagram as shown in Figure 1B where the temperature is analogous to voltage, heat flux is analogous to current flow and thermal resistance is analogous to electrical resistance. The temperature of the stir (V_{stir}) can be calculated using the following relation if the tool face temperature (V_f), the tool face resistance (R_{Face}) taken as the reciprocal of the contact heat transfer coefficient (CHTC), and the tool current (I_{Tool}) are known.

$$V_{Stir} = I_{tool}R_{Face} + V_{Face} \tag{1}$$

Following the same logic, if the stir temperature is known and the face resistance is unknown, the face resistance can be calculated by the following rewrite.

$$R_{Face} = \frac{V_s - V_{Face}}{I_{Tool}} \tag{2}$$

Since R_{Face} is a function of the contact between the stir and the tool, it is a function of the stirred material, the tool material, and weakly of the processing conditions. If estimates can be made of the resistance value beforehand, then a temperature measurement only needs to give a value for the face temperature and the heat flux up the tool.

Equation 2 can be translated into heat transfer terms and is a rearranged form of the generalized convection equation.

$$h_{face}(t) = \frac{q_{face}(t)}{T_s(t) - T_{face}(t)} \tag{3}$$

Using inverse heat conduction methods, the time-varying heat flux boundary at the face of the tool (I_{Tool}), can be estimated from temperature measurements along the tool [7], [50]. In this work the function specification method with multiple temperature sensors and arbitrary future time steps was used with $q = C$ [7]. To determine the sensitivity to heat flux at each sensor location a transient 1-dimensional finite volume (FV) method is used. This model employed a 100-millisecond timestep with an element size of 30 μm. This sensitivity to heat flux, ϕ, at a

given point in space *i* at a given time τ, with a single future timestep is defined below by Beck [7]:

$$\phi_{i,\tau} = \frac{\widehat{T_{i,\tau}} - \overline{T_{i,\tau}}}{\epsilon * q_g} \tag{4}$$

Where $\overline{T_{i,\tau}}$ is the temperature at point *i* when the domain has been subjected to a step heat flux of $q_g = 10{,}000 \frac{W}{m^2}$ until τ time. $\widehat{T_{i,\tau}}$ is the temperature at point *i* when the domain is subjected to a heat flux of $(1+\epsilon)q_g$ until τ time, where $\epsilon = .01$.

In this work, the sensitivity is calculated by running the transient finite volume model first with a nominal face heat flux guess of 10,000 $\frac{W}{m^2}$ then with the (1+ ϵ) guess of 10,100 $\frac{W}{m^2}$. The temperature at each sensor location is then calculated at each sample time for both runs using the FV model. This calculation step is considered the forward step. The sample times in the model correspond to the measurement times in the experiment. At each location and time, a sensitivity is calculated, and the measured temperature is compared with the calculated temperature from the nominal run. Based on the temperature difference at each point and its corresponding sensitivity, each point then yields a heat flux estimation. The final heat flux estimation at each time is then taken as a combination of these point-wise estimations based on Beck et. al. eq. 4.4.24 [7].

The FV model used for the tool accounts for known boundary conditions, material properties, and the geometry of the tool. In this work the tool is modeled as an H13 tool steel cylinder with a cross-sectional area based on the diameter of the tool (38.1mm) minus the area of the feed rod channel (10.1mmx10.1mm) this cross-section can be seen in Figure 2A. Out-of-plane convection along the length of the tool is considered, with a static convection coefficient (h_{Side}).

In addition to conduction up the tool, there is conduction up the 9.5mm x 9.5mm aluminum feed rod in the center of the tool. This feed rod is mechanically keyed inside the tool as shown in Figure 2B. Since the contact area between the feed rod and the feed rod channel is relatively small, the heat transfer between the tool and the feed rod can be simplified as convection with a coefficient (h_{Feed}). The feed rod is explicitly modeled with a second FV model where any convective heat transfer from the feed rod must go to the corresponding point along the tool. To enforce a heat flux boundary condition on the tool face, a ghost element is used. This element's temperature is changed relative to the second to enforce the correct amount of heat flux coming into the model. Since the feed rod is more conductive than the tool, enforcing the same heat flux boundary condition is non-physical. The first element of the feed rod model is then enforced to be the tool model's ghost element temperature since the temperature the tool face and the feed rod face experience are the same. On the backside of both models, a convection boundary condition is applied to model the effect of the tool attaching to the larger machine, and the feed rod being in contact with the machine pushrod. The entire model is illustrated by a cross-section view in Figure 2C.

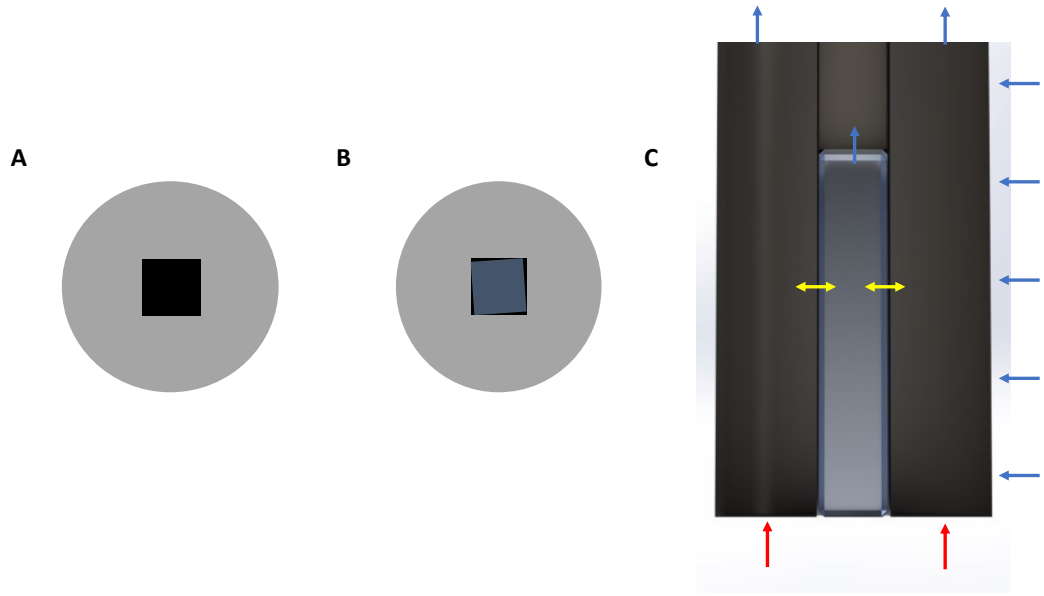

Figure 2 A) Cross section of the MELD R2 tool showing the location of the channel (black). B) Diagram showing how the feed rod (blue-grey) is keyed into the tool. C) Schematic showing the relative locations and heat transfer paths of the tool model.

This model accurately reflects the thermal system of the MELD R2 print head and with it, accurate sensitivity to heat flux can be calculated. The temperature along the tool can now be measured through time to determine the thermal history of each point. At each point, the temperature change between timesteps is calculated and the sensitivities are applied to estimate the heat flux at the face. It is important to note that the sensitivity for each measurement point along the tool rapidly drops as the point becomes farther from the face. Measurements in the first few millimeters are the most important, and any measurement farther than approximately 10mm from the face contains little information about the current heat flux.

Finally, the inverse heat conduction algorithm is used to make a whole domain temperature estimation based on the estimated heat flux as illustrated in Figure 3A. This predicted temperature is readily compared against the measured data to understand the accuracy of the heat flux estimation like the representative timestep shown in Figure 3B. The estimation over the entire domain also provides a good estimate of the tool face temperature, as the measurement points are slightly farther back. This estimation is superior to any type of regression curve fit since it has been informed by the physics of the problem.

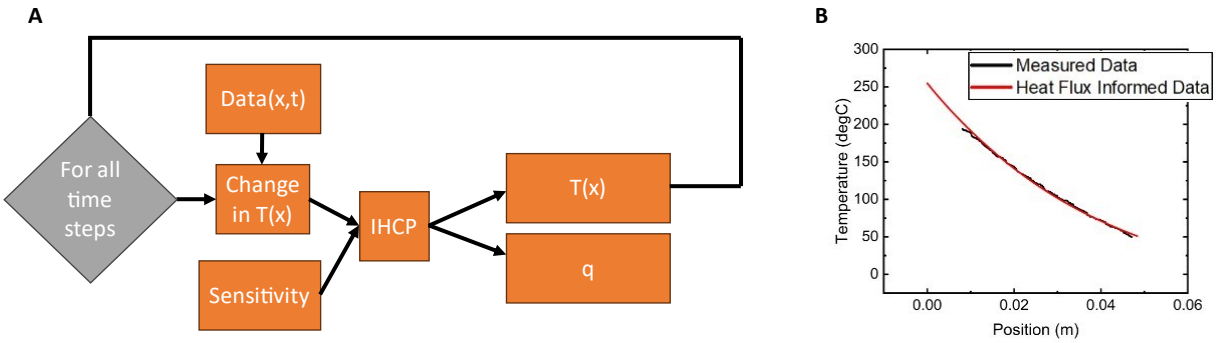

Figure 3 A) Graphical outline of the IHC algorithm. B) Measured Data vs data generated from the IHC algorithm along the length of the substrate at a given timestep.

From the inverse heat conduction algorithm, I_{tool} and V_{face} have been estimated. The only variable needed to understand the face resistance is the stir temperature. If a suitable geometry is selected, where the 1-D assumption holds and measurements very near the stir are possible, then the same principle of using the IHC algorithm described above is possible. If the domain of the substrate model is considered as extending halfway into the stir (0.5mm) then the stir temperature can be estimated using the whole domain estimation procedure explained above.

Since the radius of the stir changes as more material is added over time, the effective area across which the heat flux is applied changes as well. Because the IHC model is 1-D, it is assumed that heat is applied uniformly across the cross-section. To correct the estimation, the estimated heat flux needs to be scaled after the estimation by the changing radius, which can be done using the conservation of energy principle:

$$q_{real}(t) = \frac{q_{est}(t) * A_{tool}}{A_{stir}(t)} \tag{5}$$

The radius of the stir is readily calculated from the conservation of mass or measured via the side camera. While the changing radius of the stir does induce a 2D thermal field, the diametral Biot number of the tool is low enough to neglect this effect. Considering the tool as a solid cylinder, a worst-case scenario, the Biot number is given by:

$$Bi = \frac{h_{side} D}{k} = \frac{15 \frac{W}{m^2 K} * 0.0381 m}{24 \frac{W}{mK}} = 0.023 \tag{6}$$

where h_{side} is the convection coefficient on the side of the tool, D is the diameter of the tool, and k is the thermal conductivity of the H13 tool steel that the tool is manufactured from. With all relevant variables calculated for each timestep, the contact resistance can be calculated for each timestep. In the next sections, the exact methods and geometries used will be shown. Once the contact resistance has been calculated for a given tool-material combination the temperature of the stir can be estimated from a measurement of the tool alone.

Materials and Methods

To experimentally measure the contact resistance between the tool and stir, the geometry shown below in Figure 4A was created out of solid AA6061-T6 and AA7075-T6. This geometry has the

same diameter as the tool in a long enough length away from the base to facilitate IR imaging. A corresponding 1D, transient FV model was developed, with a convection coefficient of 10 $\frac{W}{m^2K}$ applied to the outside, and conduction on the bottom approximated as convection with a coefficient of 25 $\frac{W}{m^2K}$. The model was simpler than the one discussed for the tool since it did not need to include an internal channel. This model used the same 100 millisecond timestep with an element size of 15 µm. The geometry was clamped onto the steel bed of an R2 Meld Machine (Meld Manufacturing, Christiansburg, USA), as shown in Figure 4B. The deposition was carried out using a 9.5mm x 9.5 mm x 50mm feed rod made of the same material as the substrate. All depositions were conducted for 90s, with a layer height of 1mm, and a material feed rate of 0.21 mm/s. The three variables that were altered were the type of tool used, the rotation rate of the tool, and the substrate material. The tool options included either four small, 2.2mm high protrusions on the face (Figure 4C) or a featureless design (Figure 4d), referred to as the "pinned" tool and the "featureless" tool, respectively. The material was either AA6061 or AA7075. For clarity, in this paper, "featureless AA6061" refers to the processing of AA6061 using a featureless tool. The featureless AA6061 case was considered the baseline and was conducted at 250, 350, 450, 550, and 650 RPM. All other combinations of conditions were conducted at 350, 450, and 550 RPM, except for the pinned AA7075 case where the rotations rates were 250, 350, and 450 RPM. This lower rotation rate for AA7075 with protrusions is of more industrial interest. During each deposition, the machine's rotational power, rotational torque, and feed rod actuator force were recorded at a frequency of 1Hz from the control system. However, a machine malfunction on the 250 RPM, AA7075 print with the protrusion tool resulted in the machine data record not being captured. As a result, this data was discarded. After collection, the remaining data was converted to metric units, and the baseline power draw was subtracted out, resulting in only the power required by the deposition being shown.

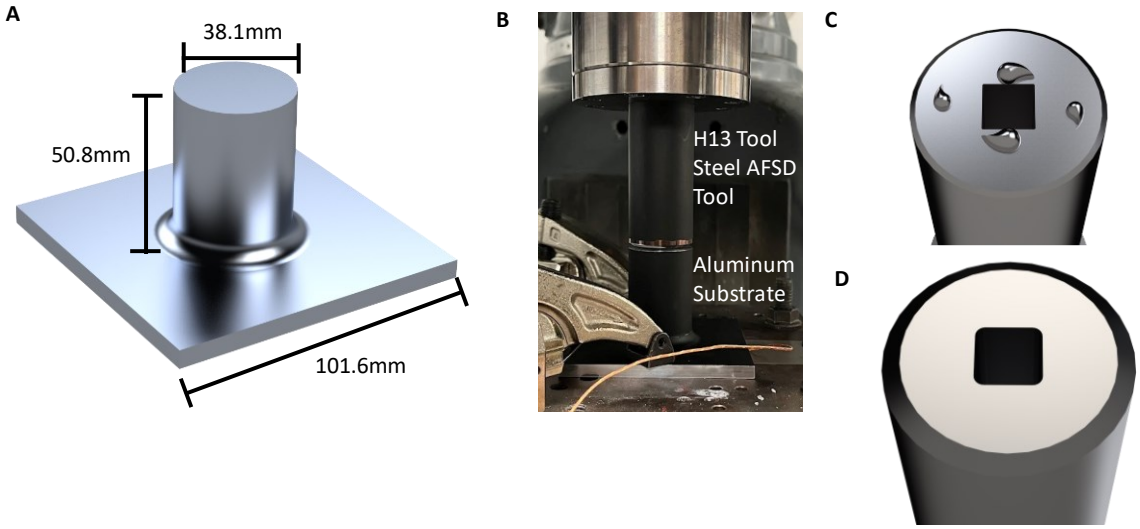

Figure 4 A) Substrate geometry used for this work. The diameter of the post exactly matches the tool diameter. Geometry was made from a single piece of material. B) Physical test setup on the R2 MELD machine. C) Rendering of the pinned tool showing the four 2.2mm high teardrop-shaped protrusions. D) Rendering of the featureless tool.

During each test, the temperature was measured with two TIM VGA thermal cameras (Micro-Epsilon, Raleigh NC), one for the tool and the other for the substrate. These cameras gave a resolution of 6 pixels per mm on both the tool and the substrate. Both the H13 tool steel AFSD tool and the substrate were painted with high-temperature thermographic paint that has a known emissivity (Lab IR, Morseova, Czech Republic). This paint, combined with the low diametral Biot number, provided confidence in the temperatures recorded, reflecting the areas of interest.

After conducting the experiments, the data from the thermal cameras was exported using MATLAB at a frame rate of 10Hz. The temperature along the centerline of the substrate and tool was collected for each time step and averaged laterally across ten pixels to minimize the uncorrelated random error found in each thermal camera pixel. The temperature profile was then related to the true position using known distances and references. Following this extraction, the IHC algorithm was used to estimate the CHTC between the stir and the tool.

Results

The temperature estimation for the entire domain, produced by the IHC algorithm, can be compared to the measured data at each timestep. A representative timestep (38 seconds into the print) is shown for the tool and the substrate in, Figure 5A and Figure 5B, respectively. The good agreement seen in each profile lends confidence to the CHTC estimates and the heat flux estimates the CHTC is based on. Any discrepancy would suggest that the underlying Inverse Heat Conduction Problem (IHCP) algorithm may not fully capture the physics at play, indicating a mismatch with the Finite Volume (FV) model assumptions. This trend of the predicted temperature matching the measured temperature is emulated for all other results.

Looking at the temperature through time of the first position of the substrate which corresponds to the centerline of the stir, the featureless and pinned tool can be compared in Figure 5c and Figure 5d respectively. Data has been trimmed from the end of each print corresponding to when the substrate deformed away from the tool. This deformation was caused by a combination of continued thermal softening and increasing downforce forcing the substrate to yield away from the tool. The stronger AA7075 takes longer to reach a critical limit than the AA6061, leading to a longer time series plot. This deformation event effectively ends each experimental trial as it skews the thermal measurement by changing the viewing angle and skews the machine data and process conditions by reducing the pressure in the stir. The featureless tool initially exhibits positive concavity due to the total volume of the stir increasing. This volumetric increase leads to more total deformation and therefore more total heat generation. Following this there is an inflection to negative concavity; as the material heats up it becomes easier to deform, producing less heat. This behavior is asymptotic to the solidus point of the material (AA6061 ~580 °C). This is contrasted by the pinned tool where the bulk of the heat is generated in the first few seconds. This heat generation is due to the protrusions on the face of the tool piercing into the substrate by ~1mm and displacing material rapidly. This displaced material is constrained by the face of the tool and forced to be deformed again in a cyclic pattern. The grooves left over from the protrusion interaction can be seen in Figure 5e. The temperature approaches the same asymptote due to the same mechanism as the featureless tool hence the similar maximum temperatures.

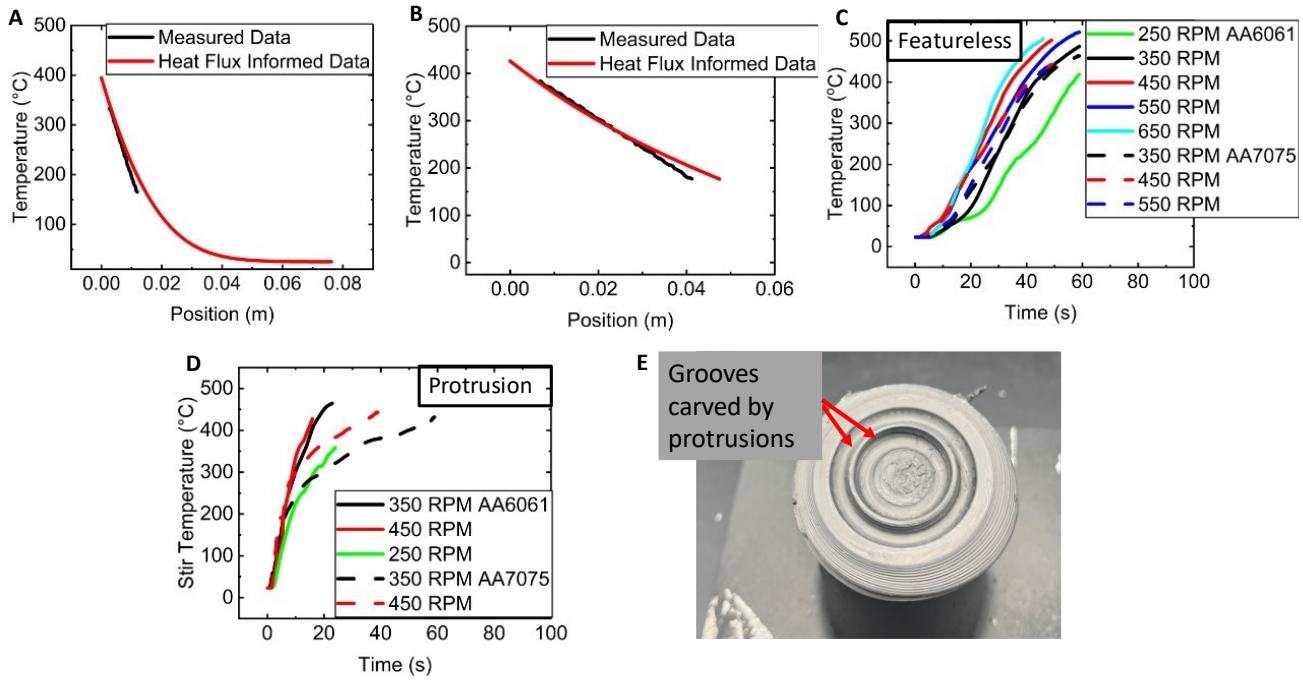

Figure 5 A) Representative time step of the tool, showing measured temperature along its length and the temperature estimated by IHC. Note that the length of the measured data corresponds to the amount of the tool that was visible to the IR camera. This length is somewhat short to increase the number of pixels per mm. B) The same time step of the substrate, depicting the measured temperature and the temperature predicted by IHC. C) Estimated temperature of the vertical centerline of the stir as a function of time for the featureless tool. AA6061 prints are shown in a solid line and AA7075 are shown with dashed lines. D) Temperature of the vertical centerline of the stir as a function of time for the pinned tool. AA6061 prints are shown in a solid line, while AA7075 prints are depicted with dashed lines. E) Photograph of a pinned print showing the grooves cut into the substrate and left behind. The top of the substrate has been painted for clarity.

By utilizing the IHC algorithm to determine temperature and heat flux, the CHTC can be estimated over time. In Figure 6A and Figure 6B the CHTC through time for AA6061 and AA7075 printed with a featureless tool is shown for each rotation rate. Data has been trimmed at the beginning of the print, as there is a period when the feed rod is spinning but not stirring. The data has some fluctuation over time, which is likely attributed to noise in the underlying temperature measurements. This data is contrasted with the purple dashed reference lines shown in A and B. These lines represent the CHTC needed to achieve a 1 °C difference across the boundary at the peak tool heat flux of 2500 $\frac{kW}{m^2}$. While it is clear the CHTC is very high it is far from perfect. Figure 6C illustrates the average of each point, indicating no discernible trend with rotation rate. The error bars represent the maximum and minimum values within the center 10-second interval.

The observed high Contact Heat Transfer Coefficient (CHTC) is likely due to the flowing metal being able to fill many of the surface irregularities that cause imperfect thermal contact. When comparing the values in this work to stationary aluminum-steel contact data from Fieberg &

Kneer [50], as shown in Figure 6D, it becomes apparent that the Contact Heat Transfer Coefficient (CHTC) from this work is on the same scale as high-pressure stationary contact.

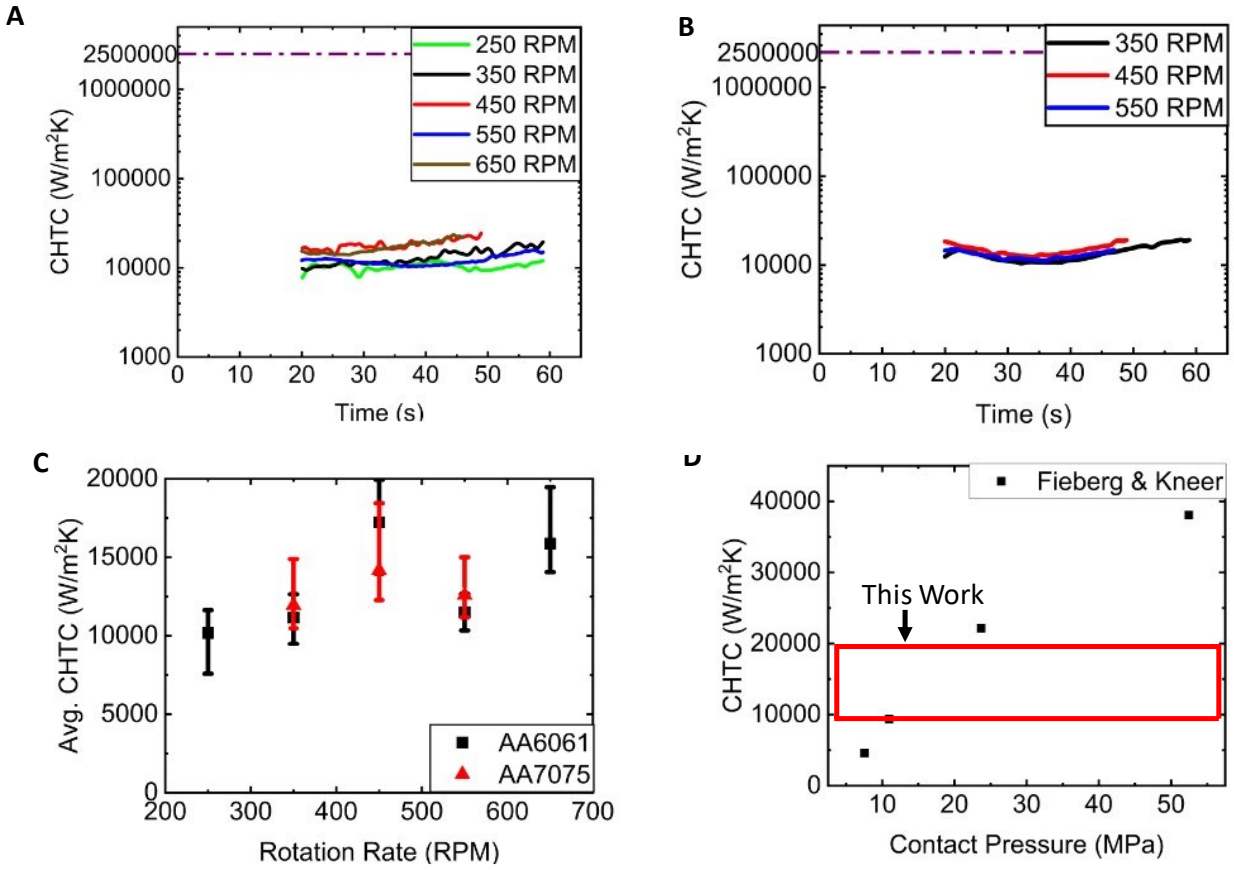

Figure 6 A) Contact Heat Transfer Coefficient (CHTC) vs time for featureless AA6061. The Purple dashed line represents the CHTC needed for a 1 °C temperature difference across the boundary at 2500 $\frac{kW}{m^2}$ of heat flux. B) CHTC vs time for featureless tool AA7075. C) Average CHTC for AA6061 and AA7075 with minimum and maximum error bars. D) The CHTC compared to a stationary aluminum-steel interface under pressure. Data from Fieberg and Kneer.

With the baseline of the featureless tool established, and a degree of confidence given to the results, the effects of the pinned tool can be examined. The CHTC vs time for the pinned tool compared to the featureless tool is shown in Figure 7. For the pinned tool, the CHTC starts low and then increases steadily as more material is added to the print. This is contrasted with the featureless tool, where once the stir is established (which is when most of the heat energy is released) the CHTC remains relatively constant.

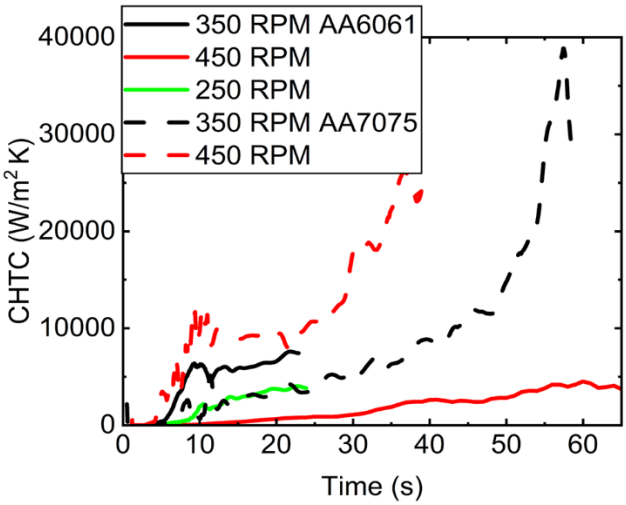

Figure 7) CHTC for each of the protrusion prints illustrates the much larger variation over time.

The machine power, which is analogous to thermal power as shown later, is depicted over time alongside a representative CHTC curve for the 350RPM AA7075 case in Figure 8A. In the pinned print, the power starts at around 2000W, and this energy is converted to heat by the pins before the stirring begins. This is contrasted with the 350RPM AA7075 featureless print shown in Figure 8B. The power starts at nearly zero and increases as the volume of material increases. This is illustrated graphically in Figure 9. The spike in power at around 20 seconds corresponds to the material yielding and beginning to properly stir, generating heat. Since all the heat at the beginning of the print is volumetric heat generation created by the pins deforming the substrate, this heat is preferentially conducted in the substrate rather than crossing into the pin and up the tool. A proposed mechanism for this decreased conduction is as follows: 1) the area connecting the pin to the rest of the tool is small, totaling 72mm^2 or 6.3% of the total surface area of the tool. This small area makes rapid heating of the tool difficult and limits the power input. 2) The pins are likely each pushing a “plug” of material around, and the actual deformation heating is taking place at the front of this plug. This phenomenon would be similar to the “built-up edge” seen in metal cutting processes driven by high friction, high pressure, and high sliding velocity [52].

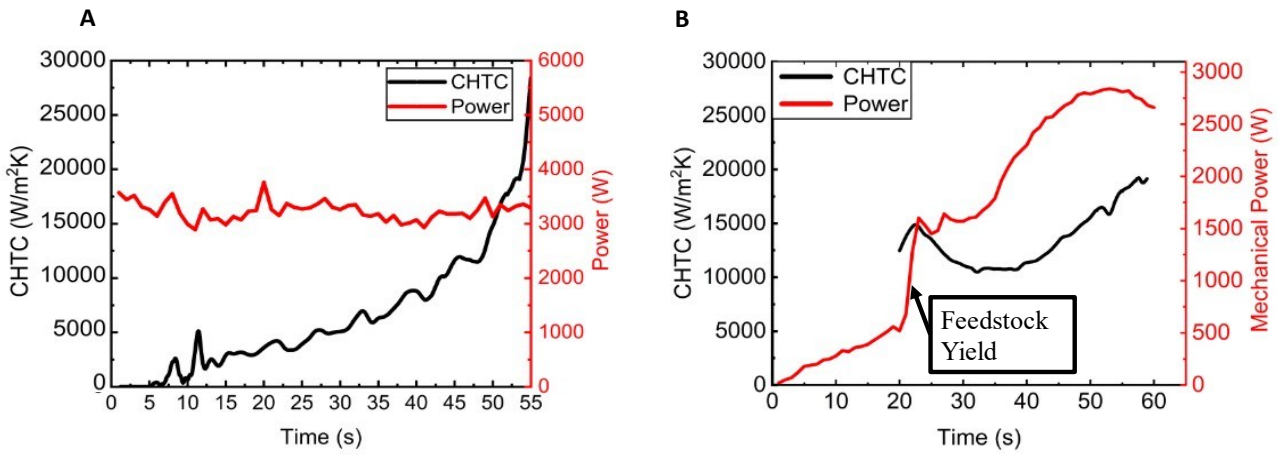

Figure 8 A) CHTC and power profiles for the pinned 350RPM, AA7075 case. B) CHTC and power profiles for the featureless 350RPM, AA7075 case.

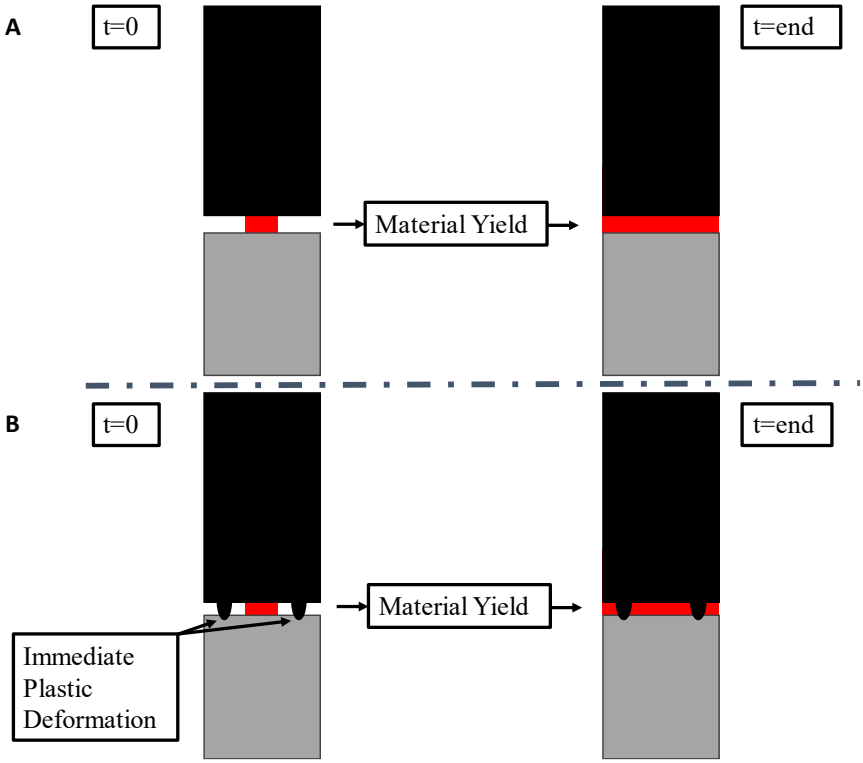

Figure 9 Graphical illustration of the start and end of the print for the A) Featureless tool and B) Protrusion tool.

Figure 10 presents the heat flux for both the substrate and tool, along with the ratio of the two (tool heat flux divided by substrate heat flux), for featureless (A-C) and pinned (D-F) configurations. Looking at the featureless substrate and tool it is apparent they follow similar trends over time. This is likely driven by the addition of material underneath the tool, which increases up to a maximum and then decreases as both the substrate and tool are thermally saturated, allowing the stir to retain the heat already contained in it. The trends in the heat flux

for both the substrate and tool roughly correlate with the rotation rate, but there are some variations. Analyzing the evolution 30 seconds into the stir, for example, reveals a rising heat flux in the AA6061 substrate case (Figure 10a), following this progression: 250RPM -> 350RPM -> 550RPM -> 450RPM -> 650RPM. This pattern is also observed in the tool heat flux. In AA7075, the difference is smaller, but the trend persists. Examination of the ratio between these two trends in Figure 10C indicates that they fluctuate between 1 and 1.5, depending on the rotation rate. Examining the increasing ratio, indicating more heat transfer into the tool, at 30 seconds, the ratio follows this trend: 250RPM -> 350RPM->550RPM-> 450RPM≈650RPM. Considering all these factors together, the total heat generation does not solely depend on the rotation rate, even when all other variables are kept constant. Additionally, the ratio of heat flux (indicating the tendency of the heat to move either up the tool or down the substrate) is not solely determined by rotation rate. What is likely happening is a combination of the two heat generation mechanisms of AFSD: friction between the deposit surface and the tool, or volumetric heat generation due to bulk deformation of the entire deposited region. The precise nature of this interplay is beyond the scope of this study but is likely influenced by changes in the pressure state, flow stress, and frictional contact state all fully coupled with the temperature at each point within the stir. The featureless prints may be experiencing a different combination of heat generation mechanisms forcing more heat into the tool. Shifting focus to the pinned prints, a completely different trend emerges. The substrate data presented in Figure 10D is limited because the outside of the substrate deforms, leading to early termination of analysis. However, the recorded heat flux magnitude is on the same order of magnitude as the featureless case. The trend observed in the prints is markedly different from the featureless. The heat flux begins at a high level due to the immediate generation of heat by pin interaction, rather than solely from feed rod friction and yielding and later the volumetric heat generation picks up. This is illustrated in Figure 11. The tool heat flux is significantly smaller than that of featureless prints (Figure 10E vs Figure 10B), resulting in a heat flux ratio of 0.4 to 0.5. This suggests that the substrate receives roughly twice the energy as the tool, most likely due to the challenge of heat conduction through the pins, which traps the heat generated in the stir. It is important to note that the ratios presented here are only applicable to the specific tool, material, and geometry combination used in this calculation. In friction stir welding this ratio is often simplified to[53]:

$$R = \frac{\left(k_{tool}\rho_{tool}\, c_{p,\,tool}\right)^{0.5}}{\left(k_{sub}\rho_{sub}\, c_{p,sub}\right)^{0.5}} \tag{7}$$

When appropriate values for this system are applied to this equation the value comes out to be 0.42. This is very similar to the values seen in Figure 10F. Since this equation is based on differences in the heat conduction of the two materials it may be that the protrusion tool is experiencing less of the tool-stir frictional heat generation which matches the idea that the protrusions force additional plastic flow. This effect will need to be investigated further with other tools.

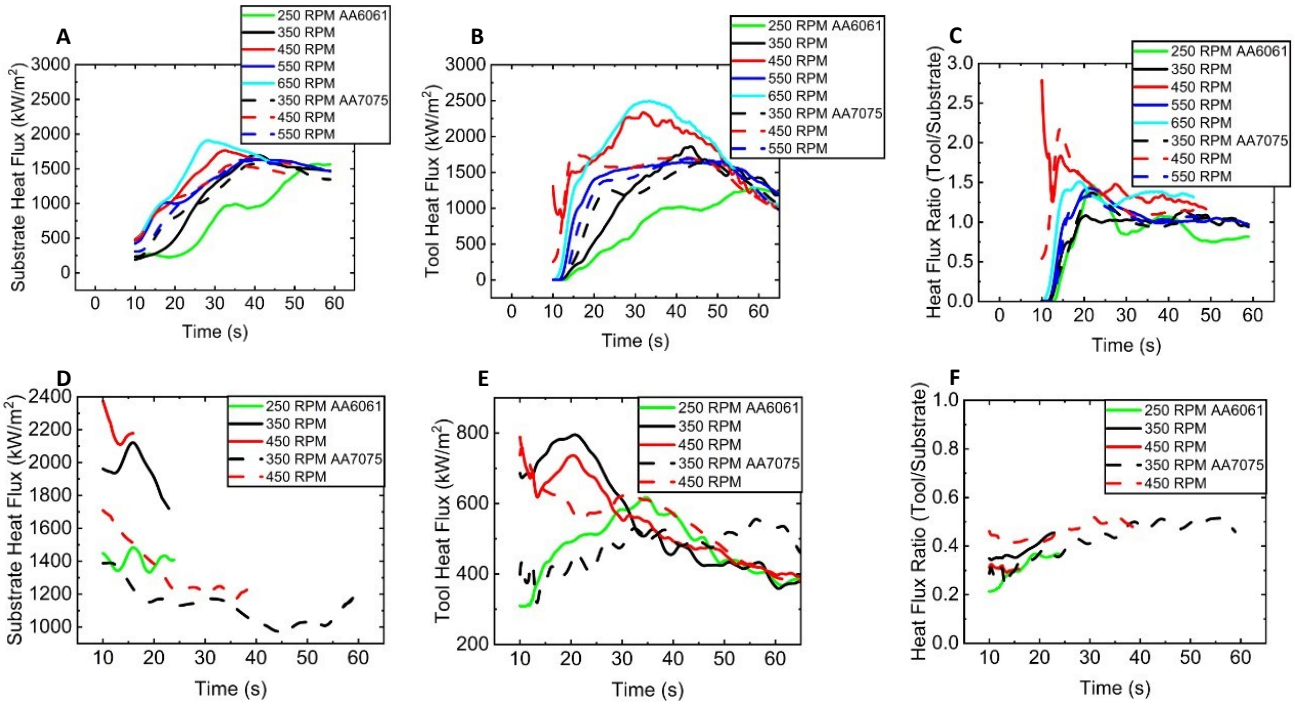

Figure 10 A) Substrate and B) Tool heat flux vs. time for featureless AA6061 and AA7075 prints. C) Ratio of featureless tool heat flux divided by substrate heat flux vs time. D) Substrate and E) Tool heat flux vs. time for pinned AA6061 and AA7075 prints. F) Ratio of pinned tool heat flux divided by substrate heat flux vs time.

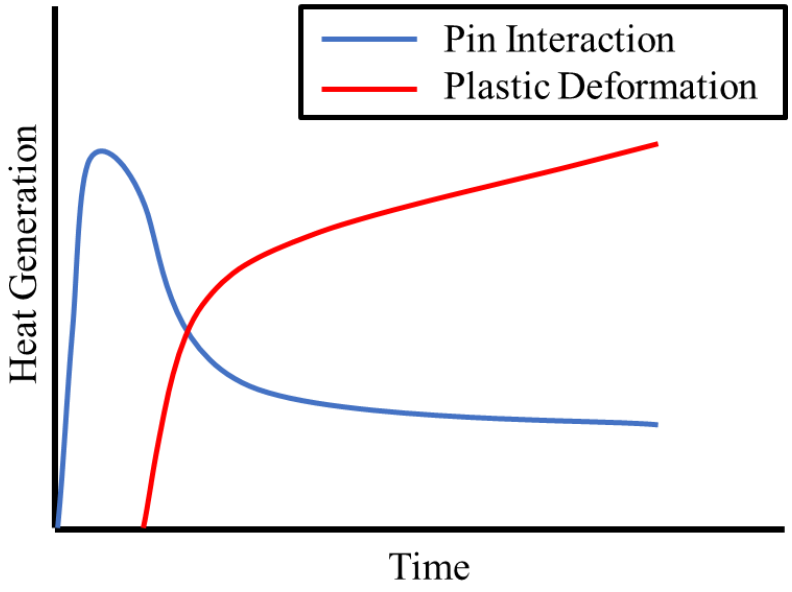

Figure 11 Illustration of the two heat generation mechanisms for the protrusion tool where at first the protrusions interacting with the substrate produce most of the heat and then the volumetric heating from plastic deformation takes over.

By summing the predicated heat flux both into the substrate and into the tool, multiplied by the area, the total thermal power of the print can be calculated. Comparing this thermal power over time to the baseline-corrected machine power vs time helps understand the efficiency by which mechanical power is converted to thermal power. Figure 12A shows the average and standard deviation of the ratio of thermal power to mechanical power for the featureless tool. Of particular interest in this graph is the AA7075, since those experiments, on average, lasted longer, providing more data in the stirring regime. While a ratio close to one is expected, the remaining energy not converted to heat is believed to go directly to the microstructure in the form of recrystallization. This consistent ratio presents a step forward in this modeling AFSD. In global models, where the heat generation of the stir is not explicitly calculated, the modeled input power can be directly linked to experimental data using the coefficient given here, eliminating the need to estimate the percentage of heat generation. However, assuming that the total power into the deposit is a constant fraction of the machine power is erroneous. The heat can move into either the tool or substrate and the ratio is driven by the total heat transfer state of the print, as shown in Figure 10C and Figure 10F. In local AFSD models, where heat generation is explicitly calculated, it is possible to compare the total heat generation to experimental data. The total heat generation is readily available from a model; however, it is much less so from an actual deposition. To the best of the author's knowledge, this is the first reported quantification of the total heat generated. Looking at Figure 12B, the machine power vs stir temperature for a featureless tool is shown. The power starts very near zero due to the absence of downforce, which results in minimal frictional heat generation. Analyzing the pinned tool power ratio in Figure 12C, we observe a similar trend with more scatter. Moving to the machine power vs temperature plot in Figure 12D, a distinct difference is evident between the pinned and featureless tools. The machine power is initially high as the pins contact the substrate, leading to machining and small amounts of heat flux flow, as shown in the early times of Figure 10D. Despite the temperature beginning to asymptotically slow, the power remains constant. This behavior is attributed to the deformation of a unit of material becoming easier, yet the volume of the stir continues to increase.

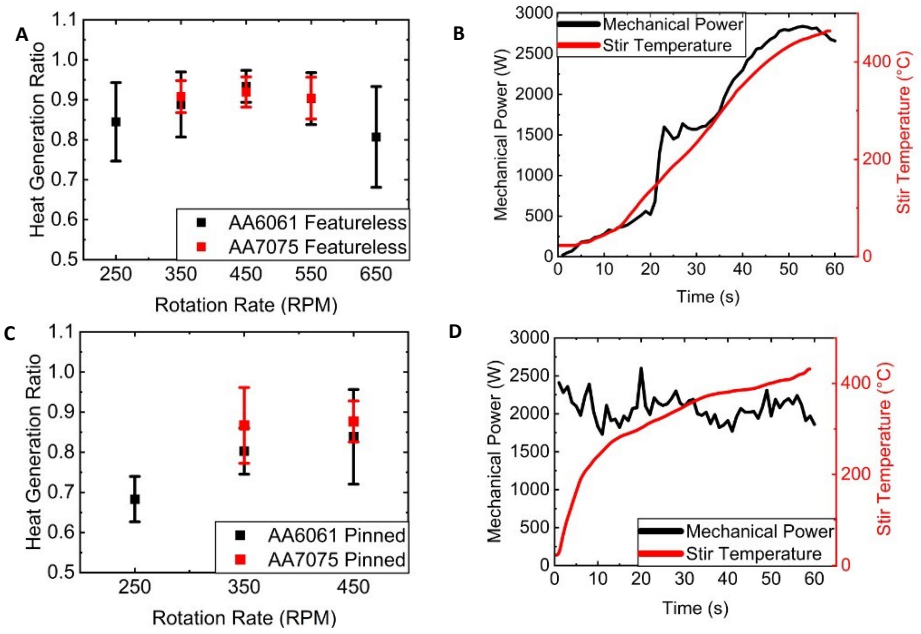

Figure 12 A) Ratio of thermal power to mechanical power for each of the featureless prints. B) Mechanical power vs stir temperature for the 350RPM featureless, AA6061 print. C) Ratio of thermal power to machine power for the pinned prints. D) Mechanical power vs stir temperature for the 350RPM pinned, AA7075 print.

It is also important to consider that the power and temperatures observed in this experiment are influenced by the test geometry and tool used. This process is fully coupled, meaning that any alteration in the boundary conditions can lead to non-linear and often unpredictable changes in the flow state. To better understand and illustrate this effect, it is helpful to examine a temperature-controlled stir experiment using the same geometry. This setup involves a thermocouple in the tool that reads the temperature and adjusts the rotation rate accordingly. As discussed earlier, increasing the rotation rate leads to a higher temperature.[14], [24]. If during a steady state stir the bottom boundary condition is changed to be much more diffusive (e.g. water is poured onto the bottom or cold air is blown) the amount of energy leaving the stir through the bottom will increase. This will decrease the amount of energy going into the tool thus lowering the temperature read by the thermocouple and causing the rotation rate to increase. At the same time, the energy leaving the substrate will make the stir colder and therefore more resistant to flow and requiring more torque to drive the same rotation rate. This increase in torque and rotation rate leads to an increase in power delivered to the stir thus raising its temperature before the heat has time to sufficiently diffuse away. This cycle will continue until the material reaches a new steady state which is governed by the non-linear flow stress and heat generation response of the flowing material all while being influenced by any time-varying thermal conditions. These ideas still hold for a rotation rate-controlled print but are less intuitive. Given these ideas, the notion that power is directly proportional to stir temperature must be discarded. In the AFSD process spindle torque and by extension power are dependent variables that are driven by rotation rate, thermal boundary conditions, and material properties. Without a complete understanding of the time-dependent thermal conditions imparted by a moving heat source on a

finite plate and the constant addition of material the control or modeling of the flow in AFSD is not possible since they are driven by the thermal conditions at all times. This idea of control is further complicated if any emergent phenomena change a boundary condition (i.e. residual stress, changing convective boundary, thermal soak).

Conclusions

In this work, we have shown the first estimates of the contact heat transfer coefficient between the stir and the tool in an AFSD deposition. This coefficient is critical to understanding the heat transfer dynamics in the process. With this, an understanding of the heat distribution between the tool and the substrate can be understood with pure conduction.

With these CHTCs determined for this tool-material system, the effective temperature is readily estimated using only information contained in the tool. The experiments outlined in this work serve as a calibration that only needs to be done once for each tool-material system of interest. Since there was little variation with rotation rate, it is likely in an industrial setting only one would be needed. It is possible that other alloy systems like copper or titanium may have rotational dependencies but that is easily determined by a similar set of experiments to this work.

We have also shown the first estimate of total thermal power vs machine power in the AFSD process. This relatively consistent ratio typically varies around 0.9 allows for the calculation of total thermal power entering a deposition based on the motor power. This quantity will be of great use to the modeling community especially when coupled with the knowledge of the CHTC.

The end use for this type of measurement is as the input to a closed-loop control system. How well this control system will work is dependent on the sensitivity of the measurement to changes in the temperature of the stir. This sensitivity is directly related to the proximity of the tool temperature measurement to the stir and the sensitivity rapidly decays as the measurement becomes farther away. For these experiments, the measurements were taken starting 1mm above the tool face. Using the multiple temperature sensors with multiple future timesteps algorithm described in Beck et. al. allows for most of the random errors to be canceled out. What remains is low frequency, correlated error related to the camera. Further work is necessary to understand the detection limits of a controller of this type.

Since the experiments shown in this work are stationary depositions, work needs to be completed to determine how traversal may affect the CHTC. Since almost no print of industrial interest is stationary, this is a critical experiment to move these techniques from the lab to the manufacturing floor. Additionally, a thermal comparison between a print completed with this type of temperature measurement system and the current state of the art will be important to begin to understand the metallurgical differences imparted. Finally, work will need to be done to adapt the FV model in this work to one that can handle the current state-of-the-art three-piece tools for MELD machines.

Manuscript 1 References

[1] F. P. Incropera and D. P. De Witt, “Fundamentals of heat and mass transfer, 2nd edition,” 1990. [Online]. Available: https://api.semanticscholar.org/CorpusID:94205714

[2] A. V. Lykov, *Analytical Heat Diffusion Theory*. Academic Press, 1968.

[3] R. Komanduri and Z. B. Hou, “Analysis of heat partition and temperature distribution in sliding systems,” *Wear*, vol. 251, no. 1–12, pp. 925–938, Oct. 2001, doi: 10.1016/S0043-1648(01)00707-4.

[4] “Inverse Heat Transfer: Fundamentals and Applications - Helcio R.B. Orlande - Google Books.” Accessed: Feb. 11, 2024. [Online]. Available: https://books.google.com/books?hl=en&lr=&id=xEMiEAAAQBAJ&oi=fnd&pg=PP1&ots=WDtHUe5bnd&sig=IfUktFDZnxIJf9XeOKco5BHMK8c#v=onepage&q&f=false

[5] J. V. Beck, B. Litkouhi, and C. R. S. Clair, “EFFICIENT SEQUENTIAL SOLUTION OF THE NONLINEAR INVERSE HEAT CONDUCTION PROBLEM,” *Numeri Heat Transf A Appl*, vol. 5, no. 3, pp. 275–286, 1982, doi: 10.1080/10407788208913448.

[6] N. Daouas and M. S. Radhouani, “A new approach of the Kalman filter using future temperature measurements for nonlinear inverse heat conduction problems,” *Numerical Heat Transfer, Part B: Fundamentals*, vol. 45, no. 6, pp. 565–585, Jun. 2004, doi: 10.1080/10407790490430598.

[7] J. V Beck, B. Blackwell, and C. R. S. C. Jr, *Inverse Heat Conduction: Ill-Posed Problems*, 1st edition. New York: Wiley-Interscience, 1985.

[8] H. Najafi and K. A. Woodbury, “Online heat flux estimation using artificial neural network as a digital filter approach,” *Int J Heat Mass Transf*, vol. 91, pp. 808–817, Dec. 2015, doi: 10.1016/J.IJHEATMASSTRANSFER.2015.08.010.

[9] S. Wan, P. Xu, K. Wang, J. Yang, and S. Li, “Real-time estimation of thermal boundary of unsteady heat conduction system using PID algorithm,” *International Journal of Thermal Sciences*, vol. 153, p. 106395, Jul. 2020, doi: 10.1016/J.IJTHERMALSCI.2020.106395.

[10] M. Zálešák, L. Klimeš, P. Charvát, M. Cabalka, J. Kůdela, and T. Mauder, “Solution approaches to inverse heat transfer problems with and without phase changes: A state-of-the-art review,” *Energy*, vol. 278, p. 127974, Sep. 2023, doi: 10.1016/J.ENERGY.2023.127974.

[11] H. Z. Yu, “Additive Friction Stir Deposition,” *Additive Friction Stir Deposition*, pp. 1–333, Jan. 2022, doi: 10.1016/C2020-0-01505-7.

[12] J. K. Yoder, H. Z. Yu, W. T. Reynolds, W. Cai, L. Li, and V. Blacksburg, “Origins of Embrittlement of an Al-Zn-Mg-Cu Alloy Post Additive Friction Stir Deposition,” Jan. 2023, Accessed: Sep. 15, 2023. [Online]. Available: https://vtechworks.lib.vt.edu/handle/10919/113012

[13] W. D. Hartley *et al.*, “Solid-state cladding on thin automotive sheet metals enabled by additive friction stir deposition,” *J Mater Process Technol*, vol. 291, 2021, doi: 10.1016/j.jmatprotec.2021.117045.

[14] J. K. Yoder, D. J. Erb, R. Henderson, and H. Z. Yu, “Closed-loop temperature controlled solid-state additive manufacturing of Ti-6Al-4V with forging standard out-of-plane tensile properties,” *J Mater Process Technol*, vol. 322, p. 118201, Dec. 2023, doi: 10.1016/J.JMATPROTEC.2023.118201.

[15] D. Z. Avery *et al.*, “Influence of Grain Refinement and Microstructure on Fatigue Behavior for Solid-State Additively Manufactured Al-Zn-Mg-Cu Alloy,” *Metall Mater Trans A Phys Metall Mater Sci*, vol. 51, no. 6, 2020, doi: 10.1007/s11661-020-05746-9.

[16] G. G. Stubblefield, K. Fraser, B. J. Phillips, J. B. Jordon, and P. G. Allison, “A meshfree computational framework for the numerical simulation of the solid-state additive manufacturing process, additive friction stir-deposition (AFS-D),” *Mater Des*, vol. 202, 2021, doi: 10.1016/j.matdes.2021.109514.

[17] B. J. Phillips *et al.*, “Microstructure-deformation relationship of additive friction stir-deposition Al–Mg–Si,” *Materialia (Oxf)*, vol. 7, p. 100387, Sep. 2019, doi: 10.1016/J.MTLA.2019.100387.

[18] K. C. Kincaid, D. W. MacPhee, G. G. Stubblefield, J. B. Jordon, T. W. Rushing, and P. G. Allison, “A Finite Volume Framework for the Simulation of Additive Friction Stir Deposition,” *J Eng Mater Technol*, vol. 145, no. 3, Jul. 2023, doi: 10.1115/1.4056642.

[19] N. Gotawala and H. Z. Yu, “Material flow path and extreme thermomechanical processing history during additive friction stir deposition,” *J Manuf Process*, vol. 101, pp. 114–127, Sep. 2023, doi: 10.1016/J.JMAPRO.2023.05.095.

[20] P. C. Metz *et al.*, “Heterogeneous microstructure development in additive friction-stir deposited Al-Mg-Si alloy,” 2024, doi: 10.1016/j.addma.2024.103989.

[21] B. A. Rutherford *et al.*, “metals Effect of Thermomechanical Processing on Fatigue Behavior in Solid-State Additive Manufacturing of Al-Mg-Si Alloy”, doi: 10.3390/met10070947.

[22] G. D. Hahn, K. P. Knight, N. Gotawala, and H. Z. Yu, “Additive friction stir deposition of AA7050 achieving forging-like tensile properties,” *Materials Science and Engineering: A*, vol. 896, p. 146268, Mar. 2024, doi: 10.1016/J.MSEA.2024.146268.

[23] M. B. Williams *et al.*, “Towards Understanding the Relationships between Processing Conditions and Mechanical Performance of the Additive Friction Stir Deposition Process,” *Metals 2023, Vol. 13, Page 1663*, vol. 13, no. 10, p. 1663, Sep. 2023, doi: 10.3390/MET13101663.

[24] G. R. Merritt, M. B. Williams, P. G. Allison, J. B. Jordon, T. W. Rushing, and C. A. Cousin, “Closed-Loop Temperature and Force Control of Additive Friction Stir

Deposition," *Journal of Manufacturing and Materials Processing*, vol. 6, no. 5, 2022, doi: 10.3390/jmmp6050092.

[25] R. Sanders and J. Staley, "A History of Wrought Aluminum Alloys and Applications," in *Properties and Selection of Aluminum Alloys*, ASM International, 2019, pp. 157–201. doi: 10.31399/asm.hb.v02b.a0006516.

[26] Battelle Memorial Institute., "Metallic Materials Properties Development and Standardization (MMPDS-2023)".

[27] E. A. Starke and J. T. Staley, "Application of modern aluminium alloys to aircraft," in *Fundamentals of Aluminium Metallurgy: Production, Processing and Applications*, Elsevier Ltd., 2010, pp. 747–783. doi: 10.1533/9780857090256.3.747.

[28] H. Z. Yu *et al.*, "Non-beam-based metal additive manufacturing enabled by additive friction stir deposition," *Scr Mater*, vol. 153, pp. 122–130, Aug. 2018, doi: 10.1016/j.scriptamat.2018.03.025.

[29] H. Z. Yu and R. S. Mishra, "Additive friction stir deposition: a deformation processing route to metal additive manufacturing," *Mater Res Lett*, vol. 9, no. 2, 2021, doi: 10.1080/21663831.2020.1847211.

[30] J. K. Yoder, R. J. Griffiths, and H. Z. Yu, "Deformation-based additive manufacturing of 7075 aluminum with wrought-like mechanical properties," *Mater Des*, vol. 198, Jan. 2021, doi: 10.1016/j.matdes.2020.109288.

[31] A. M. Vest, D. R. St-Pierre, S. Rock, A. M. Maniatty, D. J. Lewis, and S. J. A. Hocker, "Thermocouple Temperature Measurements in Selective Laser Melting Additive Manufacturing", Accessed: Feb. 11, 2024. [Online]. Available: http://www.sti.nasa.gov

[32] B. Müller, ; U Renz, B. Mü Ller, and U. Renz, "Development of a fast fiber-optic two-color pyrometer for the temperature measurement of surfaces with varying emissivities," *Review of Scientific Instruments*, vol. 72, no. 8, pp. 3366–3374, Aug. 2001, doi: 10.1063/1.1384448.

[33] A. Lerner *et al.*, "Laser Powder Bed Fusion thermal monitoring using optical fiber sensors: in situ measurements and modelling," *2023 Conference on Lasers and Electro-Optics Europe and European Quantum Electronics Conference, CLEO/Europe-EQEC 2023*, 2023, doi: 10.1109/CLEO/EUROPE-EQEC57999.2023.10232209.

[34] C. Krishna, P. Vallabh, and X. Zhao, "Melt pool temperature measurement and monitoring during laser powder bed fusion based additive manufacturing via single-camera two-wavelength imaging pyrometry (STWIP)," *J Manuf Process*, vol. 79, pp. 486–500, 2022, doi: 10.1016/j.jmapro.2022.04.058.

[35] B. Bevans *et al.*, "Heterogeneous sensor data fusion for multiscale, shape agnostic flaw detection in laser powder bed fusion additive manufacturing," *Virtual Phys Prototyp*, vol. 18, no. 1, Dec. 2023, doi: 10.1080/17452759.2023.2196266.

[36] J. Petrich, Z. Snow, D. Corbin, and E. W. Reutzel, “Multi-modal sensor fusion with machine learning for data-driven process monitoring for additive manufacturing,” *Addit Manuf*, vol. 48, p. 102364, Dec. 2021, doi: 10.1016/J.ADDMA.2021.102364.

[37] P. K. Rao, J. Liu, D. Roberson, Z. Kong, and C. Williams, “Online Real-Time Quality Monitoring in Additive Manufacturing Processes Using Heterogeneous Sensors,” *Journal of Manufacturing Science and Engineering, Transactions of the ASME*, vol. 137, no. 6, Dec. 2015, doi: 10.1115/1.4029823/374977.

[38] K. J. Colligan and R. S. Mishra, “A conceptual model for the process variables related to heat generation in friction stir welding of aluminum,” *Scr Mater*, vol. 58, no. 5, pp. 327–331, Mar. 2008, doi: 10.1016/j.scriptamat.2007.10.015.

[39] W. D. Hartley and S. W. Case, “Processing Mechanics of Additive Friction Stir Deposition.”

[40] S. H. Mousavi Anijdan, H. R. Madaah-Hosseini, and A. Bahrami, “Flow stress optimization for 304 stainless steel under cold and warm compression by artificial neural network and genetic algorithm,” *Mater Des*, vol. 28, no. 2, pp. 609–615, Jan. 2007, doi: 10.1016/J.MATDES.2005.07.018.

[41] K. A. Fraser, “Robust and efficient meshfree solid thermo-mechanics simulation of friction stir welding,” 2017.

[42] K. Kumar, C. Kalyan, S. V. Kailas, and T. S. Srivatsan, “An Investigation of Friction During Friction Stir Welding of Metallic Materials,” *Materials and Manufacturing Processes*, vol. 24, no. 4, pp. 438–445, Apr. 2009, doi: 10.1080/10426910802714340.

[43] A. F. Hasan, C. J. Bennett, P. H. Shipway, S. Cater, and J. Martin, “A numerical methodology for predicting tool wear in Friction Stir Welding,” *J Mater Process Technol*, vol. 241, pp. 129–140, Mar. 2017, doi: 10.1016/J.JMATPROTEC.2016.11.009.

[44] S. Mandal, J. Rice, G. Hou, K. M. Williamson, and A. A. Elmustafa, “Modeling and simulation of a donor material concept to reduce tool wear in friction stir welding of high-strength materials,” *J Mater Eng Perform*, vol. 22, no. 6, pp. 1558–1564, Jun. 2013, doi: 10.1007/S11665-012-0452-4/FIGURES/10.

[45] J. Zhang, P. Upadhyay, Y. Hovanski, and D. P. Field, “High-Speed Friction Stir Welding of AA7075-T6 Sheet: Microstructure, Mechanical Properties, Micro-texture, and Thermal History”, doi: 10.1007/s11661-017-4411-4.

[46] G. R. Merritt, M. B. Williams, P. G. Allison, J. B. Jordon, T. W. Rushing, and C. A. Cousin, “Closed-Loop Temperature and Force Control of Additive Friction Stir Deposition,” *Journal of Manufacturing and Materials Processing*, vol. 6, no. 5, Oct. 2022, doi: 10.3390/jmmp6050092.

[47] Z. T. Niu, H. Qi, Y. K. Ji, S. Wen, Y. T. Ren, and M. J. He, “Real-time reconstruction of thermal boundary condition of porous media via temperature sequence,” *International Journal of Thermal Sciences*, vol. 177, Jul. 2022, doi: 10.1016/j.ijthermalsci.2022.107570.

[48] D. Lu and C. Wang, “Three-dimensional temperature field inversion calculation based on an artificial intelligence algorithm,” *Appl Therm Eng*, vol. 225, May 2023, doi: 10.1016/j.applthermaleng.2023.120237.

[49] S. Motahar, “Experimental study and ANN-based prediction of melting heat transfer in a uniform heat flux PCM enclosure,” 2020, doi: 10.1016/j.est.2020.101535.

[50] C. Fieberg and R. Kneer, “Determination of thermal contact resistance from transient temperature measurements,” *Int J Heat Mass Transf*, vol. 51, no. 5–6, pp. 1017–1023, Mar. 2008, doi: 10.1016/j.ijheatmasstransfer.2007.05.004.

[51] A. Bejan and A. D. Kraus, *Heat transfer handbook*. J. Wiley, 2003.

[52] M. Nouari, B. Haddag, A. Moufki, and S. Atlati, “Investigation on the built-up edge process when dry machining aeronautical aluminum alloys,” *Machining of Light Alloys*, pp. 35–48, Aug. 2018, doi: 10.1201/B22153-2.

[53] R. Nandan, T. Debroy, and H. K. D. H. Bhadeshia, “Recent advances in friction-stir welding-Process, weldment structure and properties”, doi: 10.1016/j.pmatsci.2008.05.001.

[54] R. Nandan, G. G. Roy, T. J. Lienert, and T. Debroy, “Three-dimensional heat and material flow during friction stir welding of mild steel,” *Acta Mater*, vol. 55, no. 3, pp. 883–895, Feb. 2007, doi: 10.1016/J.ACTAMAT.2006.09.009.

[55] K. Fraser, L. I. Kiss, L. St-Georges, and D. Drolet, “Optimization of friction stir weld joint quality using a meshfree fully-coupled thermo-mechanics approach,” *Metals (Basel)*, vol. 8, no. 2, Feb. 2018, doi: 10.3390/MET8020101.

[56] S. Solhjoo, “Revisiting the Common Practice of Sellars and Tegart’s Hyperbolic Sine Constitutive Model,” *Modelling 2022, Vol. 3, Pages 359-373*, vol. 3, no. 3, pp. 359–373, Aug. 2022, doi: 10.3390/MODELLING3030023.

[57] G. G. Stubblefield *et al.*, “Ballistic Evaluation of Aluminum Alloy (AA) 7075 Plate Repaired by Additive Friction Stir Deposition Using AA7075 Feedstock,” *Journal of Dynamic Behavior of Materials*, vol. 9, no. 1, pp. 79–89, Mar. 2023, doi: 10.1007/s40870-022-00363-6.

[58] C. J. T. Mason *et al.*, “Process-structure-property relations for as-deposited solid-state additively manufactured high-strength aluminum alloy,” *Addit Manuf*, vol. 40, Apr. 2021, doi: 10.1016/j.addma.2021.101879.

[59] R. S. Mishra, R. S. Haridas, and P. Agrawal, “Friction stir-based additive manufacturing,” *Science and Technology of Welding and Joining*, vol. 27, no. 3. Taylor and Francis Ltd., pp. 141–165, 2022. doi: 10.1080/13621718.2022.2027663.

[60] R. S. Mishra and M. Komarasamy, *Physical Metallurgy of 7XXX Alloys*. Elsevier, 2016. doi: 10.1016/b978-0-12-809465-5.00002-7.

[61] M. Schöbel, P. Pongratz, and H. P. Degischer, "Coherency loss of Al 3(Sc,Zr) precipitates by deformation of an Al-Zn-Mg alloy," *Acta Mater*, vol. 60, no. 10, pp. 4247–4254, Jun. 2012, doi: 10.1016/j.actamat.2012.04.011.

[62] A. Zubelewicz, "Century-long Taylor-Quinney interpretation of plasticity-induced heating reexamined," *Scientific Reports 2019 9:1*, vol. 9, no. 1, pp. 1–7, Jun. 2019, doi: 10.1038/s41598-019-45533-0.

[63] V. L. Popov, "Thermal Effects in Contacts," *Contact Mechanics and Friction*, pp. 199–205, 2010, doi: 10.1007/978-3-642-10803-7_13.

[64] B. H., "Theoretical Study of Temperature Rise at Surfaces of Actual Contact under Oiliness Lubricating Conditions," *Proc. Instn. Mech. Engrs. (General discussion on lubrication and lubricants)*, vol. 2, pp. 222-, 1937, Accessed: Mar. 11, 2024. [Online]. Available: https://cir.nii.ac.jp/crid/1573668924965107328

[65] J. C. Jaeger and J. C. Jaeger, "Moving sources of heat and the temperature at sliding contacts," *Journal and proceedings of the Royal Society of New South Wales*, vol. 76, no. 3, pp. 203--224, May 1943, doi: 10.5962/p.360338.

[66] K. J. Zwick and M. Tate, "Flash Temperature Theory," *Encyclopedia of Tribology*, pp. 1182–1194, 2013, doi: 10.1007/978-0-387-92897-5_1312.

[67] D. G. Bansal and J. L. Streator, "A method for obtaining the temperature distribution at the interface of sliding bodies," *Wear*, vol. 266, no. 7–8, 2009, doi: 10.1016/j.wear.2008.08.019.

[68] M. Akbari, D. Sinton, and M. Bahrami, "Moving heat sources in a half space: Effect of source geometry," *Proceedings of the ASME Summer Heat Transfer Conference 2009, HT2009*, vol. 3, pp. 685–694, 2009, doi: 10.1115/HT2009-88562.

[69] R. Mendoza, "In-service Corrosion Issues in Sustainment of Naval Aircraft," 2012.

[70] R. Joey Griffiths, D. T. Petersen, D. Garcia, and H. Z. Yu, "Additive friction stir-enabled solid-state additive manufacturing for the repair of 7075 aluminum alloy," *Applied Sciences (Switzerland)*, vol. 9, no. 17, Sep. 2019, doi: 10.3390/app9173486.

[71] M. E. J. Perry, R. J. Griffiths, D. Garcia, J. M. Sietins, Y. Zhu, and H. Z. Yu, "Morphological and microstructural investigation of the non-planar interface formed in solid-state metal additive manufacturing by additive friction stir deposition," *Addit Manuf*, vol. 35, Oct. 2020, doi: 10.1016/j.addma.2020.101293.

[72] M. E. J. Perry *et al.*, "Tracing plastic deformation path and concurrent grain refinement during additive friction stir deposition," *Materialia (Oxf)*, vol. 18, Aug. 2021, doi: 10.1016/j.mtla.2021.101159.

[73] C. C. De Castro *et al.*, “Tool wear mechanisms and effects on refill friction stir spot welding of AA2198-T8 sheets,” *Journal of Materials Research and Technology*, vol. 20, pp. 857–866, Sep. 2022, doi: 10.1016/J.JMRT.2022.07.092.

[74] Q. Chu *et al.*, “On visualizing material flow and precipitate evolution during probeless friction stir spot welding of an Al-Li alloy,” *Mater Charact*, vol. 144, pp. 336–344, Oct. 2018, doi: 10.1016/J.MATCHAR.2018.07.026.

[75] “Wrought Aluminum Alloys: Atlas of Fractographs,” in *Fractography*, ASM International, 2018, pp. 414–439. doi: 10.31399/asm.hb.v12.a0000621.

3 Chapter 3: Unveiling Real-World Heat Transfer Dynamics

In the preceding chapter, the groundwork for the analysis techniques used and the common principles considered was laid. In this chapter, some of the simplifications and non-standard tooling used are replaced with conditions that more accurately reflect the end-use case of the process. A discussion on the limitations of the assumptions and what bounds can be put onto future heat generation assumptions is also shown.

3.1 Manuscript 2: Traversal Heat Generation and Transfer in Additive Friction Stir Deposition of Aluminum Alloys

Kendall P. Knight, Greg Hahn, Hang Z. Yu

Abstract

Additive Friction Stir Deposition (AFSD) has emerged as a promising technique for fabricating metallic components with forging-like properties. This study investigates the tool geometry, traversal parameters, and thermal characteristics during the AFSD process. An inverse heat transfer approach is used to investigate the heat generation and distribution to elucidate these traversal and tool effects. It was found that the total heat generation trends very well with the spindle power but the distribution of this heat, either into the tool or into the substrate is a time-dependent variable driven by the thermal state. Additionally, small differences in the construction of the AFSD tool were shown to drive large effects. Tools with protrusions and those with flat faces were shown to have different behaviors in the heat generation mechanism leading to different temperature distributions. From the measurements conducted in this work, it is shown that the embedded tool thermocouple is insufficient to characterize the AFSD process. This research underscores the significance of tailored tooling and traversal strategies in harnessing the full potential of AFSD for fabricating high-performance metallic components.

Introduction

In Additive Friction Stir Deposition (AFSD), the generation and propagation of heat are critical to leveraging the friction stir principle to deposit material [29]. Without sufficient heat generation, the plastic flow of the material cannot occur. Once sufficient heat has been generated to allow for flow there is a wide range of heat generation and dissipation parameters that will allow a stir to sustain. Understanding the resulting thermal state of these parameters is critical to understanding the temperature history of any given voxel of an AFSD print [15], [17], [19], [20]. Furthermore, since the flow properties of a given material are so intimately connected to temperature [16], [41], [54], [55], [56], knowing the temperature to a high degree of accuracy is required to begin to understand the strain and strain rates a given voxel of material experienced during printing. Since it is well understood that materials of interest such as 6xxx and 7xxx series aluminums can have tight processing windows [57], [58], [59], [60], [61] where adverse metallurgical effects do not occur the study and understanding of heat generation underpins all AFSD understanding.

In AFSD, and its more mechanically constrained cousin friction stir welding (FSW), two mechanisms of heat generation are assumed to take place: volumetric and frictional [18], [29], [43]. Volumetric heat generation is driven by viscous dissipation of energy in the flowing metal. The energy released from flow is a function of the stir's velocity and its viscosity. Viscosity is in

turn a function of temperature leading to a fully coupled system. Much effort has been made to understand this behavior in a variety of materials. Common numerical methods of dealing with the coupling include models like Sellars-Tegart, Johnson Cook and Fraser, Kiss, St. George [16], [41].

Alternatively, heat can be generated between the rotating tool and the nominally stationary stir. In practice, the stir exhibits sticking and slipping behavior and depending on processing conditions can either move with the tool, like the zero-slip wall condition in fluid dynamics, or at some portion of the tool's velocity resulting in sliding friction [11]. In AFSD this is normally expressed as the stick-slip coefficient with values between 1-0. Where a value of 1 indicates a zero-slip condition and 0 indicates a fully static stir. This value can change as a function of radius, diameter, and contact pressure. The exact values and curves of this coefficient are unknown and difficult to measure directly. To the best of the author's knowledge, no direct measurement has been completed for AFSD.

In previous work, these two heat generation mechanisms have been considered together where thermal energy was considered to generate, from mechanical energy, in the stir and conduct into the surroundings, specifically the tool and the substrate. Additionally, the temperature of the stir was considered to be a uniform, transient, "effective" temperature that drove heat conduction. This idea is equivalent to the volumetric average in the far spatial field. From these assumptions, several meaningful physical quantities could be calculated using inverse heat transfer. First, the thermal energy generated could be tabulated and compared to the spindle power. For the stationary case, it was found that ~80% of the spindle power could be traced as thermal power. It is believed that the other 20% of the energy is transferred to the microstructure in the form of thermodynamically unfavorable grain refinement and a small percentage is lost to convection. Secondly, the ratio of heat transfer into the substrate and the tool could be quantified as a function of time. This ratio reflects the heat transfer state at a given time based on the temperature of the tool and the substrate and as such evolves through time based on the diffusivity of the two parts and their thermal boundary conditions. In general, this tool/substrate ratio hovered between 0.3-0.5. Thirdly, a contact heat transfer coefficient (CHTC) was calculated by considering the temperature difference between the stir and the face. In effect, this can be considered analogous to a convection coefficient where the temperature difference drives a given heat flux through the contact gap. It was found that the CHTC was very large, meaning that conduction into the tool was very efficient.

It is important to contextualize these results, in the previous work depositions were carried out on a first-of-a-kind R2 MELD machine using a single-piece, solid H13 tool pictured in Figure 13A. One tool had 2.2mm tall protrusions hereafter referred to as pins shown in Figure 13B and one had a featureless face, hereafter referred to as flat shown in Figure 13C. The current state-of-the-art, commercially available off-the-shelf tool is the MELD Manufacturing three-piece tool with integrated thermocouple shown in Figure 13D. It is comprised of three main pieces: the cap, the body, and the face. The H13 tools teel cap is press fit to the body and provides mechanical keying and centering to the larger machine through its flats and a taper. The body is the main piece of the tool, with holes for screws to draw the face up and holes for thermocouple

penetration. It can be made of either copper-beryllium or H13 tool steel. The final piece is the face, made of H13 tool steel. This is what directly contacts the stir and receives the torque, force, and heat flux. The thermal contact condition of the cap, relative to the body, determines how easily heat is transferred out of the stir. Since these two pieces only have a contact region under stress in one area, the overall heat transfer is poor, leading to heat being concentrated in the face. Additionally, the experiments completed previously were only done with a stationary deposition, there was no movement of the tool relative to the workpiece. To overcome some of the limitations from the previous study a new set of experiments is shown here using commonly available tooling and considering tool movement.

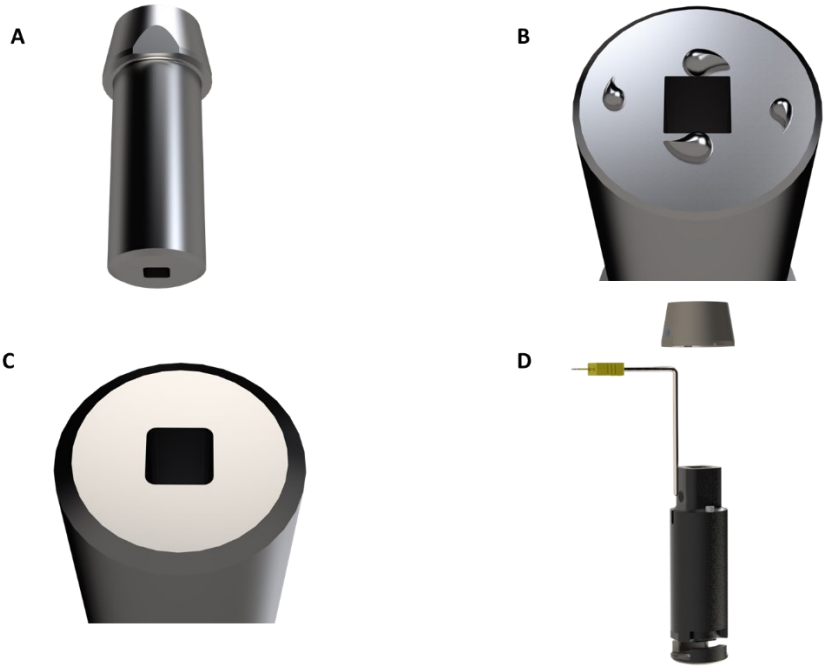

Figure 13 A) Rendering of a single-piece tool. B) Rendering of a pinned tool showing the four 2.2mm tall protrusions. C) Rendering of a flat tool. D) Exploded view of a three-piece tool showing the three main pieces and the thermocouple.

Materials and Methods

To better understand the heat generation in a scenario more similar to a real-world AFSD build a geometry made from AA6061-T6 was used with dimensions of 206mm x 44mm x 38.1mm. The 38.1mm dimension corresponds to the left to right thickness as this is the diameter of the tool. This geometry is shown in Figure 14A. One side of this geometry was painted with a known emissivity IR spray paint (whatever Moldova) to act as a favorable IR image target. A TIM VGA (Micro-Epsilon, MA, USA) IR camera was used to measure the temperature field of the substrate at 32 frames per second. This camera gave a lateral resolution of 440 pixels and 102 pixels in the vertical direction. An IR image can be seen in Figure 13B showing the thermal field being captured.

The side of the tool was painted in the same way as the substrate and a second TIM VGA IR camera was used to record the temperature of the side of the tool at 125Hz to resolve the rotation of the tool without aliasing. This resulted in a resolution of 47 pixels in the region of interest.

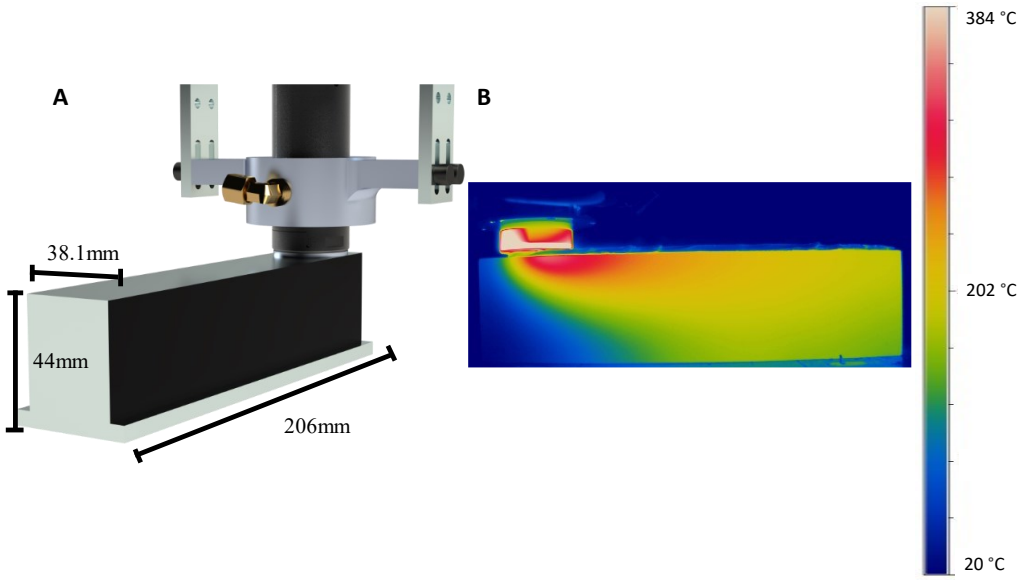

Figure 14 A) Rendering of the test setup showing the substrate geometry used, with the tool and cooling jacket. B) Thermal image of the flat 254 mm/min test taken at 80s.

Stirs were conducted with a flat and pinned three-piece H13 tool steel tool with an integrated thermocouple from MELD Manufacturing on an L3 Meld Machine (MELD Manufacturing, VA, USA). A 12.7 mm x 12.7mm feed rod made of AA6061 was used. To understand the effect of traversing, a constant ratio of material feed rate and traverse rate was used, for these prints, that ratio was equal to 0.75. The traversal speeds used were 127 mm/min, 254 mm/min, and 381 mm/min corresponding to 5 ipm, 10 ipm, and 15 ipm. All prints were conducted at a rotation rate of 350 RPM. The layer height of the deposition was 2mm for both tool designs. To achieve the desired layer height with the pinned tool, the pins protruded 0.5mm into the substrate. The print was started by bringing the rotation rate up to 350 RPM and then moving the tool to the layer height. Once the tool was at the desired position material was fed at 12.7 mm/min until the tool thermocouple read 260 °C. Once this temperature was hit, the feed rate was increased to the setpoint and traversal began at the specified rate. The print was run along the entire length of the substrate. During the prints, the L3 Meld Machine recorded the spindle power and the tool thermocouple temperature at a rate of 1 Hz.

To apply the inverse heat transfer algorithm, a COMSOL model was constructed for both the substrate and the tool. For the substrate a 2D model was used, that considered the stir, the substrate geometry, and a 50mm thick steel backing plate. The model used a mesh size of 3 mm and a timestep of 0.1 seconds. This model employed convection on all sides except the contact between the backing and the substrate with a coefficient of 1 $\frac{W}{m^2K}$. The contact was treated as an

impaired conduction with a contact conductance of 0.0001 $\frac{W}{m^2K}$, this is due to poor surface finish on the bottom not allowing efficient conduction into the backing plate. The stir was treated as a surface heat flux on a domain with a 2 mm thickness, corresponding to the layer height. The top of this domain had the surface heat flux applied to it in the area where the tool was located. Additionally, material addition was treated by changing the density, thermal conductivity, and heat capacity from that of air to aluminum when the material was within the radius of the tool. Changing the properties was achieved using COMSOL state variables.

To model the tool, a full 3D model was constructed based on a disassembled tool. In Figure 15A a cross section of the tool is shown. The COMSOL model was simplified to only the face and the body of the tool since nearly all the thermal energy is extracted with a cooling jacket, as shown in Figure 14A. The body was modeled as H13 tool steel with a tetrahedral mesh. The cooling jacket was approximated using a convection coefficient on only the areas that would be in contact with the cooling water. The rest of the cylinder was treated with a convection coefficient of 30 $\frac{W}{m^2K}$ since the tool rotates in the air. The area where the body contacts the cap was treated as convection with a coefficient of 30 $\frac{W}{m^2K}$. The heat flux was applied uniformly to the bottom of the face and the face was assumed to have four different thermal contact conditions with the tool. These conditions are driven by the manufacturing tolerances of production and the way force and torque transfer from the face to the body. These contact regions are shown in Figure 15B.

Using the recorded data and the COMSOL models the inverse heat transfer problem could be solved by using the function specification method from Beck et. al. This method yielded both the predicted heat flux and a predicted temperature field for both models. This predicted temperature is easily compared to the measured data to understand the error in the model. To determine the values of the conductance of the face contacts and the convection of the water, surrogate optimization was implemented in MATLAB. The optimization started by guessing the values to be determined, and the inverse algorithm was run with those guesses. The predicted thermocouple and predicted IR data were then compared to the measured data and the guess was updated. The goal of the optimization was to change the values of the conductance and convection to make both the predicted thermocouple and predicted IR data match the measured data. This approach worked well and achieved good agreement between the model and the measured data. This optimization was repeated for both the flat tool and the pinned tool since there is variation between individual tools from the manufacturer.

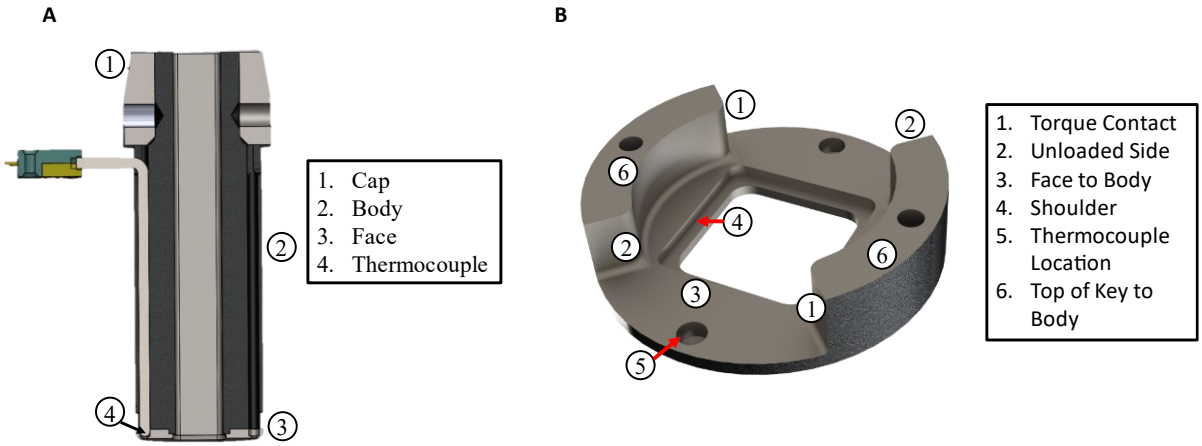

Figure 15 A) Cross-section of a three-piece tool showing the three main body components and the thermocouple routing and placement. B) A close view of the face showing the five distinct thermal contact regions and the thermocouple termination

Results

Internal Tool Contact

The different contacts between the face and the body are driven by the different loading conditions, and manufacturing tolerances seen by each face. In Figure 15B, the faces labeled #1 are the two faces that transmit the torque from the counterclockwise rotating spindle. With a nominal spindle torque of 200 N*m, each face takes approximately 5.6kN of force creating close thermal contact. The two faces labeled #2 are forced away from the body by the same torque that closes #1. Since the face is not press fit into the body a small gap appears during printing, limiting heat transfer from those faces. Contact #3 is the face that is drawn nominally flush by the bolts holding the face piece to the body. It is uncertain if force from the stir is transmitted through this face or contact #4. In this work, since contact 4 is much smaller than #3 and the mating conditions are not known to a high degree of precision, contact #4 was treated as part of 3#. The area labeled #5 is the hole that the thermocouple is connected into. This connection can be either a braze or a spot weld. In the tools used in these experiments, the connection was a braze. Contact #6 are the two faces that have the bolt hole. These faces are the top of what will be referred to as the key. On the flat tool used in this study, these faces are cut slightly shorter than the slot they mate with so there is also no thermal conductance between them and the tool body. On the pinned tool used, the face sat slightly angled due to the braze in contact #5 sitting slightly above the surface. This forced one face into much better contact resulting in a higher average contact conductance value. In general, each individual tool will vary based on surface corrosion and mechanical design and if accurate contact parameters are needed, they must be measured. Due to these different contact conditions, the temperature field of the tool is non-uniform, necessitating the use of a high frame rate to capture the differences.

In Figure 16A a rendering of the field of view of the IR camera is shown. The cooling jacket truncates the visibility of the stir, but it does not affect the accuracy of the prediction since the temperature is exponentially more sensitive towards the face of the tool. In Figure 16B an IR image is shown. This IR image is taken at the end of the flat 127mm/min print and shows the

area of the tool without the key. There is a left-to-right asymmetry due to the difference in the torque contact where the right side has a better thermal conductance. The contrast with Figure 16C is striking. This image shows the key part of the face and is much hotter. In Figure 16D, the results of the contact conductance optimization are shown. The predicted and measured thermocouple agree very well, and the predicted and measured IR side temperatures also agree.

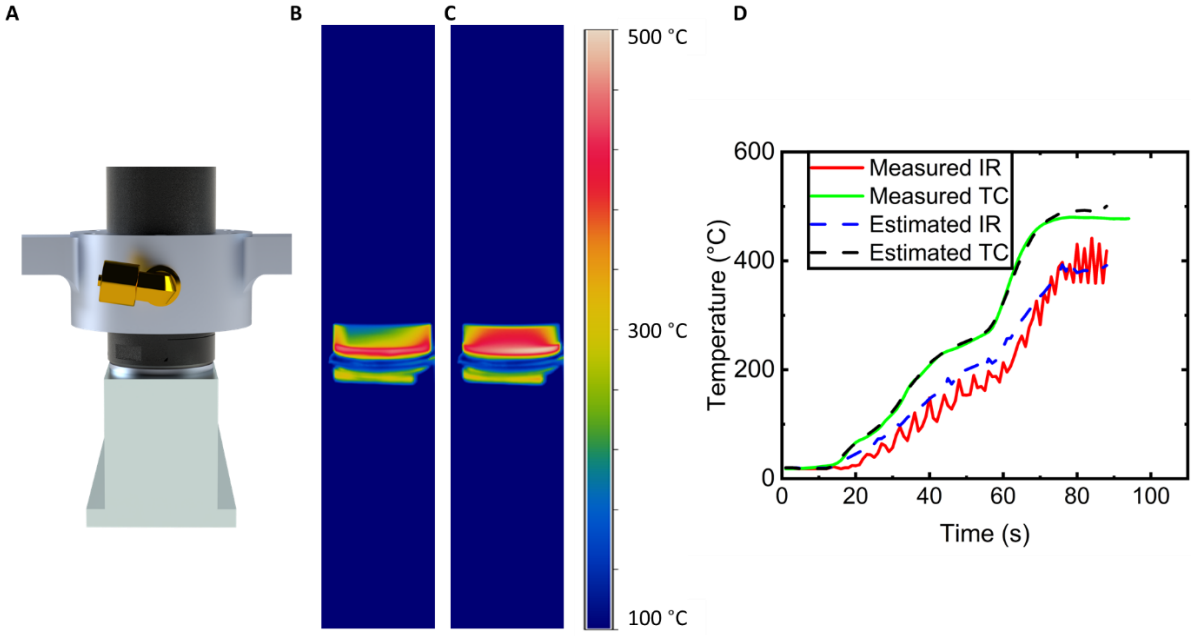

Figure 16 A) Rendering of the IR camera's field of view, showing the substrate head-on, the tool, and the cooling jacket. B) IR image of the tool at the end of the flat, 127 mm/min print. The tool is oriented such that the space between the two keys is shown facing the camera. Note the left-to-right asymmetry caused by the torque-loaded contact allowing more heat transfer on the right-hand side. C) IR image of the tool 0.042 seconds, or five frames, after B showing the key. Note the large temperature difference caused by the contact differences. D) Results of the contact optimization showing a low error between both the thermocouple and the IR data.

The results of the contact optimization are shown below in Table 1. These values have some variation between the two tools but generally conform to the understanding of the tool's construction. The main difference between the two tools is the values for contact #4. The pin tool has a larger value, and this conforms with the experimental observations. The water jacket estimate was left as a variable for both optimization runs, and its convergence to nearly the same value provides some more confidence in the optimization process.

Table 1 Calculated contact conductance values and water jacket convection for the flat and pinned tool. All units in $\frac{W}{m^2K}$.

	#1 Torque Face	#2 Unloaded Face	#3 Face to Body	#4 Top of Key to Body	Water Jacket Convection
Flat Tool	10505	7673	1094	5997	158
Pin Tool	15500	9220	1193	12022	154

Temperature

By understanding the conductance values within the tool, the inverse heat transfer process can be applied to both the tool and the substrate to estimate heat flux and temperature. To understand the error in the estimation the predicated temperature at given points and times can be compared to the measured temperature at the same points and times. This is shown below in Figure 17. Note that in all subfigures the graphs have been shifted to show the start of traversal at $t = 0$ for clarity. The substrate measured data in A and C is taken as the maximum of the topmost IR plane on the substrate, about 3mm below the stir. For the tool curves in B and D, the measured data is from the tool thermocouple. All the flat tool and substrate data match very well between prints with the same tool type and the maximum measured tool temperature is independent of traversal rate. In the case of the pinned tool and substrate, there are some run-to-run differences at the beginning of the print but these are due to the fact the tool makes contact with the substrate with its pins before the material is being fed in. Small discrepancies in the amount of time it takes to begin material feeding lead to the different amounts of time before traversal. Additionally, the maximum temperature in both is not a function of the traversal rate.

.

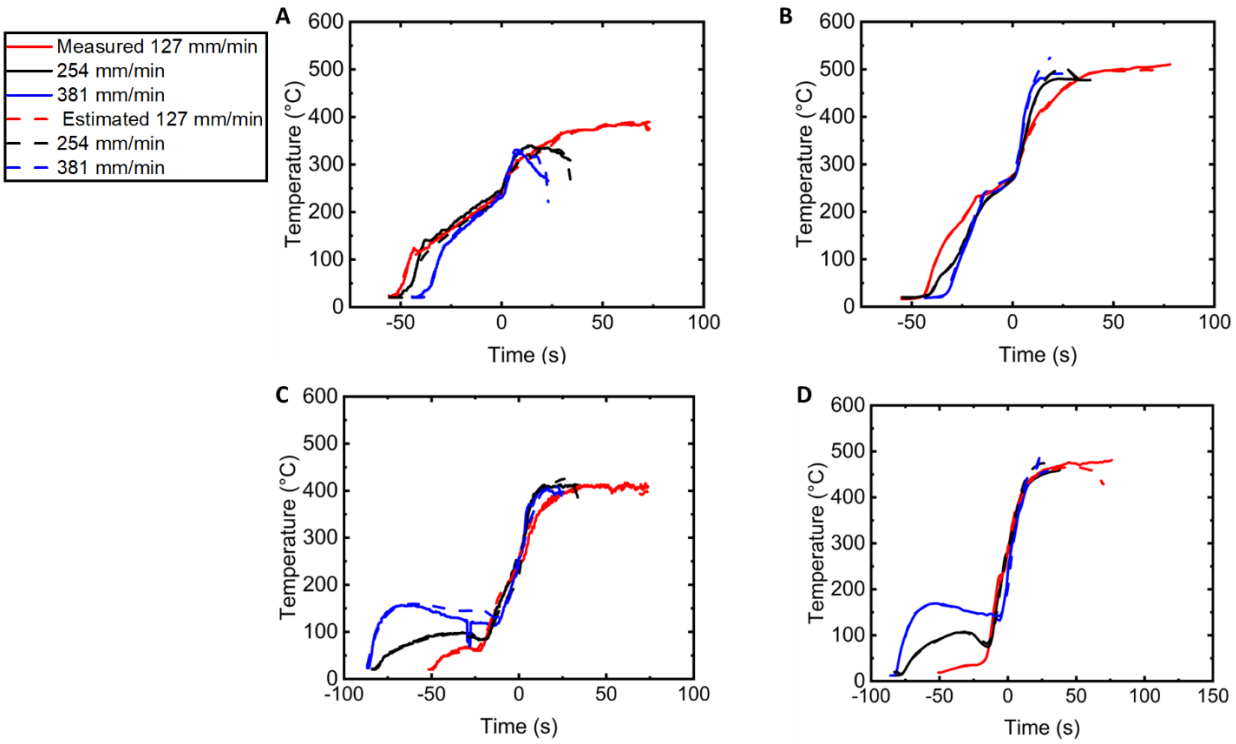

Figure 17 Predicted and measured temperatures with the traversal time centered on t=0 for: A) Flat substrate B) Flat tool C) Pinned substrate D) Pinned tool. Note that the solid curve for the tool graphs is the embedded tool thermocouple.

Thermal Power

Since the measured and predicted temperatures have good agreement, there is confidence in the predicted heat flux values. The values for all experimental trials are shown in Figure 18. In A and B the heat flux for the substrate and tool for the flat cases is shown. At the start of traversal, the heat flux spikes dramatically owing to the increased material feed rate. The maximum value of the heat flux increases with the traverse rate in a nearly linear fashion. Near the end of the print, the heat flux begins to taper off, this is due to the tool approaching the end of the substrate, which due to the convection boundary condition acts as a thermal barrier. The barrier results in an accumulation of heat energy on the boundary reducing the driving force for heat input. Looking at the ratio of the tool and the substrate in Figure 18C, the first conclusion is that the substrate heat flux is nearly a full order of magnitude larger than the tool. On the surface, this contrasts with the ratio reported by Knight et. al. for a featureless tool of approximately 1. This discrepancy is due to the "heat break" effect of the three-piece tool in this work vs the single-piece tool used previously. This ratio also decreases as traversal continues, with a smaller ratio corresponding to a faster traverse rate. This contrasts with the static ratio predicted for friction stir welding [53] of 0.42 for this system. In Figure 18D and E, the substrate and tool heat flux are shown for the pinned tool case. Many of the same trends exist for the pinned case as for the flat case. It should be noted that the maximum heat flux for the tool in each print was nearly the same and like the flat case occurred directly after the start of traversal. The ratio of the heat flux shown in F also has similar trends but shows a smaller final value for each of the prints. The

slowest traversal case shown in red also exhibits an upward trend and concavity near the end of the print.

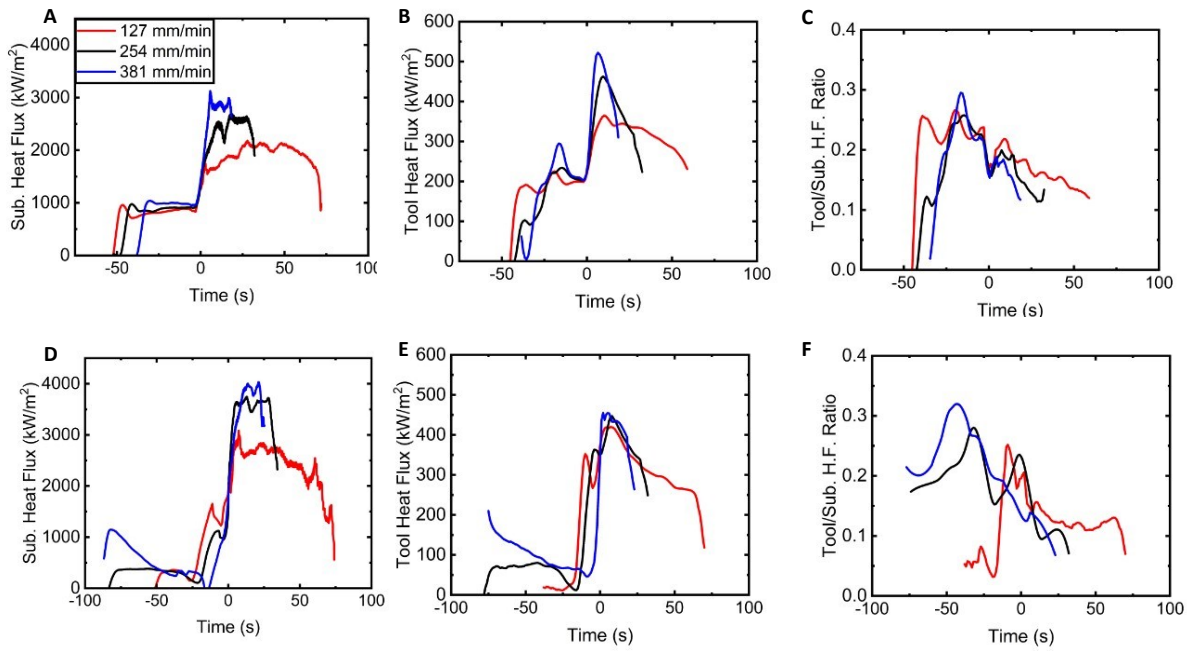

Figure 18 A) Flat substrate heat flux. B) Flat tool heat flux. C) Ratio of tool and substrate heat flux for the flat case. D) Pinned substrate heat flux. E) Pinned tool heat flux. F) Ratio of the tool and substrate heat flux for the pinned case.

The area that the heat flux acts on for both the tool and substrate can be taken as a known constant and by multiplying the heat flux by the area and adding the heat flux into the tool and into the substrate the total thermal power can be found, as shown below.

$$\dot{Q} = \dot{q_{tool}} * A_{tool} + \dot{q_{\text{sub}}} * A_{sub} \quad (1)$$

The thermal power is shown Figure 19A and C for the flat and pinned tool respectively. It should be noted that it very closely resembles the substrate heat flux since that is the dominant conduction path. It can be compared with the spindle power shown in B and D for the flat and pinned tool. This power is directly recorded from the machine and was baseline subtracted to remove the power consumed by frictional losses in the drivetrain. At each time the ratio of thermal power and spindle power can be compared, and the average is shown in Figure 19E. This ratio represents the amount of mechanical power that is turned into heat, also known as the Taylor-Quinney coefficient [62]. For the pinned tool, this ratio is very constant with respect to the traversal rate with a value of 0.74. For the flat case, there is a weak dependency on the traversal rate where the ratio starts lower than the pinned case at the same traversal rate, meaning less heat is generated for the same mechanical power and it increases with increasing traversal rate to nearly the same value.

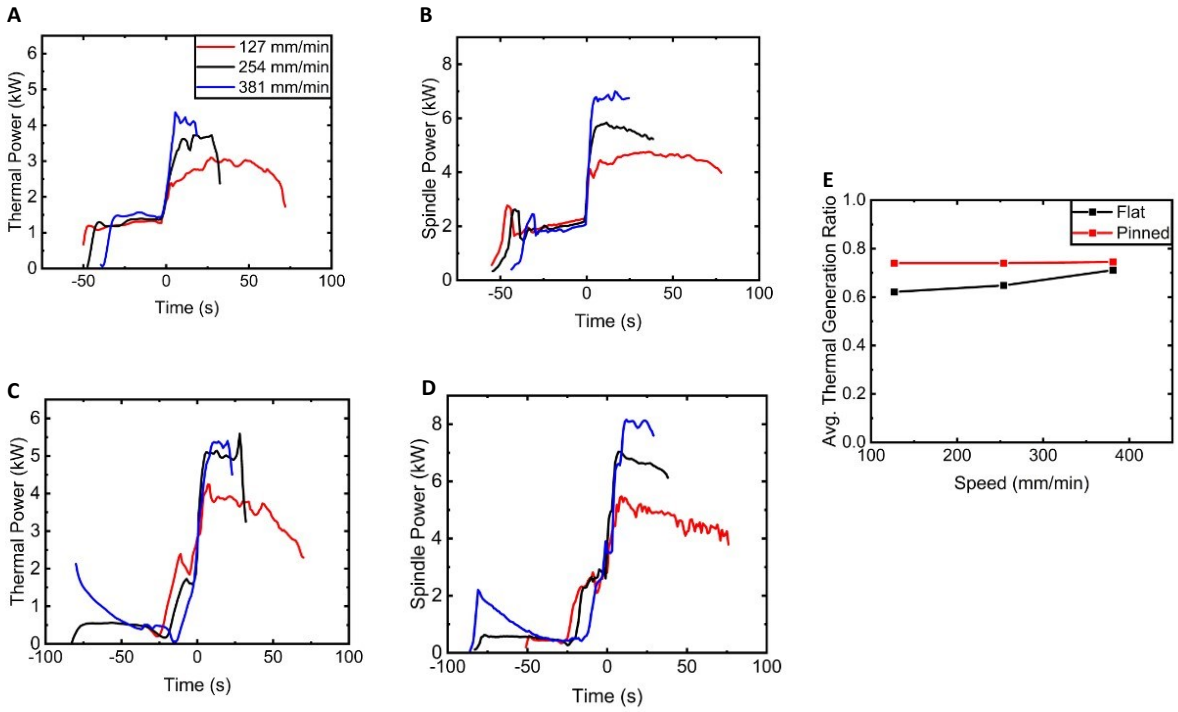

Figure 19 A) Total thermal power for the flat cases B) Measured spindle power for the flat cases. C) Total thermal power for the pinned cases. D) Measured spindle power for the pinned cases. E) Average ratio of spindle power to thermal power.

Using the COMSOL model, temperatures that were not measured can be estimated based on the physics captured by the inverse method. This allows for the temperature distribution along the side of the tool and the tool face to be captured based on the assumption of a uniform heat flux. These distributions are shown in Figure 20. From the side profiles in A and C, it is clear that the "heat break" plays a critical role in the temperature distribution of the tool and that the flat tool is slightly hotter. The face distributions show similar results where the flat tool is hotter. The more striking feature is the non-axisymmetric distribution predicted for both tools. In the model, the distribution is driven by the different conduction states of the key and non-key areas of the face piece.

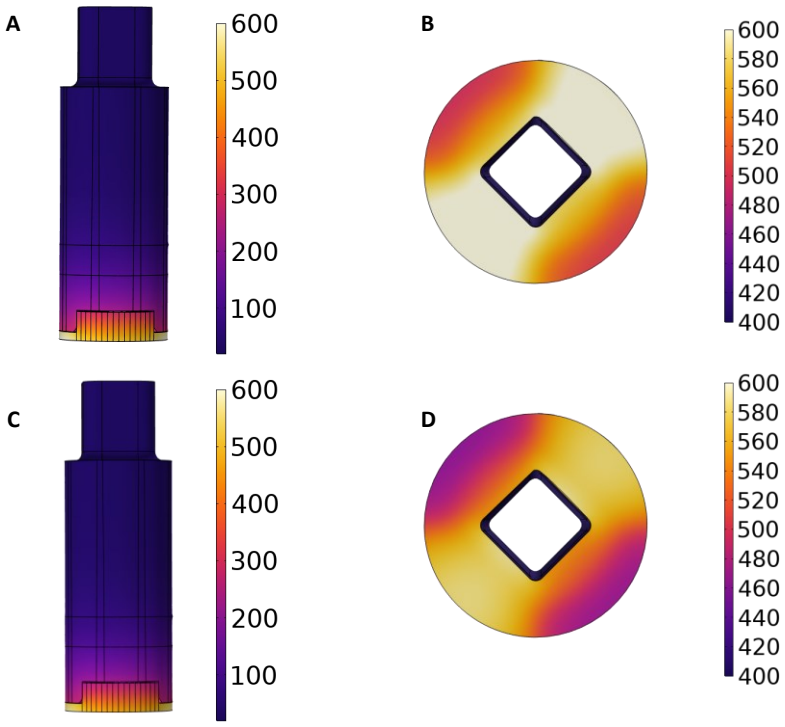

Figure 20 Tool side (A&C) and face (B&D) temperature distribution from COMSOL in °C at the same timestep in the print and traversal rate for the: A-B) Flat case. C-D) Pinned case.

Discussions

Tool Effects

From these experiments a few conclusions are salient. Firstly, when transitioning from a stationary print to a traversal, there is a large increase in the thermal energy release rate. It is unclear from the data in these experiments if this increase is directly due to traversal or the corresponding material feed rate increase. Based on the intensity of the spike shown in Figure 18A, a significant component of the increase is likely due to the feed rate increase and more work will be needed to understand the interplay between the two. The second salient feature is that the ratio of tool to substrate heat flux is dependent entirely on the thermal state at a given time and by changing the traversal rate different ratios are seen. The rate at which the tool reaches the end of the substrate also affects heat generation and the tool-substrate ratio due to the thermal boundary of the wall. This ratio, also called the heat partition factor, has been the topic of much study in thermal contacts [3], [63], [64], [65], [66]. The variability of this ratio has large implications for the control of AFSD. Since the current, state-of-the-art, control systems leverage thermocouples embedded in the tool [24], [45], a change in the amount of heat energy going into the tool will result in a different reading from the thermocouple even for a constant heat source. Since the ratio of heat flux is dependent on a variety of factors including geometric heat transfer effects (i.e. edges) and process heat transfer effects (i.e. traverse rate and feed rate) the difference

between the thermocouple temperature and the temperature of the face of the tool then becomes a function of these variables. Since heat flux in one dimension is defined as:

$$hf = -k\frac{dT}{dx} \tag{2}$$

a larger heat flux into the tool creates a larger difference between the two temperatures. The solution to this problem was proposed by Knight et. al. where the heat flux could be calculated in near real-time and related to the stir temperature through the contact heat transfer coefficient. This was shown to be an effective stir temperature estimation method using a single-piece tool that had a tool substrate ratio of approximately 0.5; a 1 to 2 split of the heat flux where the tool received half of what the substrate did. This approach was duplicated in this work with very different results. It was found that at many times the predicted face temperature was higher than the predicted bulk stir temperature and that this effect was exaggerated in the flat tool case. This conclusion flies in the face of the physics of the problem since, at a theoretical minimum, heat flows into the tool from the stir. This heat is either generated at the boundary or inside of the stir. This result prompted an investigation of the raw data. Below in Figure 21 a comparison of the tool thermocouple and maximum measured substrate data from the flat and pinned case is shown. In the flat tool case in A, the temperature of the thermocouple does not trend with the substrate very closely, resulting in a nearly 150 °C difference. This is contrasted in the pin tool case shown in B where the two temperatures trend very closely. Three possible reasons for this come to mind: 1) The pins protruding into the stir create a better thermal coupling between the tool and the stir resulting in a closer temperature difference. 2) The small amount of pin interaction in the substrate increases the temperature considerably. 3) The pins force a different mechanism of heat generation to dominate than that in the flat tool case.

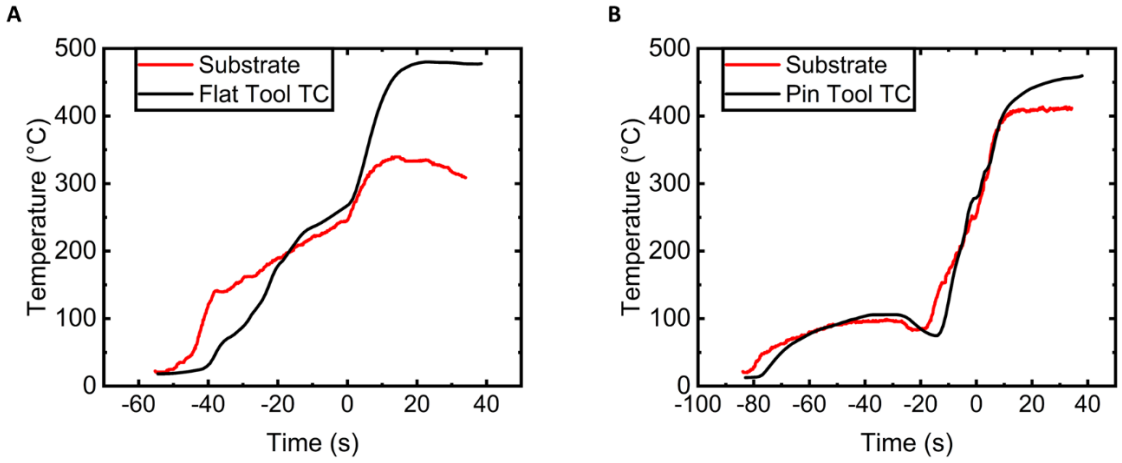

Figure 21 Tool thermocouple temperature and maximum measured substrate temperature for the: A) Flat case. B) Pinned Case.

Option 1 is spurious, since in Knight et. al., it was shown that the pins had relatively poor heat transfer to the tool. It is believed that this is due to the pins pushing a "plug" of material around similar to a built-up edge in machining. Option 2 has more credence since the total power of the stir is higher than in the flat tool case, but the fact that the substrate temperature overtakes the

tool thermocouple temperature in the flat tool case shows that the substrate is not temperature limited by lack of tool interaction. At the same time in the print, 40 seconds before traverse, the flat tool substrate is almost 50 °C hotter than the pin tool substrate. In option 3, the thought is that since the pins are known drivers of plastic deformation more of the heat that is generated comes from plastic deformation rather than tool-stir friction. This is reversed in the flat tool case, where more heat is generated on the boundary rather than the stir interior and therefore is more easily transmitted to the tool. This would explain the difference in the magnitude of the tool-substrate heat flux ratio shown in Figure 18C and F. The flat tool receives a larger percentage of the total heat generated since more of it is generated on the boundary. This also accounts for the variability of the heat generation ratio in the flat tool seen in Figure 19E contrasted with the consistency of the pinned tool. As the temperature changed, the contact conditions evolved under the flat tool. This idea would also explain why the predicted face temperature in the flat tool was at many times higher than the centerline stir temperature. It is thought that the reversed temperature difference was not seen in the single-piece tool case because the greater bulk diffusivity compared to the "heat break" flat tool allowed for either different contact conditions resulting in more area with a lower tool-stir velocity difference (i.e. more stick) or a lower frictional flash temperature [63], [66] decreasing the face temperature. It is also possible that it exhibited a combination of these effects.

With this idea that the flat tool may be experiencing more sliding friction than the pin tool the assumptions behind the predicted face temperature distribution shown in Figure 20 are further called into question. In sliding contact theory, it is assumed that there is some degree of temperature matching on both sides of the interface based on a thermodynamic "zero jump condition" [3], [63], [64], [65], [66], [67] This idea can be numerically treated as a matching maximum temperature or a matching average temperature, but in its strongest form it is considered a point-to-point matching temperature. Since the three-piece tool face has different effective conductivities depending on the radial and circumferential positions, the heat flux into the tool must also change to satisfy the zero-jump condition. At sufficiently high-velocity mismatches between the tool and the stir, the temperature distribution would need to react incredibly quickly since the change between a highly conductive region and a non-highly conductive region would occur very quickly, on the order of 40ms. These two conditions raise more questions than answers and place some very tight requirements concerning a predicted temperature distribution of the stir. A simple uniform or linear heat generation assumption would violate these ideas. The question is also raised if there could be temperature or heat generation oscillations on the time scale of the rotation rate.

Moving Heat Source

Stepping away from ambiguities in the vicinity of the stir tool interface, the process can also be investigated as a simple moving heat source problem with a very poorly understood heat generation rate. In these types of problems, it is important to consider the Peclet number of the problem to understand the regime of heat transfer. This number is a ratio between the advection and the diffusion in a system. In moving heat source problems this number is defined as [68]:

$$Pe = \frac{lv}{2\alpha} \tag{3}$$

Where l is the characteristic length, in this case, taken to be the radius of the tool, v is the velocity of the source, and α is the thermal diffusivity of aluminum. In this work, Peclet numbers of 0.24, 0.48, and 0.72 were considered. These values corresponded to traverse rates of 127 mm/min, 254 mm/min, and 381 mm/min respectively. In moving heat transfer theory, this is a diffusion-dominated regime as opposed to advection. A value of 5 is normally considered to be fully advection-dominated [66]. A diffusion-dominated case causes the propagation of thermal energy in all directions, essentially pre-heating the substrate in front of the tool. This will result in a larger edge effect since the heat will have had more time to pile up resulting in a larger temperature spike. This would be evident when traversing into a corner during a print for example. The opposite is also true, moving faster will result in a shorter pre-heating time and a smaller temperature spike. This is shown most clearly in Figure 19D where increasing traverse rates have smaller power dips toward the end of the print. Much like all things, there is no free lunch. A more advection-dominated print case is expected to have more layer-to-layer thermal strain mismatch since there is less local substrate pre-heating before deposition. This directly leads to increased residual stress.

Looking at the power of this moving heat source is equally confounding. Since both heat generation mechanisms are a function of temperature the power input into the stir is a dependent variable stemming from the rotation rate, feed rate, traverse rate, material properties, and geometry. Interestingly, integrated power, or thermal energy, trends very well with the pseudo heat index employed in friction stir welding. This is shown below in Figure 22. It is believed that each material feed rate, traversal rate, and tool type would fall onto its own curve. That being said, for modeling purposes experimental data would be needed to predict the power and temperature distribution in a part in the absence of a fully coupled CFD model, that also modeled the heat transfer of the part.

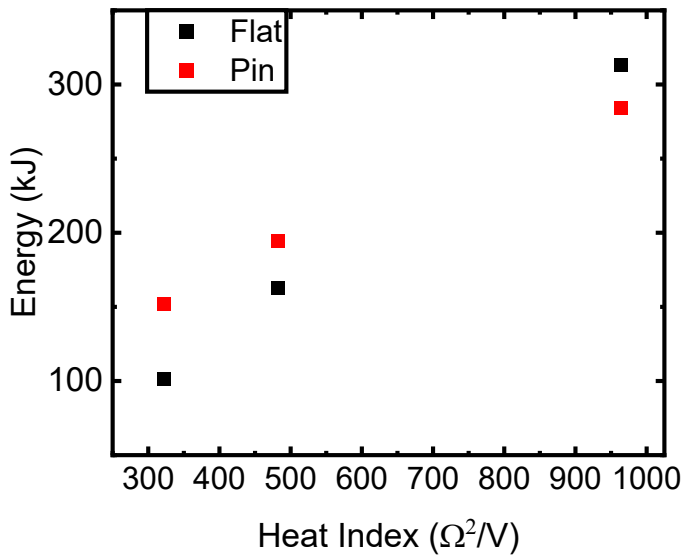

Figure 22 Thermal energy vs pseudo heat index for the flat and pinned case.

Looking at the translation of these findings to practical considerations a few things are evident. Firstly, a changing heat flux ratio will skew any thermocouple reading made by the tool. This has large implications for process control as any temperature setpoint is now governed by the specific geometry being processed, and due to the additive nature of the process, the geometry is always changing. Secondly, since it is believed that the ratio of heat generation mechanisms is a variable based on tool type, the temperature setpoints of a flat tool cannot be carried over to a pinned tool. Taking this a step further, since frictional force is a function of normal force, the exact distribution of the stick-slip coefficient and therefore frictional heat generation is itself a function of the process parameters that affect the hydrostatic pressure of the stir. Unfortunately, one of these parameters is known to be temperature, leading to another fully coupled feedback path. Large questions are also raised about how the temperature of the sliding face satisfies all the conditions imposed on it, calling into question any isothermal, or near isothermal assumptions made relating the face temperature to the temperature any given voxel of material saw while stirring and therefore its validity as a control mechanism. It is also noted that the traversal speed is a double-edged sword, its increase can reduce temperature spikes in corners while simultaneously potentially increasing residual stress.

Conclusions

In this work, the heat distribution in AFSD was investigated using inverse heat transfer during a traversing print. The traversal was implemented with a modern three-piece tool on a substrate that was conducive to inverse analysis. From this study, the total heat generation could be compared to the machine spindle power and the percentage of this power that was conducted into the tool and the substrate was able to be calculated. Comparing the ratio of the power that was conducted either into the substrate or the tool yielded the heat partition value that determines the offset between a tool thermocouple and the temperature of the face. It was found that this ratio is variable and therefore the difference between the tool thermocouple and the face temperature was also variable and was a time-dependent function of geometry and processing parameters. It was shown that simple uniform or linear heat distribution assumptions on the face of the tool lead to inconsistencies in the heat transfer between the stir and the face and that the existence of pins complicated the question further. Finally, the following insights about the production of AFSD printed parts could be concluded:

1) The temperature reading of an embedded thermocouple is inherently disconnected from the process it is designed to measure.
2) The design of the tool for AFSD plays a massive role in heat generation, propagation, and measurement. Small changes in tolerances can stack up to be very meaningful and small manufacturing errors can skew any results.
3) More generally, a single point temperature is currently used as an analogy for heat flux to control AFSD. This type of measurement is plagued from the start due to an incredibly strong dependence on boundary conditions that are driven by minute differences, thus, the error is amplified.

4) The geometry of a substrate and in-progress print will play a key role in the power output through time and heat distribution in an AFSD print.
5) Choosing a pinned versus flat tool can influence the heat generation mechanism and its effects on the metallurgy of a part may not be well understood or captured by current in-situ monitoring techniques.

Manuscript 2 References

[1] F. P. Incropera and D. P. De Witt, “Fundamentals of heat and mass transfer, 2nd edition,” 1990. [Online]. Available: https://api.semanticscholar.org/CorpusID:94205714

[2] A. V. Lykov, *Analytical Heat Diffusion Theory*. Academic Press, 1968.

[3] R. Komanduri and Z. B. Hou, “Analysis of heat partition and temperature distribution in sliding systems,” *Wear*, vol. 251, no. 1–12, pp. 925–938, Oct. 2001, doi: 10.1016/S0043-1648(01)00707-4.

[4] “Inverse Heat Transfer: Fundamentals and Applications - Helcio R.B. Orlande - Google Books.” Accessed: Feb. 11, 2024. [Online]. Available: https://books.google.com/books?hl=en&lr=&id=xEMiEAAAQBAJ&oi=fnd&pg=PP1&ots=WDtHUe5bnd&sig=IfUktFDZnxIJf9XeOKco5BHMK8c#v=onepage&q&f=false

[5] J. V. Beck, B. Litkouhi, and C. R. S. Clair, “EFFICIENT SEQUENTIAL SOLUTION OF THE NONLINEAR INVERSE HEAT CONDUCTION PROBLEM,” *Numeri Heat Transf A Appl*, vol. 5, no. 3, pp. 275–286, 1982, doi: 10.1080/10407788208913448.

[6] N. Daouas and M. S. Radhouani, “A new approach of the Kalman filter using future temperature measurements for nonlinear inverse heat conduction problems,” *Numerical Heat Transfer, Part B: Fundamentals*, vol. 45, no. 6, pp. 565–585, Jun. 2004, doi: 10.1080/10407790490430598.

[7] J. V Beck, B. Blackwell, and C. R. S. C. Jr, *Inverse Heat Conduction: Ill-Posed Problems*, 1st edition. New York: Wiley-Interscience, 1985.

[8] H. Najafi and K. A. Woodbury, “Online heat flux estimation using artificial neural network as a digital filter approach,” *Int J Heat Mass Transf*, vol. 91, pp. 808–817, Dec. 2015, doi: 10.1016/J.IJHEATMASSTRANSFER.2015.08.010.

[9] S. Wan, P. Xu, K. Wang, J. Yang, and S. Li, “Real-time estimation of thermal boundary of unsteady heat conduction system using PID algorithm,” *International Journal of Thermal Sciences*, vol. 153, p. 106395, Jul. 2020, doi: 10.1016/J.IJTHERMALSCI.2020.106395.

[10] M. Zálešák, L. Klimeš, P. Charvát, M. Cabalka, J. Kůdela, and T. Mauder, “Solution approaches to inverse heat transfer problems with and without phase changes: A state-of-the-art review,” *Energy*, vol. 278, p. 127974, Sep. 2023, doi: 10.1016/J.ENERGY.2023.127974.

[11] H. Z. Yu, “Additive Friction Stir Deposition,” *Additive Friction Stir Deposition*, pp. 1–333, Jan. 2022, doi: 10.1016/C2020-0-01505-7.

[12] J. K. Yoder, H. Z. Yu, W. T. Reynolds, W. Cai, L. Li, and V. Blacksburg, “Origins of Embrittlement of an Al-Zn-Mg-Cu Alloy Post Additive Friction Stir Deposition,” Jan. 2023, Accessed: Sep. 15, 2023. [Online]. Available: https://vtechworks.lib.vt.edu/handle/10919/113012

[13] W. D. Hartley *et al.*, “Solid-state cladding on thin automotive sheet metals enabled by additive friction stir deposition,” *J Mater Process Technol*, vol. 291, 2021, doi: 10.1016/j.jmatprotec.2021.117045.

[14] J. K. Yoder, D. J. Erb, R. Henderson, and H. Z. Yu, “Closed-loop temperature controlled solid-state additive manufacturing of Ti-6Al-4V with forging standard out-of-plane tensile properties,” *J Mater Process Technol*, vol. 322, p. 118201, Dec. 2023, doi: 10.1016/J.JMATPROTEC.2023.118201.

[15] D. Z. Avery *et al.*, “Influence of Grain Refinement and Microstructure on Fatigue Behavior for Solid-State Additively Manufactured Al-Zn-Mg-Cu Alloy,” *Metall Mater Trans A Phys Metall Mater Sci*, vol. 51, no. 6, 2020, doi: 10.1007/s11661-020-05746-9.

[16] G. G. Stubblefield, K. Fraser, B. J. Phillips, J. B. Jordon, and P. G. Allison, “A meshfree computational framework for the numerical simulation of the solid-state additive manufacturing process, additive friction stir-deposition (AFS-D),” *Mater Des*, vol. 202, 2021, doi: 10.1016/j.matdes.2021.109514.

[17] B. J. Phillips *et al.*, “Microstructure-deformation relationship of additive friction stir-deposition Al–Mg–Si,” *Materialia (Oxf)*, vol. 7, p. 100387, Sep. 2019, doi: 10.1016/J.MTLA.2019.100387.

[18] K. C. Kincaid, D. W. MacPhee, G. G. Stubblefield, J. B. Jordon, T. W. Rushing, and P. G. Allison, “A Finite Volume Framework for the Simulation of Additive Friction Stir Deposition,” *J Eng Mater Technol*, vol. 145, no. 3, Jul. 2023, doi: 10.1115/1.4056642.

[19] N. Gotawala and H. Z. Yu, “Material flow path and extreme thermomechanical processing history during additive friction stir deposition,” *J Manuf Process*, vol. 101, pp. 114–127, Sep. 2023, doi: 10.1016/J.JMAPRO.2023.05.095.

[20] P. C. Metz *et al.*, “Heterogeneous microstructure development in additive friction-stir deposited Al-Mg-Si alloy,” 2024, doi: 10.1016/j.addma.2024.103989.

[21] B. A. Rutherford *et al.*, “metals Effect of Thermomechanical Processing on Fatigue Behavior in Solid-State Additive Manufacturing of Al-Mg-Si Alloy”, doi: 10.3390/met10070947.

[22] G. D. Hahn, K. P. Knight, N. Gotawala, and H. Z. Yu, “Additive friction stir deposition of AA7050 achieving forging-like tensile properties,” *Materials Science and Engineering: A*, vol. 896, p. 146268, Mar. 2024, doi: 10.1016/J.MSEA.2024.146268.

[23] M. B. Williams *et al.*, “Towards Understanding the Relationships between Processing Conditions and Mechanical Performance of the Additive Friction Stir Deposition Process,” *Metals 2023, Vol. 13, Page 1663*, vol. 13, no. 10, p. 1663, Sep. 2023, doi: 10.3390/MET13101663.

[24] G. R. Merritt, M. B. Williams, P. G. Allison, J. B. Jordon, T. W. Rushing, and C. A. Cousin, “Closed-Loop Temperature and Force Control of Additive Friction Stir

Deposition," *Journal of Manufacturing and Materials Processing*, vol. 6, no. 5, 2022, doi: 10.3390/jmmp6050092.

[25] R. Sanders and J. Staley, "A History of Wrought Aluminum Alloys and Applications," in *Properties and Selection of Aluminum Alloys*, ASM International, 2019, pp. 157–201. doi: 10.31399/asm.hb.v02b.a0006516.

[26] Battelle Memorial Institute., "Metallic Materials Properties Development and Standardization (MMPDS-2023)".

[27] E. A. Starke and J. T. Staley, "Application of modern aluminium alloys to aircraft," in *Fundamentals of Aluminium Metallurgy: Production, Processing and Applications*, Elsevier Ltd., 2010, pp. 747–783. doi: 10.1533/9780857090256.3.747.

[28] H. Z. Yu *et al.*, "Non-beam-based metal additive manufacturing enabled by additive friction stir deposition," *Scr Mater*, vol. 153, pp. 122–130, Aug. 2018, doi: 10.1016/j.scriptamat.2018.03.025.

[29] H. Z. Yu and R. S. Mishra, "Additive friction stir deposition: a deformation processing route to metal additive manufacturing," *Mater Res Lett*, vol. 9, no. 2, 2021, doi: 10.1080/21663831.2020.1847211.

[30] J. K. Yoder, R. J. Griffiths, and H. Z. Yu, "Deformation-based additive manufacturing of 7075 aluminum with wrought-like mechanical properties," *Mater Des*, vol. 198, Jan. 2021, doi: 10.1016/j.matdes.2020.109288.

[31] A. M. Vest, D. R. St-Pierre, S. Rock, A. M. Maniatty, D. J. Lewis, and S. J. A. Hocker, "Thermocouple Temperature Measurements in Selective Laser Melting Additive Manufacturing", Accessed: Feb. 11, 2024. [Online]. Available: http://www.sti.nasa.gov

[32] B. Müller, ; U Renz, B. Mü Ller, and U. Renz, "Development of a fast fiber-optic two-color pyrometer for the temperature measurement of surfaces with varying emissivities," *Review of Scientific Instruments*, vol. 72, no. 8, pp. 3366–3374, Aug. 2001, doi: 10.1063/1.1384448.

[33] A. Lerner *et al.*, "Laser Powder Bed Fusion thermal monitoring using optical fiber sensors: in situ measurements and modelling," *2023 Conference on Lasers and Electro-Optics Europe and European Quantum Electronics Conference, CLEO/Europe-EQEC 2023*, 2023, doi: 10.1109/CLEO/EUROPE-EQEC57999.2023.10232209.

[34] C. Krishna, P. Vallabh, and X. Zhao, "Melt pool temperature measurement and monitoring during laser powder bed fusion based additive manufacturing via single-camera two-wavelength imaging pyrometry (STWIP)," *J Manuf Process*, vol. 79, pp. 486–500, 2022, doi: 10.1016/j.jmapro.2022.04.058.

[35] B. Bevans *et al.*, "Heterogeneous sensor data fusion for multiscale, shape agnostic flaw detection in laser powder bed fusion additive manufacturing," *Virtual Phys Prototyp*, vol. 18, no. 1, Dec. 2023, doi: 10.1080/17452759.2023.2196266.

[36] J. Petrich, Z. Snow, D. Corbin, and E. W. Reutzel, “Multi-modal sensor fusion with machine learning for data-driven process monitoring for additive manufacturing,” *Addit Manuf*, vol. 48, p. 102364, Dec. 2021, doi: 10.1016/J.ADDMA.2021.102364.

[37] P. K. Rao, J. Liu, D. Roberson, Z. Kong, and C. Williams, “Online Real-Time Quality Monitoring in Additive Manufacturing Processes Using Heterogeneous Sensors,” *Journal of Manufacturing Science and Engineering, Transactions of the ASME*, vol. 137, no. 6, Dec. 2015, doi: 10.1115/1.4029823/374977.

[38] K. J. Colligan and R. S. Mishra, “A conceptual model for the process variables related to heat generation in friction stir welding of aluminum,” *Scr Mater*, vol. 58, no. 5, pp. 327–331, Mar. 2008, doi: 10.1016/j.scriptamat.2007.10.015.

[39] W. D. Hartley and S. W. Case, “Processing Mechanics of Additive Friction Stir Deposition.”

[40] S. H. Mousavi Anijdan, H. R. Madaah-Hosseini, and A. Bahrami, “Flow stress optimization for 304 stainless steel under cold and warm compression by artificial neural network and genetic algorithm,” *Mater Des*, vol. 28, no. 2, pp. 609–615, Jan. 2007, doi: 10.1016/J.MATDES.2005.07.018.

[41] K. A. Fraser, “Robust and efficient meshfree solid thermo-mechanics simulation of friction stir welding,” 2017.

[42] K. Kumar, C. Kalyan, S. V. Kailas, and T. S. Srivatsan, “An Investigation of Friction During Friction Stir Welding of Metallic Materials,” *Materials and Manufacturing Processes*, vol. 24, no. 4, pp. 438–445, Apr. 2009, doi: 10.1080/10426910802714340.

[43] A. F. Hasan, C. J. Bennett, P. H. Shipway, S. Cater, and J. Martin, “A numerical methodology for predicting tool wear in Friction Stir Welding,” *J Mater Process Technol*, vol. 241, pp. 129–140, Mar. 2017, doi: 10.1016/J.JMATPROTEC.2016.11.009.

[44] S. Mandal, J. Rice, G. Hou, K. M. Williamson, and A. A. Elmustafa, “Modeling and simulation of a donor material concept to reduce tool wear in friction stir welding of high-strength materials,” *J Mater Eng Perform*, vol. 22, no. 6, pp. 1558–1564, Jun. 2013, doi: 10.1007/S11665-012-0452-4/FIGURES/10.

[45] J. Zhang, P. Upadhyay, Y. Hovanski, and D. P. Field, “High-Speed Friction Stir Welding of AA7075-T6 Sheet: Microstructure, Mechanical Properties, Micro-texture, and Thermal History”, doi: 10.1007/s11661-017-4411-4.

[46] G. R. Merritt, M. B. Williams, P. G. Allison, J. B. Jordon, T. W. Rushing, and C. A. Cousin, “Closed-Loop Temperature and Force Control of Additive Friction Stir Deposition,” *Journal of Manufacturing and Materials Processing*, vol. 6, no. 5, Oct. 2022, doi: 10.3390/jmmp6050092.

[47] Z. T. Niu, H. Qi, Y. K. Ji, S. Wen, Y. T. Ren, and M. J. He, “Real-time reconstruction of thermal boundary condition of porous media via temperature sequence,” *International Journal of Thermal Sciences*, vol. 177, Jul. 2022, doi: 10.1016/j.ijthermalsci.2022.107570.

[48] D. Lu and C. Wang, “Three-dimensional temperature field inversion calculation based on an artificial intelligence algorithm,” *Appl Therm Eng*, vol. 225, May 2023, doi: 10.1016/j.applthermaleng.2023.120237.

[49] S. Motahar, “Experimental study and ANN-based prediction of melting heat transfer in a uniform heat flux PCM enclosure,” 2020, doi: 10.1016/j.est.2020.101535.

[50] C. Fieberg and R. Kneer, “Determination of thermal contact resistance from transient temperature measurements,” *Int J Heat Mass Transf*, vol. 51, no. 5–6, pp. 1017–1023, Mar. 2008, doi: 10.1016/j.ijheatmasstransfer.2007.05.004.

[51] A. Bejan and A. D. Kraus, *Heat transfer handbook*. J. Wiley, 2003.

[52] M. Nouari, B. Haddag, A. Moufki, and S. Atlati, “Investigation on the built-up edge process when dry machining aeronautical aluminum alloys,” *Machining of Light Alloys*, pp. 35–48, Aug. 2018, doi: 10.1201/B22153-2.

[53] R. Nandan, T. Debroy, and H. K. D. H. Bhadeshia, “Recent advances in friction-stir welding-Process, weldment structure and properties”, doi: 10.1016/j.pmatsci.2008.05.001.

[54] R. Nandan, G. G. Roy, T. J. Lienert, and T. Debroy, “Three-dimensional heat and material flow during friction stir welding of mild steel,” *Acta Mater*, vol. 55, no. 3, pp. 883–895, Feb. 2007, doi: 10.1016/J.ACTAMAT.2006.09.009.

[55] K. Fraser, L. I. Kiss, L. St-Georges, and D. Drolet, “Optimization of friction stir weld joint quality using a meshfree fully-coupled thermo-mechanics approach,” *Metals (Basel)*, vol. 8, no. 2, Feb. 2018, doi: 10.3390/MET8020101.

[56] S. Solhjoo, “Revisiting the Common Practice of Sellars and Tegart’s Hyperbolic Sine Constitutive Model,” *Modelling 2022, Vol. 3, Pages 359-373*, vol. 3, no. 3, pp. 359–373, Aug. 2022, doi: 10.3390/MODELLING3030023.

[57] G. G. Stubblefield *et al.*, “Ballistic Evaluation of Aluminum Alloy (AA) 7075 Plate Repaired by Additive Friction Stir Deposition Using AA7075 Feedstock,” *Journal of Dynamic Behavior of Materials*, vol. 9, no. 1, pp. 79–89, Mar. 2023, doi: 10.1007/s40870-022-00363-6.

[58] C. J. T. Mason *et al.*, “Process-structure-property relations for as-deposited solid-state additively manufactured high-strength aluminum alloy,” *Addit Manuf*, vol. 40, Apr. 2021, doi: 10.1016/j.addma.2021.101879.

[59] R. S. Mishra, R. S. Haridas, and P. Agrawal, “Friction stir-based additive manufacturing,” *Science and Technology of Welding and Joining*, vol. 27, no. 3. Taylor and Francis Ltd., pp. 141–165, 2022. doi: 10.1080/13621718.2022.2027663.

[60] R. S. Mishra and M. Komarasamy, *Physical Metallurgy of 7XXX Alloys*. Elsevier, 2016. doi: 10.1016/b978-0-12-809465-5.00002-7.

[61] M. Schöbel, P. Pongratz, and H. P. Degischer, "Coherency loss of Al 3(Sc,Zr) precipitates by deformation of an Al-Zn-Mg alloy," *Acta Mater*, vol. 60, no. 10, pp. 4247–4254, Jun. 2012, doi: 10.1016/j.actamat.2012.04.011.

[62] A. Zubelewicz, "Century-long Taylor-Quinney interpretation of plasticity-induced heating reexamined," *Scientific Reports 2019 9:1*, vol. 9, no. 1, pp. 1–7, Jun. 2019, doi: 10.1038/s41598-019-45533-0.

[63] V. L. Popov, "Thermal Effects in Contacts," *Contact Mechanics and Friction*, pp. 199–205, 2010, doi: 10.1007/978-3-642-10803-7_13.

[64] B. H., "Theoretical Study of Temperature Rise at Surfaces of Actual Contact under Oiliness Lubricating Conditions," *Proc. Instn. Mech. Engrs. (General discussion on lubrication and lubricants)*, vol. 2, pp. 222-, 1937, Accessed: Mar. 11, 2024. [Online]. Available: https://cir.nii.ac.jp/crid/1573668924965107328

[65] J. C. Jaeger and J. C. Jaeger, "Moving sources of heat and the temperature at sliding contacts," *Journal and proceedings of the Royal Society of New South Wales*, vol. 76, no. 3, pp. 203--224, May 1943, doi: 10.5962/p.360338.

[66] K. J. Zwick and M. Tate, "Flash Temperature Theory," *Encyclopedia of Tribology*, pp. 1182–1194, 2013, doi: 10.1007/978-0-387-92897-5_1312.

[67] D. G. Bansal and J. L. Streator, "A method for obtaining the temperature distribution at the interface of sliding bodies," *Wear*, vol. 266, no. 7–8, 2009, doi: 10.1016/j.wear.2008.08.019.

[68] M. Akbari, D. Sinton, and M. Bahrami, "Moving heat sources in a half space: Effect of source geometry," *Proceedings of the ASME Summer Heat Transfer Conference 2009, HT2009*, vol. 3, pp. 685–694, 2009, doi: 10.1115/HT2009-88562.

[69] R. Mendoza, "In-service Corrosion Issues in Sustainment of Naval Aircraft," 2012.

[70] R. Joey Griffiths, D. T. Petersen, D. Garcia, and H. Z. Yu, "Additive friction stir-enabled solid-state additive manufacturing for the repair of 7075 aluminum alloy," *Applied Sciences (Switzerland)*, vol. 9, no. 17, Sep. 2019, doi: 10.3390/app9173486.

[71] M. E. J. Perry, R. J. Griffiths, D. Garcia, J. M. Sietins, Y. Zhu, and H. Z. Yu, "Morphological and microstructural investigation of the non-planar interface formed in solid-state metal additive manufacturing by additive friction stir deposition," *Addit Manuf*, vol. 35, Oct. 2020, doi: 10.1016/j.addma.2020.101293.

[72] M. E. J. Perry *et al.*, "Tracing plastic deformation path and concurrent grain refinement during additive friction stir deposition," *Materialia (Oxf)*, vol. 18, Aug. 2021, doi: 10.1016/j.mtla.2021.101159.

[73] C. C. De Castro *et al.*, “Tool wear mechanisms and effects on refill friction stir spot welding of AA2198-T8 sheets,” *Journal of Materials Research and Technology*, vol. 20, pp. 857–866, Sep. 2022, doi: 10.1016/J.JMRT.2022.07.092.

[74] Q. Chu *et al.*, “On visualizing material flow and precipitate evolution during probeless friction stir spot welding of an Al-Li alloy,” *Mater Charact*, vol. 144, pp. 336–344, Oct. 2018, doi: 10.1016/J.MATCHAR.2018.07.026.

[75] “Wrought Aluminum Alloys: Atlas of Fractographs,” in *Fractography*, ASM International, 2018, pp. 414–439. doi: 10.31399/asm.hb.v12.a0000621.

4 Chapter 4: Thermal Control of Solid-State Repair

In this chapter, a step forward in the ongoing repair work of the Yu group is presented. This is a single step in a long-standing project to leverage the solid-state nature of the AFSD process to extend the life of U.S. Navy aircraft components that have had small but significant amounts of corrosion in bolt holes. Using the understanding from the previous two chapters it is apparent that one of the most critical variables in the AFSD process is the thermal boundary condition. In this work, the thermal boundary is experimentally modified to understand its effects on the fatigue life of a hole repair. Metallurgical effects from these different thermal conditions and future process considerations are shown.

4.1 Manuscript 3: Effect of Support Geometry on the AFSD Repair of Corroded AA7050 Through Holes

Kendall P. Knight, Greg Hahn, Luke Hagedorn, Mark Pandol, Hang Yu

Abstract

In Naval aircraft, corrosion-induced defects form around through holes, substantially compromising their mechanical integrity and fatigue life. This paper presents a step forward for repairing corroded fastener holes in metallic substrates to improve fatigue properties. Additive friction stir deposition (AFSD) was employed to fill the corroded holes, effectively restoring the structural integrity, and enhancing the fatigue resistance of the repaired areas. Additionally, active cooling techniques were applied to optimize microstructural refinement and mechanical properties, resulting in superior fatigue performance compared to traditional repair methods. The synergistic effect of AFSD and active cooling was investigated through a comprehensive characterization of the repaired samples, including microstructural analysis, in-situ monitoring, and fatigue testing. The findings demonstrate the potential of this combined approach to significantly enhance the fatigue life and durability of corroded structures, offering promising prospects for future applications in aerospace, automotive, and other critical industries.

Introduction

Corrosion in Naval aircraft creates a taxpayer burden of over $2.5 Billion per year and drives questions about the operational safety of air systems and their sustainment and mission readiness [69]. The harsh maritime environment encountered by Naval aircraft, with sea spray, salty air, and humidity, drives the corrosion of structures at an accelerated rate. Among the challenges of corrosion in structural components is that of corroding through holes. These holes are often found as bolt holes to interlock components. When these holes corrode to a size that is no longer acceptable the first line of defense is to drill out the corrosion and then press fit a bushing into the hole. This provides a geometric repair, i.e. makes the hole the original size, however, the lack of mechanical bonding decreases the fatigue lifetime of the component leading to a lower number of service hours. If the corrosion returns or the component hits its service hour ceiling the entire component must be replaced. This accelerated replacement of expensive, forged components creates an opportunity for great cost savings if these trouble spots can be eliminated. A potential path to repair these holes is through additive friction stir deposition.

Additive friction stir deposition (AFSD) is a novel solid-state additive manufacturing process that employs the friction stir principle to deposit material [28], [29], [30]. In addition to printing

wholesale components, this process has been previously leveraged to repair corroded through holes with good fatigue properties [15], [70]. The large amount of material flow caused by AFSD creates a strong interfacial bond between the added material and the original material [15], [16], [71], [72]. Previous works have shown the feasibility of using AFSD to repair holes, first by Griffiths et. al. in AA7075 as proof of concept. Later, good fatigue results combined with microstructural investigations of the mechanism behind the good repair life were shown by Hahn and Knight et. al. In this previous work by Hahn et. al., hereafter referred to as the nominal repair, three AA7050 coupon geometries were employed. One with a 7.937mm (5/16”) hole hereafter referred to as the 5/16” hole. One with a 6.35mm (1/4”) hole hereafter referred to as the 1/4” hole, and one with a 5/16” hole that had been repaired using AFSD and then machined and redrilled to 1/4” hereafter referred to as the repaired coupon. Ten of each coupon were fatigue tested at loading ratios of R=-1 and R=0.1 for a total of 60 coupons tested. For the case of R=0.1 the repaired coupon, on average, outlasted both the 5/16” hole and the ¼” hole. This meant that the repair was better than new material in fatigue. However, in the case of R=-1, the repair was only able to outlast the 5/16” hole meaning that the repair was not as good as the pristine sample made from rolled plate but was better than no repair to the 5/16” hole at all. This inability to beat new material in one but not both cases means that there is potential for further optimization. Additionally, Hahn provided no investigation of thermal mechanisms that could be driving the results seen in fatigue.

The components under investigation in this work and the ones before it are made of AA7050. This is a high-strength precipitation hardened aluminum alloy with a hierarchical microstructure. The structures in this alloy exist on several length scales, from iron-rich constituent particles left over as contamination from the melt on the 10-100 micron scale to Zr-based dispersoid particles designed to be high-temperature grain stabilizers at the 10-30 nanometer scale [27]. Finally, the $MgZn_2$ or η strengthening phase that precipitates after heat treatment exists in the range of single nanometers [27]. The morphology of these precipitates has been thoroughly studied outside of this work, with much of the understanding of AA7050 coming from Mishra. These structures come together to form an alloy with low quench sensitivity and a high strength-to-weight ratio. AA7050 is also corrosion resistant, typically deployed in the T7x temper. This is a slightly overaged configuration that lends itself well to resisting fatigue and corrosion [26]. Due to its low density and high-performance characteristics and relatively low cost, aircraft structural components that experience lower operating temperatures and are needed in thick sections are commonly made from this alloy [60].

Materials and Methods

Materials and Manufacturing

The AA7050-T7451 plate used for both the substrate and feedstock was sourced from Tri-Tech Metals (Rancho Cucamonga, CA, USA). These materials were fashioned into 76.2 mm x 152.4 mm x 6.35 mm coupons where the long direction corresponded to the rolling direction of the plate. 152.4 mm x 9.525 mm x 9.525 mm feed rods were also made from the plate. These geometries were exactly those used by Hahn et.al.

Additive friction stir deposition was carried out on a MELD R2 system (MELD Manufacturing, Christiansburg VA, USA). For all prints, a tool with four 2.29mm high teardrop features in the face was used. To execute the repair, Hahn et. al. have previously used a discrete piece of steel measuring 1.27mm x 25.4mm x 76.2 mm to support the gauge section of the coupon while it is clamped to a steel fixture during the AFSD repair. A cross-section of this nominal repair process is shown in Figure 23a. This piece of steel is known as the backing, the geometry of this is critical as material not constrained by the backing flows down to meet the clamp fixture. In the nominal repair, material flow occurred on the top and bottom of the coupon and not on the sides, this can be seen on the backside of the pre-machined configuration shown in Figure 23b. The actual repair printing was conducted in the exact same manner as the method described in Hahn et. al.

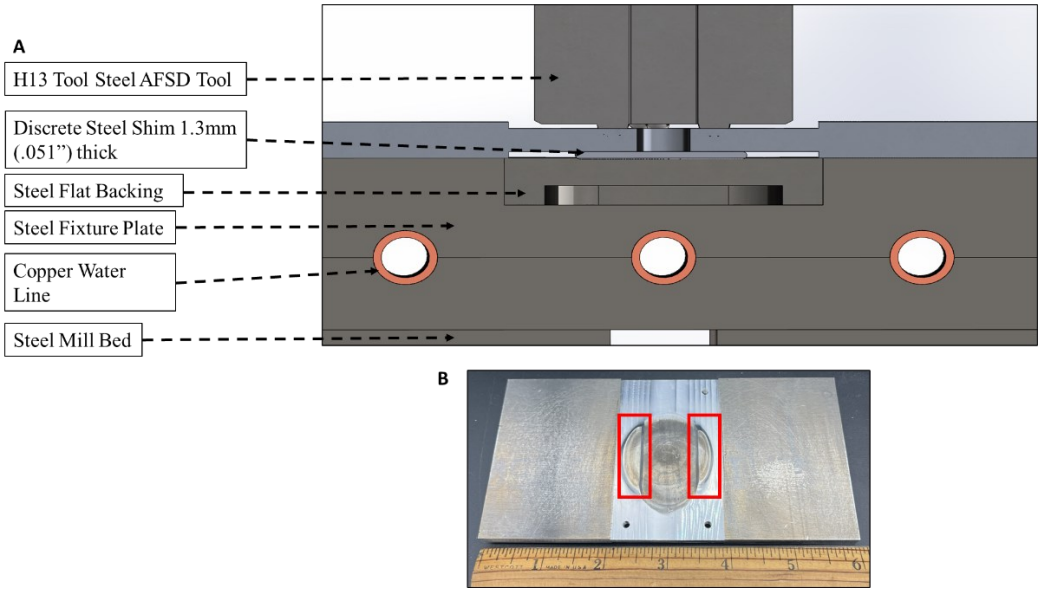

Figure 23 A) Schematic of the nominal repair from Hahn et. al. showing the distinct pieces of the fixturing. B) Photograph of a repair with the flow along the top and bottom circled in red.

In these experiments, six new backing plate geometries were tested to understand the effects of material flow around the repair. These new backing plates were made of a single piece of steel that was bolted into the clamp fixture, taking the place of the part labeled “steel flat backing” in Figure 23Figure 24a. Below in Figure 24a the six backing plates are shown, and Figure 24b-g show cross-sections of the geometries. The Old Shim backing plate shown in Figure 24b was considered as a control as it had the same geometry as the backing in the nominal repair, except it was made of a single piece of steel, thus eliminating one thermal barrier. Additionally, active cooling was used at the end of the repair to cool the repair and clamp fixture back down to ambient temperature faster. This active cooling was accomplished by plumbing a large reservoir of cold water into the copper lines embedded in the clamp fixture and pumping that cold water through. The same clamp fixture was used for both the nominal repairs in Hahn et. al. and the repairs in this work. In the work of Hahn et. al., these cooling channels did not have water in them, and no water was forced through.

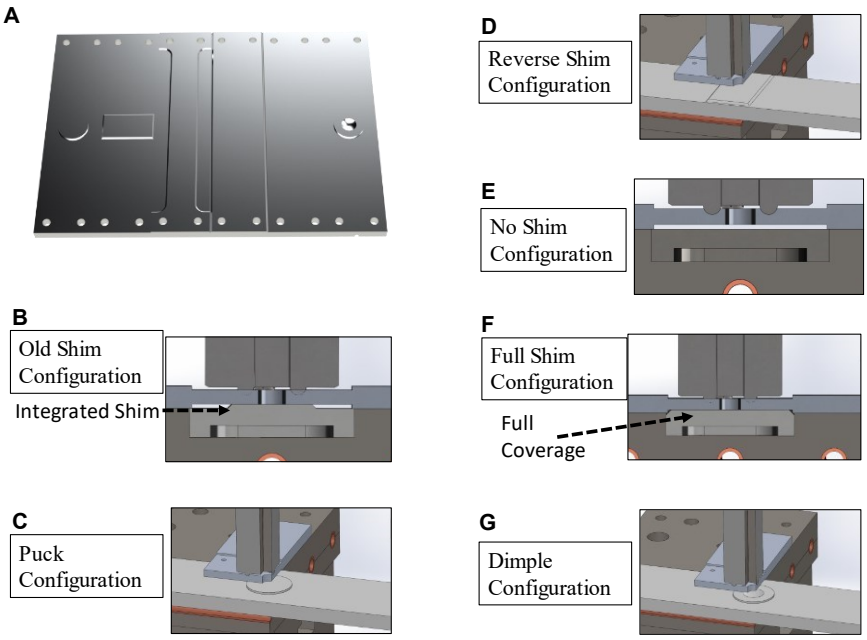

Figure 24 A) Side-by-side rendering of each of the backing plate geometries. From left to right: Puck, Reverse Shim, Old Shim, Full Shim, No Shim, Dimple. B) Cross-section of the old shim configuration. Note the same shape as the nominal repair but made of one piece of metal. C) Quarter view of the puck configuration. D) Quarter view of the reverse shim configuration. E) Quarter view of the No Shim configuration. Note the lack of support underneath the coupon at the start. After printing the coupon partially collapses into this area. F) Cross-section of the Full Shim. Note that the entire gauge section is constrained. G) Quarter view of the Dimple.

For each backing configuration. four repairs were conducted, three were drilled and reamed back to the nominal ¼" size and fatigue tested, and the fourth was machined to size but not drilled and held for microstructural characterization. Before fatigue testing and microscopy, all samples were naturally aged for three months post-deposition.

Process Monitoring

Each of these repairs had three type K thermocouples mounted at consistent locations on the surface by compressing the bead of the thermocouple under a #6-32 screw. This compression ensured quality thermal contact without the added uncertainty of thermal paste. The downside to this contact is the fact the thermocouple is influenced by the temperature of the screw. This is mitigated by using a short, and small diameter screw. These placements of the thermocouple corresponded to the same placements as the nominal repair, approximately 5mm from the edge of the stir. A drawing of the thermocouple placements is shown in Appendix 1. Data from these thermocouples was recorded at 3Hz. Additionally, the spindle torque, power, and actuator force were recorded at a rate of 1Hz during the print directly from the machine. Data from the torque and power was baseline corrected to only reflect power delivered into the stir rather than frictional losses in the drivetrain and bearings.

Mechanical Testing and Characterization

Fatigue specimens were polished parallel to the loading direction with SiC polishing stones and a 4:1 mixture of WD-40® and Marvel Mystery Oil®. All surfaces were first polished with a 220-grit stone, then the gauge section was polished with a 400-grit stone. Care was given not to disturb the edge of the hole in the gauge section. Force-controlled fatigue testing was conducted on an MTS 810 with a 50kN load cell (Eden Prairie, MN, USA). Fatigue testing occurred at a loading ratio of R= -1 in load control at a nominal stress of 134 MPa cycled at 5Hz. This loading matches the fatigue testing for the R=-1 nominal repair. During fatigue testing, the peak displacement at each cycle was measured and recorded by the MTS controller. After fatigue testing broken samples were observed under an SEM (JEOL IT500HR, Tokyo, Japan) to examine the fracture surface to understand the crack propagation mode.

The remaining fourth coupon was first polished and electro-etched with Barker's Reagent as described in ASTM E407 and examined with optical microscopy under polarized light on a Keyence VHX-7000 (Osaka, Japan) digital microscope. After optical investigations, the coupons were mechanically polished with a 1200-grit SiC polishing pad. They were then electropolished with a LN_2-cooled 70% methanol 30% Nitric Acid electrolyte at 30V for 30 seconds. Electron backscatter diffraction (EBSD) was conducted (FEI Helios 600 NanoLab, Thermo Fisher, Waltham, USA at regions of interest from the optical images.

Once all EBSD and optical microscopy had been conducted, a 3mm plug was cut via sinker EDM out of the Old Shim control sample. This plug was cut via a diamond wafering blade and mechanically thinned to approximately 100 μm before final electrothinning. Electrothinning was conducted utilizing a twinjet system and the same LN_2-cooled electrolyte previously mentioned. This thinned sample was then investigated using Scanning transmission electron microscopy (STEM) (Themis, Thermo Fisher, Waltham, USA)

Results

In-Situ Trends

Looking at the thermal results, a clear difference in the maximum temperature of the groups can be seen along with a difference in the maximum temperature of the nominal repair. This data can be seen in the bar plot of Figure 25a. The lower maximum temperature than the nominal repair is due to the removal of the thermal barrier of the shim to the backing plate. Removing that interface by making the shim and backing plate from one contiguous piece of material increases the heat transfer efficiency from the stirring material to the rest of the environment. The small differences in maximum temperature between the actively cooled groups are driven by the interplay of heat generation, material flow, and heat transfer efficiency of the backing plate. These variables play into the fully coupled thermo-mechanical system that links strain, strain rate, temperature, and heat generation.

Looking at the time-dependent temperature shown in Figure 25b a clear difference can be seen between the nominal repair and the actively cooled repairs. The temperature vs time curve in Figure 25b was taken from the same location on the coupon in both the nominal and the old shim configuration. This curve shows data from the start of the repair to the end of printing as well as the cooling of the coupon with the cooling region marked in black. The cooling region of the

temperature vs time plot for the same point on each of the four runs for each of the six groups plus the nominal repair can be empirically fit by an equation of the form $T(t) = at^b + c$. Averaged values of the coefficient b which is inversely related to the cooling rate are shown for each group in Figure 25c. The shape of the backing does not strongly influence the cooling rate or the maximum temperature, however having the integrated backing uniformly lowers the maximum temperature. In every case, the nominal repair has a higher maximum temperature and a slower cooling rate. The integral of the spindle power curve is plotted for each group in Figure 25d. This is the mechanical energy of each print averaged across each group. It can be seen that the nominal repair had lower energy input than the rest of the actively cooled coupons, but it also had a much higher average temperature. This is primarily due to the improved conduction path created from the integrated backing plate design. More thermal energy leaving the stir through the backing means that more must be added via spindle torque to adequately stir the deposit. The spindle power is not fixed in this scenario is not fixed and will change based on the nonlinear material response [43], [55], [56]. This means that whenever the boundary conditions are changed the power of the stir and thermal field will change in a fully coupled manner.

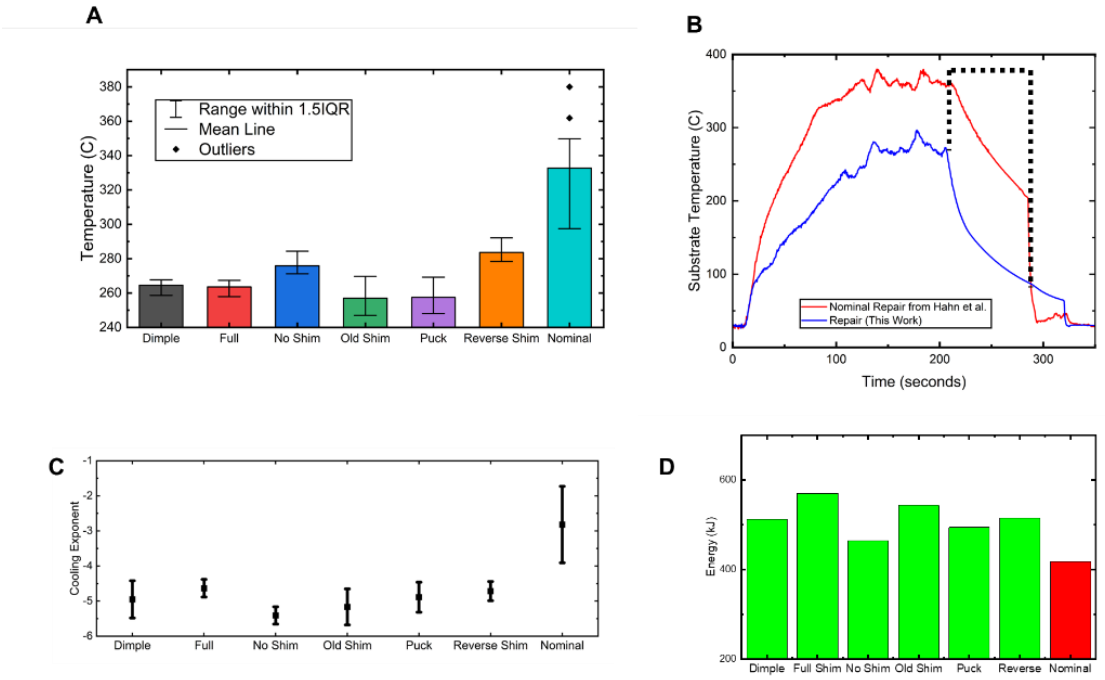

Figure 25 A) Bar chart showing the average and standard deviation of the maximum repair temperature for each group as recorded by a substrate thermocouple. B) Temperature vs time comparison of the Nominal repair and an Old Shim repair from this work. Note the cooling region notated in black. C) The average of the exponent from the empirical curve fits. Note a more negative number means a faster cooling rate. D) The energy input into the stir averaged across all the repairs from each group and the nominal.

Fatigue

The fatigue data for each group is shown below in Figure 26a. Between the six backing plate configurations there is little visible difference. Using a one-way ANOVA test shows no

statistically significant difference in the lifetimes between the groups. It is important to note that the number of samples used here is a minimum and can only detect large variability due to the scattered nature of fatigue testing. For a more confident fatigue life prediction somewhere on the order of 30 more tests would need to be run for each group [26]. Looking in context at the nominal repair and the 1/4" pristine sample, Figure 26b shows a large fatigue life improvement if all the configurations are considered to be a single actively cooled group. There is significant enough improvement where the 60% lifetime of the actively cooled repair outperforms pristine AA7050-T7541 in an R=-1 loading condition. The 60% lifetimes from Hahn et. al and this work are shown below in Table 2. Looking at the values, the actively cooled repair lasts 2,945 cycles or 20% longer than the pristine 1/4" baseline made from rolled plate. In other words, the repair is 20% better than new and outperforms the nominal repair from Hahn et al. by 51%.

Table 2 60% lifetimes from Hahn et. al. and this work.

	5/16" Baseline	1/4" Baseline	Nominal Repair [x]	Actively Cooled Repair
60% Lifetime (CTF)	9,409	14,141	11,307	17,086

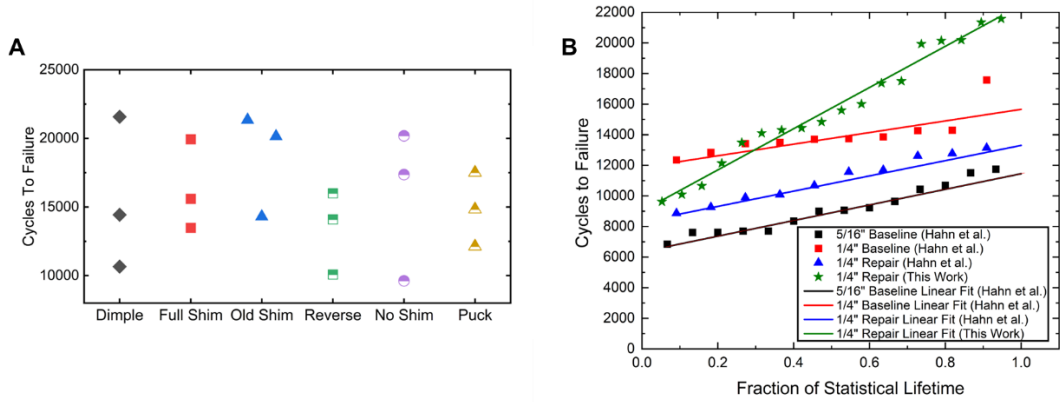

Figure 26 A) Raw cycles to failure data for each of the fatigue tests in this work. B) Weibull plots of the repairs in this work as considered to be a single group along with the repairs and baselines from Hahn et. al. Note a larger slope implies more statistical uncertainty of the actual lifetime for a given sample.

Optical

Observing the flow in the polarized light optical images shown in Figure 27a-f shows little difference in the flow patterns between groups (Note color differences within an image are representative of flow, however, color differences image to image are a result of etchant exposure length). All images are annotated with the 1/4" hole wall (i.e. the hole wall if the coupon was drilled to the test configuration) and the previous 5/16" hole wall (i.e. the hole wall before the

repair occurred). All configurations contain the same general types of flow features that are seen in the nominal repair. These consist of a region of deposited material, a blended region, a pin-affected zone, and a non-fully recrystallized region. This non-recrystallized region is the thermo-mechanically affected zone (TMAZ) where remnants of the original texture of the rolled plate can be seen. In general, the flow of the backing plate groups, and the nominal repair are the same. The exception to this is in Figure 27b and Figure 27f where on the bottom right side, the TMAZ has been rotated due to flow over the circular cross-section of the Puck and Dimple backing plates respectively.

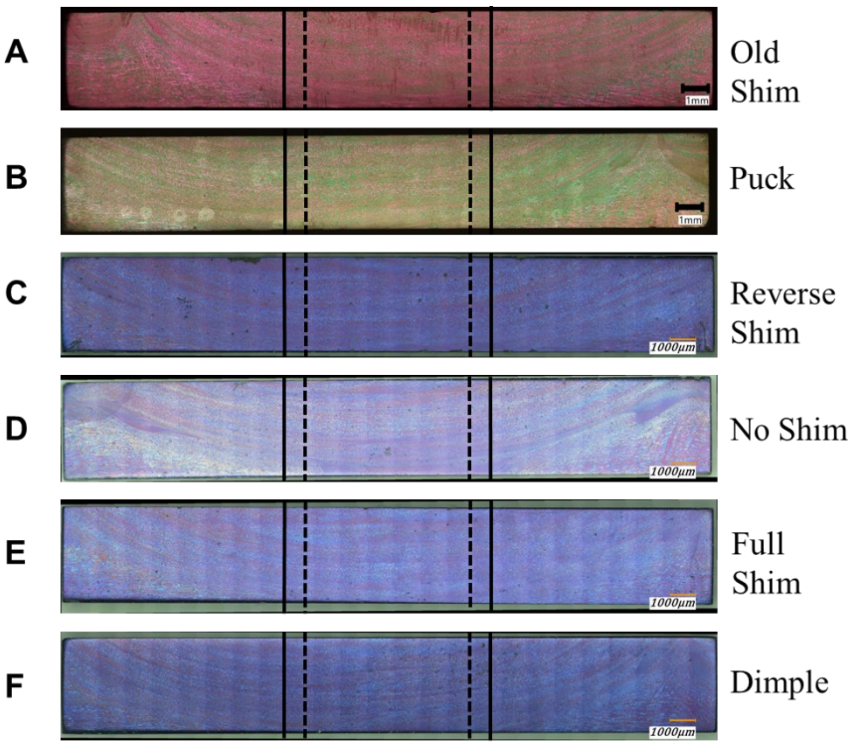

Figure 27 Polarized optical micrographs showing a sample of each one of the repair configurations. In this orientation, the tool would be on the top.

EBSD

Based on the features seen in these optical images, EBSD was conducted at specific regions of interest around the samples. A map of the location of the scan regions is shown in Figure 28. These locations were replicated in all samples. In Figure 29a-f the misorientation plot, inverse pole figure (IPF), and kernel average misorientation (KAM) from all locations in the Old Shim configuration are shown. These locations correspond to locations A-F in Figure 28.

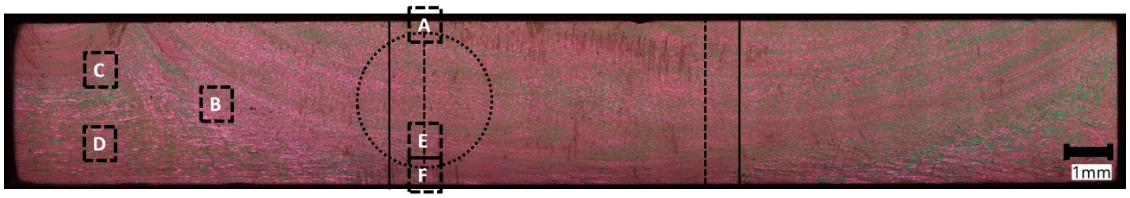

A. Top ¼" Hole Wall	D. TMAZ
B. Repair Bowl	E. Repair Bowl at the ¼" Hole Wall
C. Pin Transition Region	F. Bottom ¼" Hole Wall

Figure 28 Polarized Optical micrograph overlayed with the locations of the site-specific EBSD scans.

Figure 29a shows the region at the top of the coupon, closest to the AFSD tool on the ¼" hole wall. It can be seen there is a misorientation similar to a Mackenziean distribution except for a spike of low-angle grain boundaries. The IPF shows a mostly equiaxed structure with a number average grain size of 8.1 microns and this equiaxed structure is backed up by the KAM showing relatively complete recrystallization.

Figure 29b shows the region of transition from the repair bowl to the TMAZ. The misorientation plot shows a partially recrystallized distribution. The IPF shows elongated grains with a bimodal distribution of grain size with a number average of 4.6 microns. The KAM plot shows a slightly larger amount of subgrain rotation also pointing to a partial recrystallization with less overall strain than xa.

Figure 29c, taken just outside of the region that has undergone a pin interaction shows similar trends in terms of the misorientation distribution to the repair bowl. However, the grain structure appears to be more equiaxed indicating more complete recrystallization, possibly due to the strain induced from a nearby pin interaction. The region has a number average grain size of 4.1 μm.

Figure 29d taken in the non-recrystallized TMAZ shows a striking difference from all other regions. Here the elongated grains from the original rolled microstructure remain. The KAM shows regions of subgrain rotation not expected in a rolled texture. This is due to the heat and pressure of the repair beginning to recrystallize the region.

Figure 29e shows the region where the repair bowl crosses the future ¼" hole wall. This region is critical as it was the material deposited furthest from the tool that would remain after the coupon was cut back to the test geometry. The misorientation distribution is the closest seen yet to Mackenziean, with fairly equiaxed grain with a number average size of 4.7 microns. The KAM plot shows near full recrystallization similar to xa. Without adequate mixing in the repair, there could be "kissing" bonds where the deposited material only touches the base material and is not truly bonded. In processes with less mixing like refill and probeless friction stir spot welding this is the case, with kissing bonds at the bottom of the bowl at similar locations limiting repair depth [73], [74].

Figure 29f shows the region of the future ¼” hole wall furthest from the tool. Here there is a fully Mackenziean distribution with an equiaxed, bimodal grain structure with a number average grain size of 4.1 microns. The KAM plot shows very little evidence of subgrain boundaries. The gradient in grain size from smaller grains in the top of the image to larger grains towards the bottom is likely driven by flowing material that saw a higher shear strain rate on the top and rolled grains that were fully recrystallized at a lower strain rate on the bottom denoted by their larger size.

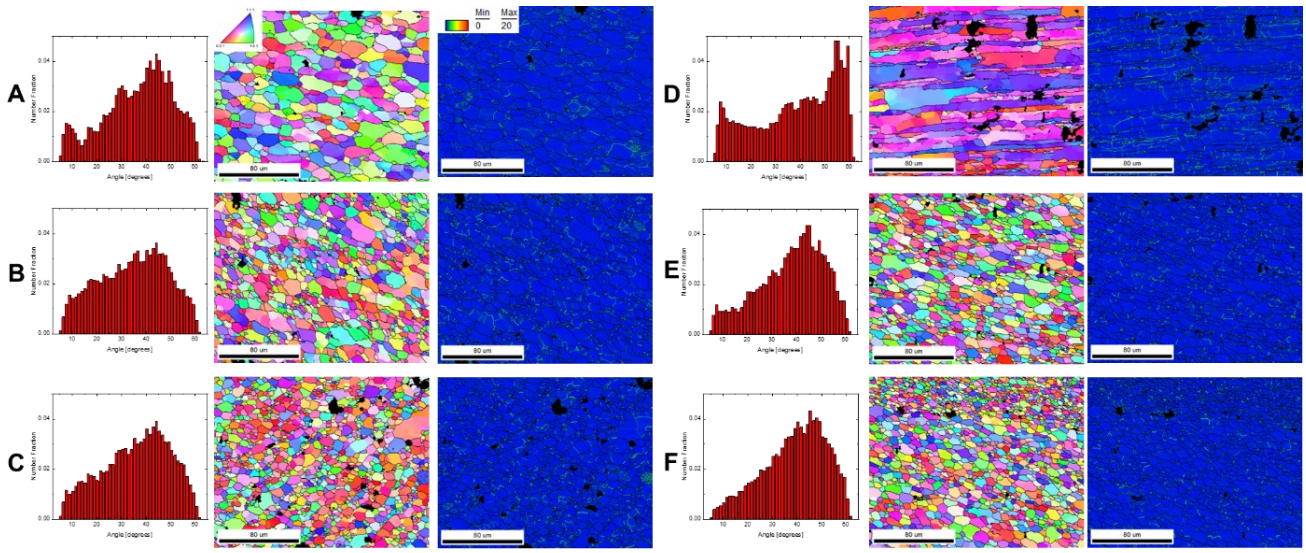

Figure 29 A) Top of 1/4" hole wall misorientation, inverse pole figure (IPF), and kernel average misorientation map (KAM). B) Repair bowl. This region is the transition from the deposit bowl to the TMAZ. C) Pin transition region. This is the region that was directly adjacent to the protrusion. D) Thermo-mechanically affected zone that did not see any direct flow. E) Repair bowl at the 1/4" hole wall. F) Bottom of the 1/4” hole wall. This is the most likely place for kissing bonds to form due to distance from the tool.

In all the samples imaged these regions were very similar. As an analog for all 36 sites, results from the top-hole wall location are shown for each of the other groups in Figure 30a-f corresponding to the Old Shim, Puck, Reverse Shim, No Shim, Full Shim, and Dimple respectively.

Figure 30a taken from the Old Shim is identical to Figure 29a and is shown for convenience. Figure 30b shows the top hole of the Puck configuration with a very similar misorientation plot to the Old Shim. The IPF shows a more equiaxed structure with a number average grain size of 9.1 microns. The KAM plot is nearly identical to Figure 30a showing a large degree of recrystallization.

Figure 30c from the Reverse Shim also shows a similar misorientation plot to the Old Shim. The IPF shows the more elongated grains like xa with a number average size of 7.8 microns. While there is some preferential texture with more [111] characteristic shown here a detailed texture analysis is beyond the scope of this work but has been studied in other works (Gregs 70502 paper) [20]. The KAM plot is very similar to the others in this figure.

Figure 30d shows the No Shim configuration with a very similar misorientation plot. The IPF however looks different with a clear top-to-bottom gradient, slightly elongated grains, and a number average grain size of 6.3 microns. The KAM, however, looks very similar to Figure 30a-c.

Figure 30e from the Full Shim takes on the most Mackenziean distribution of the set. With primarily equiaxed grains and a number average grain size of 6.9 microns, the IPF also shows some preferential orientation like xc. The KAM plot shows slightly more subgrain rotation than Figure 30a-xd.

Figure 30f from the Dimple shows a misorientation distribution similar to all but the full shim with a slightly higher peak of around 15 degrees. The IPF shows very equiaxed grains and none of the preferential orientation shown in C or E. The KAM plot however shows the most misorientation of the set, pointing to more subgrain rotation and recrystallization that was not fully complete for the highest strain rate that the material underwent.

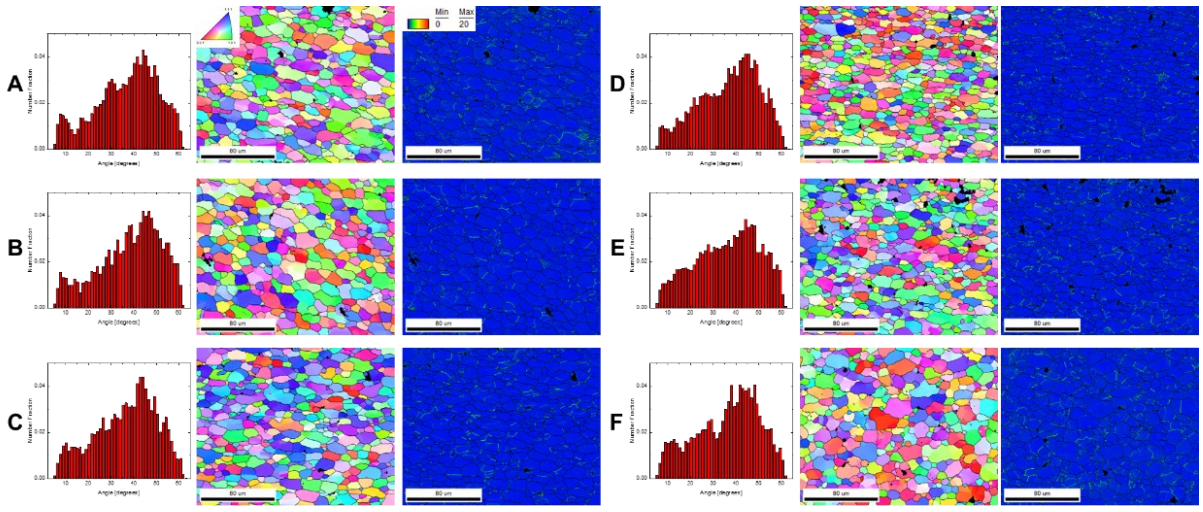

Figure 30 Misorientation plot, IPF, and KAM map of the top of the 1/4" hole wall for A) Old Shim. B) Puck. C) Reverse Shim. D) No Shim. E) Full Shim. F) Dimple

Fracture Surfaces

The fracture surfaces of the samples repaired utilizing active cooling show deviations from the nominal repair. Looking at the overview of the nominal repair in Figure 31a, which is oriented so that the tool contact surface is the top of the image, and a zoomed-in region in A1 the crack propagation mode for the nominal repair was intergranular. This is characterized by the "rock candy" appearance of the surface and is likely driven by the high density of particles on the grain boundary surface [75]. The Old Shim in Figure 31b tells a different story. Looking at its overview in B, which is oriented in the same way as A, there are several distinct regions. Looking on the right-hand side of the image, near the hole wall, the region shown in B1 is shown to have a mixed mode, mainly trans-granular crack propagation mode, evidenced by the "beach mark" patterns with some intergranular evidence. This is repeated in B2 slightly further from the hole wall but much further from the tool. Looking further inward to B3 there is some transgranular fracture but more evidence of intergranular fracture than in B1 or B2. B4 is entirely

intergranular, looking very similar to A1. This means that the crack propagation mode changes during the fatigue test for the actively cooled samples. The presence of the trans-granular fracture mode is likely a large contributor to the longer fatigue life as it is a more energy-intensive fracture mode. This trend of intergranular to transgranular fracture is echoed in the other samples.

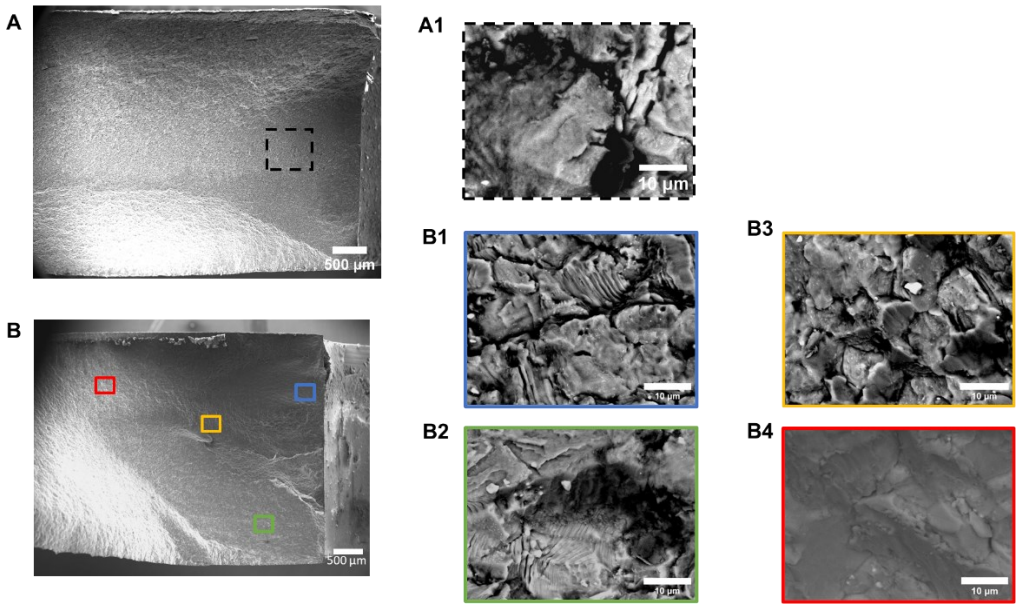

Figure 31 A) Overview SEM image of the nominal repair. A1) Zoomed in backscatter image of the dashed region in A. B) Overview of the middle-performing Old Shim. B1)-B4) Backscatter images of the regions marked in B with color-coded borders. Images get increasingly further from the edge of the hole wall.

TEM

Since the actively cooled groups did not have meaningful flow or fatigue life differences, most of the change in performance from nominal is concluded to be from thermal control adjustments. Once again using the Old Shim as an analog, a 3mm diameter cylinder was cut from the region shown with the dotted line in Figure 28. Below in Figure 32A, a large area HAADF image is shown. Immediately, it is apparent that there is significantly less grain boundary precipitation than the nominal repair along with less overgrown precipitates in the grain interior. Looking closer at the grain boundary in B, there are Zn-rich particles on the order of 5nm running along the grain boundary with particles in the grain interior. Looking at a triple junction grain boundary near this image, there is more evidence of the small Zn-rich particles, along with a copper-rich particle in the triple junction. Looking at the line scan running through the particle, there is a copper and corresponding Mg peak implying that this may be S-phase (Al_2CuMg). Looking closer at one of the particles seen in Figure 32B, these particles are overgrown precipitates forming on zirconium-rich dispersoid particles. This is corroborated by the line scan in F. There is an initial Zr peak followed by a Zn peak. This is likely the $MgZn_2$ precipitate nucleating on an Al_3Zr dispersoid particle. Overall, there is evidence of some grain boundary precipitation and heterogeneous nucleation, but it is lesser than the nominal repair.

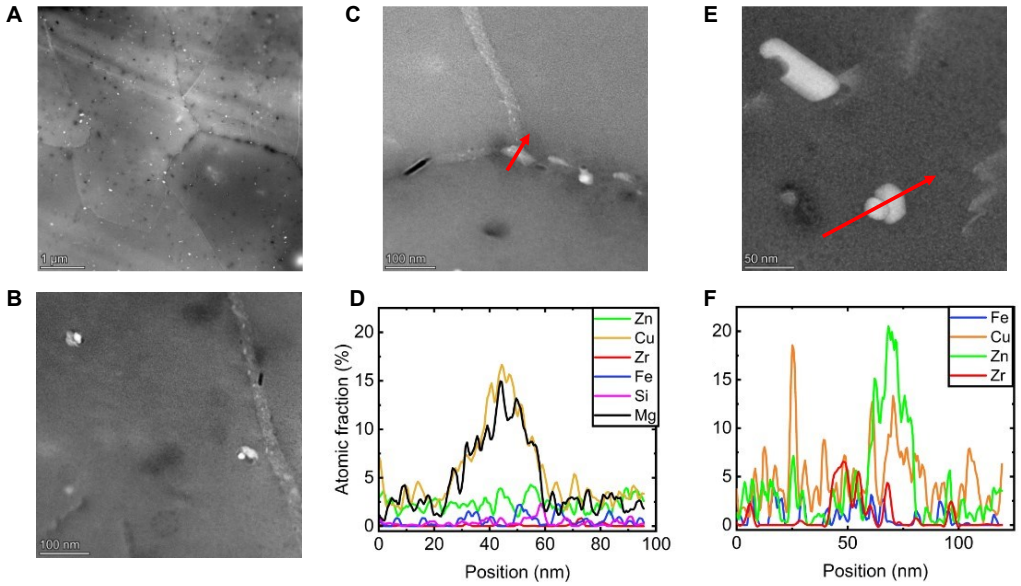

Figure 32 A) Low magnification HAADF B) HAADF of a grain boundary and grain interior. C) HAADF micrograph of a triple junction with small grain boundary precipitates above and a copper-rich particle in the center with EDX line scan noted D) Corresponding line scan is shown in C. E) HAADF of two heterogeneously nucleated precipitates with EDX line scan noted. F) The corresponding line scan is shown in E.

These figures can be compared to the TEM of the nominal repair to understand the difference in precipitate morphology. The actively cooled low magnification image in Figure 32A is contrasted with Figure 33A that shows much larger particles both in the interior of the grain and on the boundary. Figure 32B and Figure 33B both show a grain boundary with the nominal repair having more and larger precipitates. Figure 32E and its corresponding line scan in F reflect the same heterogeneous nucleation as shown in Figure 33C and D. Both particles are $MgZn_2$ located on a Zr-based dispersoid particle.

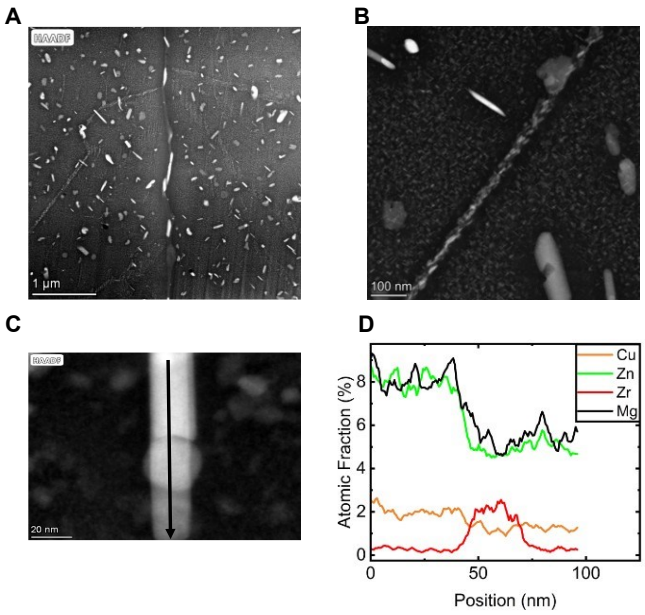

Figure 33 TEM from the nominal repair in Hahn et. al showing: A) Low magnification HAADF micrograph. B) HAADF micrograph showing a grain boundary with precipitation. C) Overgrown precipitate on a Zr particle with EDX line scan noted. D) Results of the scan shown in C.

The shape and distribution of the non-heterogeneously nucleated precipitates are also of interest as they govern the structural properties of the material. Looking closer at the linescan region from Figure 32E in Figure 34A, a heterogeneously nucleated precipitate from the actively cooled sample is shown. The η-phase shown in Figure 34 appears to be approximately twice the size as the 15-20nm dispersoid particle. In contrast, a similar particle from the nominal repair is shown in Figure 34B, in this work a linescan confirmed this to be heterogeneously precipitated η on a Zr dispersoid particle. This particle is an order of magnitude larger than the 15-20 nm dispersoid particle and is surrounded by a PFZ approximately 15 nm across. Outside of the PFZ in the nominal case, the precipitates appear to be much larger than the single nanometer size shown in the actively cooled case. These smaller precipitates are most likely η', compared to the larger fully formed η-phase within the nominal case.

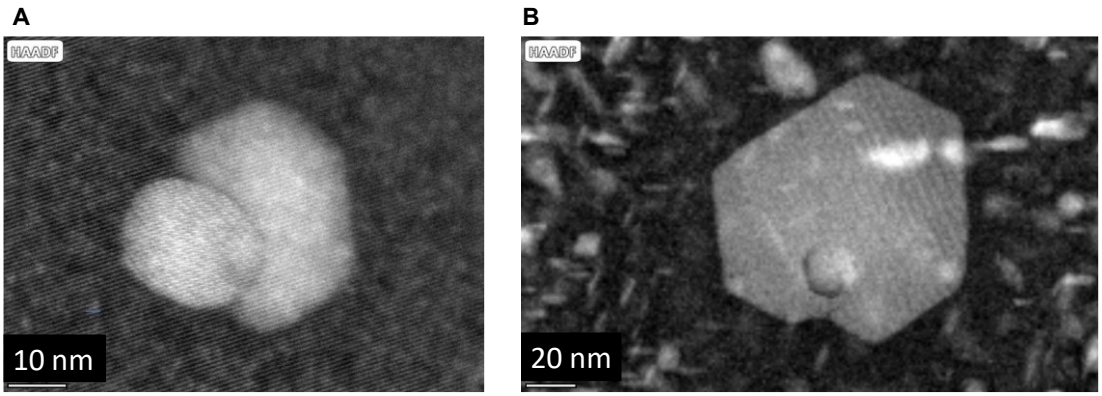

Figure 34 Heterogeneously nucleated precipitates in the A) Actively cooled sample. B) In the Nominal repair. Note the scale difference between the two images.

Discussions

Based on the fatigue results, the geometry of the backing plate had little effect on the fatigue performance. This is corroborated by the little difference between groups in polarized optical microscopy and EBSD. Overall, the characterization, except for some inconclusive fracture surfaces, shows a remarkable resemblance to the nominal repair. This similarity implies that the overall high shear processing and material mixing is very similar to nominal repair and the geometry did not fundamentally change the processing.

On the other hand, the active cooling combined with a lower maximum temperature did play a large role in extending the lifetime of the specimens. This is further confirmed by splitting the fatigue life into two parts. A pre-crack lifetime and a post-crack lifetime. The delineation between the two, i.e. the number of cycles to crack initiation, is calculated by fitting a RANSAC linear fit to the steady state peak displacement vs time graph. The crack initiation point is declared where the frame displacement deviates by more than 0.002mm away from the fit. This deviation is due to a loss of stiffness in the coupon due to the crack initiation.

Looking at a breakdown of this improvement for all samples in Figure 35 shows a clear difference between the samples in this work and the nominal repair. It has been shown by Hahn et. al. that the nominal repair does well compared to the baseline in the number of cycles to crack initiation by breaking up the large constituent particles that serve as stress concentrators on the hole wall. However, significant precipitate-free zones (PFZs) caused by heterogenous nucleation weaken the repaired material leading to a fast crack growth phase and a low number of cycles after initiation compared to baseline. The high temperatures and large degree of mixing combined with a small volume of material lead to the deposited material existing in a solutionized state directly following the end of the stir. These PFZs and heterogenous nucleation are caused by the slow natural cooling rate from the high temperature of the deposition. In this work, the actively cooled samples underwent a faster cooling rate from a lower initial temperature therefore leading to smaller PFZs and heterogeneously nucleated particles. Due to this cooling rate, the actively cooled repairs in this work perform better in both cycles to crack

initiation as well as the number of cycles after crack initiation. This means that they take longer to start cracking than the nominal repair and when they do crack, the propagation life is longer, further sustaining the life of the repair. In contrast, once the nominal repair showed a crack initiation it reached ultimate failure very quickly afterwards. It should also be noted that these actively cooled groups performed very similarly to one another once again.

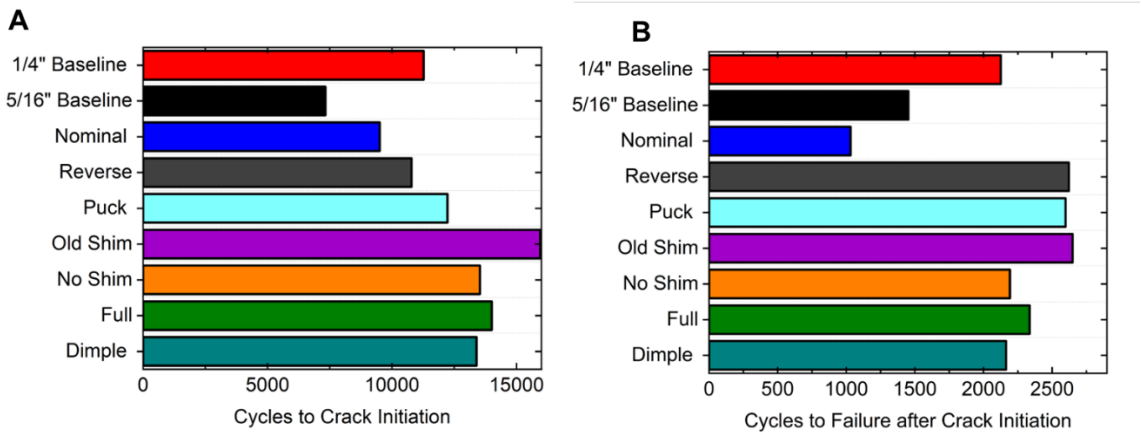

Figure 35 A) Number of cycles to crack initiation for the nominal repair, pristine baselines, and the groups shown in this work. B) Number of cycles to failure after crack initiation for the same groups.

The increase of the 60% fatigue life of the repaired coupon, now outperforming the pristine rolled plate sample is due to a few changes caused by AFSD. First, the high shear of the process breaks apart the large iron-rich constituent particles present in the rolled base material. These particles provide potent crack initiation sites for both the ¼" and 5/16" baseline conditions. By eliminating these sites, cracks must initiate instead on overgrown precipitates, which act as smaller stress concentrations than the large constituent particles. In the nominal repair case, the upside stops there. In the nominal case, slow cooling rates from the solutionized state promote the formation of large PFZs and heterogenous nucleation on dispersoids and grain boundaries. This poor precipitate morphology weakens the material and readily allows cracks to propagate along grain boundaries resulting in the intergranular fracture mode seen in SEM.

For the actively cooled condition, the repair reaps the same benefit as the nominal case, except that faster cooling rates at the end of the process better approximate a traditional quench process thus improving the size and distribution of precipitates. Since there is less time at a thermally active, non-solutionizing temperature, less diffusion can occur leading to less heterogenous nucleation. This creates even smaller crack initiation sites leading to the increase in pre-crack lifetime seen in Figure 35a. Additionally, less grain boundary precipitation results in crack propagation paths where the fracture occurs through grains rather than through a precipitate-rich grain boundary. This more energy-intensive mode of fracture also increases the number of cycles.

From the TEM image in Figure 34A, it appears that the faster cooling rate from the actively cooled samples kept enough solute in the solution to have a precipitate structure that is not fully

evolved. In the nominal repair, the slow cooling rate and subsequent natural aging allowed for nearly all the solute to be transformed into η. However much of the solute in the actively cooled sample appears to be in η′. This means that active cooling was sufficient to behave like a quenching step, and a subsequent thermal treatment step could be done to the repaired material to force into a state more similar to a T7x temper. This possibly opens many avenues of exploration and could be a remedy for the loss of other mechanical properties besides fatigue, for example, corrosion and bearing strength.

Conclusions

Repair of AA7050 through holes has been shown to be possible with fatigue results that are better than new material in the R=-1 loading condition. This is a 51% lifetime improvement from the previous work of Hahn et. al. that already beat new material in the R=0.1 loading condition. The improvement of the fatigue life is possible through the high shear process of AFSD breaking down the hole wall and promoting good bonding and mixing while simultaneously breaking up large second-phase particles that promote crack initiation. Constituent particle breakup has already been shown by Hahn et. al. Using new active cooling after the repair has ended, it is possible to gain even more benefit to the fatigue life. This is not to say that AFSD produces material that is more resistant to fatigue than rolled plate. If it were possible to remove the constituent particles in the plate, perhaps by using a higher purity alloy like AA7450, the results would likely be different.

In essence, AFSD repair of through holes provides several things:

1. A structural repair in which corroded holes can be returned to their specified size with an improvement in fatigue life compared to the base material.
2. Shear-assisted breakup and dispersion of Fe-rich constituent particles that serve as crack initiation sites in the base material.
3. Via active cooling, stronger more homogeneous material can be produced that resists crack initiation and growth as or better than rolled AA7050-T7451 plate.
4. Via active cooling AFSD can deposit repaired material in a solutionized state in which subsequent thermal treatments may be able to further optimize the fatigue and static properties.

The potential drawbacks of this style of repair are caused by the heat input. The massive heat input of this process, if left uncontrolled, will create a large heat-affected zone that could interfere with the overaged temper of the base material. Without a fully realized process model coupled with a global heat transfer model, it will not be possible to know the exact size of the HAZ without extensive trial and error on a per-component basis.

With these pitfalls in mind, however, solutions are apparent. Leveraging a combined process-heat transfer model will allow for the design of external active cooling on the component to minimize the HAZ. While this would need to be on a component-by-components basis this is no different than many other repair methods.

From these experiments, two potential avenues of improvement of the process can be seen. First, maintain the shear of the process to break up constituent particles and make a metallurgical bond. Second, shorten thermal exposure by reducing the length of the repair process and lowering the heat energy input while still solutionizing the precipitates. Third, bring the whole workpiece back down to ambient temperature as fast as possible. With these ideas and constraints in mind, a non-heat-treated solid-state repair may be feasible on aircraft.

Manuscript 3 References

[1] F. P. Incropera and D. P. De Witt, “Fundamentals of heat and mass transfer, 2nd edition,” 1990. [Online]. Available: https://api.semanticscholar.org/CorpusID:94205714

[2] A. V. Lykov, *Analytical Heat Diffusion Theory*. Academic Press, 1968.

[3] R. Komanduri and Z. B. Hou, “Analysis of heat partition and temperature distribution in sliding systems,” *Wear*, vol. 251, no. 1–12, pp. 925–938, Oct. 2001, doi: 10.1016/S0043-1648(01)00707-4.

[4] “Inverse Heat Transfer: Fundamentals and Applications - Helcio R.B. Orlande - Google Books.” Accessed: Feb. 11, 2024. [Online]. Available: https://books.google.com/books?hl=en&lr=&id=xEMiEAAAQBAJ&oi=fnd&pg=PP1&ots=WDtHUe5bnd&sig=IfUktFDZnxIJf9XeOKco5BHMK8c#v=onepage&q&f=false

[5] J. V. Beck, B. Litkouhi, and C. R. S. Clair, “EFFICIENT SEQUENTIAL SOLUTION OF THE NONLINEAR INVERSE HEAT CONDUCTION PROBLEM,” *Numeri Heat Transf A Appl*, vol. 5, no. 3, pp. 275–286, 1982, doi: 10.1080/10407788208913448.

[6] N. Daouas and M. S. Radhouani, “A new approach of the Kalman filter using future temperature measurements for nonlinear inverse heat conduction problems,” *Numerical Heat Transfer, Part B: Fundamentals*, vol. 45, no. 6, pp. 565–585, Jun. 2004, doi: 10.1080/10407790490430598.

[7] J. V Beck, B. Blackwell, and C. R. S. C. Jr, *Inverse Heat Conduction: Ill-Posed Problems*, 1st edition. New York: Wiley-Interscience, 1985.

[8] H. Najafi and K. A. Woodbury, “Online heat flux estimation using artificial neural network as a digital filter approach,” *Int J Heat Mass Transf*, vol. 91, pp. 808–817, Dec. 2015, doi: 10.1016/J.IJHEATMASSTRANSFER.2015.08.010.

[9] S. Wan, P. Xu, K. Wang, J. Yang, and S. Li, “Real-time estimation of thermal boundary of unsteady heat conduction system using PID algorithm,” *International Journal of Thermal Sciences*, vol. 153, p. 106395, Jul. 2020, doi: 10.1016/J.IJTHERMALSCI.2020.106395.

[10] M. Zálešák, L. Klimeš, P. Charvát, M. Cabalka, J. Kůdela, and T. Mauder, “Solution approaches to inverse heat transfer problems with and without phase changes: A state-of-the-art review,” *Energy*, vol. 278, p. 127974, Sep. 2023, doi: 10.1016/J.ENERGY.2023.127974.

[11] H. Z. Yu, “Additive Friction Stir Deposition,” *Additive Friction Stir Deposition*, pp. 1–333, Jan. 2022, doi: 10.1016/C2020-0-01505-7.

[12] J. K. Yoder, H. Z. Yu, W. T. Reynolds, W. Cai, L. Li, and V. Blacksburg, “Origins of Embrittlement of an Al-Zn-Mg-Cu Alloy Post Additive Friction Stir Deposition,” Jan. 2023, Accessed: Sep. 15, 2023. [Online]. Available: https://vtechworks.lib.vt.edu/handle/10919/113012

[13] W. D. Hartley *et al.*, “Solid-state cladding on thin automotive sheet metals enabled by additive friction stir deposition,” *J Mater Process Technol*, vol. 291, 2021, doi: 10.1016/j.jmatprotec.2021.117045.

[14] J. K. Yoder, D. J. Erb, R. Henderson, and H. Z. Yu, “Closed-loop temperature controlled solid-state additive manufacturing of Ti-6Al-4V with forging standard out-of-plane tensile properties,” *J Mater Process Technol*, vol. 322, p. 118201, Dec. 2023, doi: 10.1016/J.JMATPROTEC.2023.118201.

[15] D. Z. Avery *et al.*, “Influence of Grain Refinement and Microstructure on Fatigue Behavior for Solid-State Additively Manufactured Al-Zn-Mg-Cu Alloy,” *Metall Mater Trans A Phys Metall Mater Sci*, vol. 51, no. 6, 2020, doi: 10.1007/s11661-020-05746-9.

[16] G. G. Stubblefield, K. Fraser, B. J. Phillips, J. B. Jordon, and P. G. Allison, “A meshfree computational framework for the numerical simulation of the solid-state additive manufacturing process, additive friction stir-deposition (AFS-D),” *Mater Des*, vol. 202, 2021, doi: 10.1016/j.matdes.2021.109514.

[17] B. J. Phillips *et al.*, “Microstructure-deformation relationship of additive friction stir-deposition Al–Mg–Si,” *Materialia (Oxf)*, vol. 7, p. 100387, Sep. 2019, doi: 10.1016/J.MTLA.2019.100387.

[18] K. C. Kincaid, D. W. MacPhee, G. G. Stubblefield, J. B. Jordon, T. W. Rushing, and P. G. Allison, “A Finite Volume Framework for the Simulation of Additive Friction Stir Deposition,” *J Eng Mater Technol*, vol. 145, no. 3, Jul. 2023, doi: 10.1115/1.4056642.

[19] N. Gotawala and H. Z. Yu, “Material flow path and extreme thermomechanical processing history during additive friction stir deposition,” *J Manuf Process*, vol. 101, pp. 114–127, Sep. 2023, doi: 10.1016/J.JMAPRO.2023.05.095.

[20] P. C. Metz *et al.*, “Heterogeneous microstructure development in additive friction-stir deposited Al-Mg-Si alloy,” 2024, doi: 10.1016/j.addma.2024.103989.

[21] B. A. Rutherford *et al.*, “metals Effect of Thermomechanical Processing on Fatigue Behavior in Solid-State Additive Manufacturing of Al-Mg-Si Alloy”, doi: 10.3390/met10070947.

[22] G. D. Hahn, K. P. Knight, N. Gotawala, and H. Z. Yu, “Additive friction stir deposition of AA7050 achieving forging-like tensile properties,” *Materials Science and Engineering: A*, vol. 896, p. 146268, Mar. 2024, doi: 10.1016/J.MSEA.2024.146268.

[23] M. B. Williams *et al.*, “Towards Understanding the Relationships between Processing Conditions and Mechanical Performance of the Additive Friction Stir Deposition Process,” *Metals 2023, Vol. 13, Page 1663*, vol. 13, no. 10, p. 1663, Sep. 2023, doi: 10.3390/MET13101663.

[24] G. R. Merritt, M. B. Williams, P. G. Allison, J. B. Jordon, T. W. Rushing, and C. A. Cousin, “Closed-Loop Temperature and Force Control of Additive Friction Stir

Deposition," *Journal of Manufacturing and Materials Processing*, vol. 6, no. 5, 2022, doi: 10.3390/jmmp6050092.

[25] R. Sanders and J. Staley, "A History of Wrought Aluminum Alloys and Applications," in *Properties and Selection of Aluminum Alloys*, ASM International, 2019, pp. 157–201. doi: 10.31399/asm.hb.v02b.a0006516.

[26] Battelle Memorial Institute., "Metallic Materials Properties Development and Standardization (MMPDS-2023)".

[27] E. A. Starke and J. T. Staley, "Application of modern aluminium alloys to aircraft," in *Fundamentals of Aluminium Metallurgy: Production, Processing and Applications*, Elsevier Ltd., 2010, pp. 747–783. doi: 10.1533/9780857090256.3.747.

[28] H. Z. Yu *et al.*, "Non-beam-based metal additive manufacturing enabled by additive friction stir deposition," *Scr Mater*, vol. 153, pp. 122–130, Aug. 2018, doi: 10.1016/j.scriptamat.2018.03.025.

[29] H. Z. Yu and R. S. Mishra, "Additive friction stir deposition: a deformation processing route to metal additive manufacturing," *Mater Res Lett*, vol. 9, no. 2, 2021, doi: 10.1080/21663831.2020.1847211.

[30] J. K. Yoder, R. J. Griffiths, and H. Z. Yu, "Deformation-based additive manufacturing of 7075 aluminum with wrought-like mechanical properties," *Mater Des*, vol. 198, Jan. 2021, doi: 10.1016/j.matdes.2020.109288.

[31] A. M. Vest, D. R. St-Pierre, S. Rock, A. M. Maniatty, D. J. Lewis, and S. J. A. Hocker, "Thermocouple Temperature Measurements in Selective Laser Melting Additive Manufacturing", Accessed: Feb. 11, 2024. [Online]. Available: http://www.sti.nasa.gov

[32] B. Müller, ; U Renz, B. Mü Ller, and U. Renz, "Development of a fast fiber-optic two-color pyrometer for the temperature measurement of surfaces with varying emissivities," *Review of Scientific Instruments*, vol. 72, no. 8, pp. 3366–3374, Aug. 2001, doi: 10.1063/1.1384448.

[33] A. Lerner *et al.*, "Laser Powder Bed Fusion thermal monitoring using optical fiber sensors: in situ measurements and modelling," *2023 Conference on Lasers and Electro-Optics Europe and European Quantum Electronics Conference, CLEO/Europe-EQEC 2023*, 2023, doi: 10.1109/CLEO/EUROPE-EQEC57999.2023.10232209.

[34] C. Krishna, P. Vallabh, and X. Zhao, "Melt pool temperature measurement and monitoring during laser powder bed fusion based additive manufacturing via single-camera two-wavelength imaging pyrometry (STWIP)," *J Manuf Process*, vol. 79, pp. 486–500, 2022, doi: 10.1016/j.jmapro.2022.04.058.

[35] B. Bevans *et al.*, "Heterogeneous sensor data fusion for multiscale, shape agnostic flaw detection in laser powder bed fusion additive manufacturing," *Virtual Phys Prototyp*, vol. 18, no. 1, Dec. 2023, doi: 10.1080/17452759.2023.2196266.

[36] J. Petrich, Z. Snow, D. Corbin, and E. W. Reutzel, “Multi-modal sensor fusion with machine learning for data-driven process monitoring for additive manufacturing,” *Addit Manuf*, vol. 48, p. 102364, Dec. 2021, doi: 10.1016/J.ADDMA.2021.102364.

[37] P. K. Rao, J. Liu, D. Roberson, Z. Kong, and C. Williams, “Online Real-Time Quality Monitoring in Additive Manufacturing Processes Using Heterogeneous Sensors,” *Journal of Manufacturing Science and Engineering, Transactions of the ASME*, vol. 137, no. 6, Dec. 2015, doi: 10.1115/1.4029823/374977.

[38] K. J. Colligan and R. S. Mishra, “A conceptual model for the process variables related to heat generation in friction stir welding of aluminum,” *Scr Mater*, vol. 58, no. 5, pp. 327–331, Mar. 2008, doi: 10.1016/j.scriptamat.2007.10.015.

[39] W. D. Hartley and S. W. Case, “Processing Mechanics of Additive Friction Stir Deposition.”

[40] S. H. Mousavi Anijdan, H. R. Madaah-Hosseini, and A. Bahrami, “Flow stress optimization for 304 stainless steel under cold and warm compression by artificial neural network and genetic algorithm,” *Mater Des*, vol. 28, no. 2, pp. 609–615, Jan. 2007, doi: 10.1016/J.MATDES.2005.07.018.

[41] K. A. Fraser, “Robust and efficient meshfree solid thermo-mechanics simulation of friction stir welding,” 2017.

[42] K. Kumar, C. Kalyan, S. V. Kailas, and T. S. Srivatsan, “An Investigation of Friction During Friction Stir Welding of Metallic Materials,” *Materials and Manufacturing Processes*, vol. 24, no. 4, pp. 438–445, Apr. 2009, doi: 10.1080/10426910802714340.

[43] A. F. Hasan, C. J. Bennett, P. H. Shipway, S. Cater, and J. Martin, “A numerical methodology for predicting tool wear in Friction Stir Welding,” *J Mater Process Technol*, vol. 241, pp. 129–140, Mar. 2017, doi: 10.1016/J.JMATPROTEC.2016.11.009.

[44] S. Mandal, J. Rice, G. Hou, K. M. Williamson, and A. A. Elmustafa, “Modeling and simulation of a donor material concept to reduce tool wear in friction stir welding of high-strength materials,” *J Mater Eng Perform*, vol. 22, no. 6, pp. 1558–1564, Jun. 2013, doi: 10.1007/S11665-012-0452-4/FIGURES/10.

[45] J. Zhang, P. Upadhyay, Y. Hovanski, and D. P. Field, “High-Speed Friction Stir Welding of AA7075-T6 Sheet: Microstructure, Mechanical Properties, Micro-texture, and Thermal History”, doi: 10.1007/s11661-017-4411-4.

[46] G. R. Merritt, M. B. Williams, P. G. Allison, J. B. Jordon, T. W. Rushing, and C. A. Cousin, “Closed-Loop Temperature and Force Control of Additive Friction Stir Deposition,” *Journal of Manufacturing and Materials Processing*, vol. 6, no. 5, Oct. 2022, doi: 10.3390/jmmp6050092.

[47] Z. T. Niu, H. Qi, Y. K. Ji, S. Wen, Y. T. Ren, and M. J. He, “Real-time reconstruction of thermal boundary condition of porous media via temperature sequence,” *International Journal of Thermal Sciences*, vol. 177, Jul. 2022, doi: 10.1016/j.ijthermalsci.2022.107570.

[48] D. Lu and C. Wang, “Three-dimensional temperature field inversion calculation based on an artificial intelligence algorithm,” *Appl Therm Eng*, vol. 225, May 2023, doi: 10.1016/j.applthermaleng.2023.120237.

[49] S. Motahar, “Experimental study and ANN-based prediction of melting heat transfer in a uniform heat flux PCM enclosure,” 2020, doi: 10.1016/j.est.2020.101535.

[50] C. Fieberg and R. Kneer, “Determination of thermal contact resistance from transient temperature measurements,” *Int J Heat Mass Transf*, vol. 51, no. 5–6, pp. 1017–1023, Mar. 2008, doi: 10.1016/j.ijheatmasstransfer.2007.05.004.

[51] A. Bejan and A. D. Kraus, *Heat transfer handbook*. J. Wiley, 2003.

[52] M. Nouari, B. Haddag, A. Moufki, and S. Atlati, “Investigation on the built-up edge process when dry machining aeronautical aluminum alloys,” *Machining of Light Alloys*, pp. 35–48, Aug. 2018, doi: 10.1201/B22153-2.

[53] R. Nandan, T. Debroy, and H. K. D. H. Bhadeshia, “Recent advances in friction-stir welding-Process, weldment structure and properties”, doi: 10.1016/j.pmatsci.2008.05.001.

[54] R. Nandan, G. G. Roy, T. J. Lienert, and T. Debroy, “Three-dimensional heat and material flow during friction stir welding of mild steel,” *Acta Mater*, vol. 55, no. 3, pp. 883–895, Feb. 2007, doi: 10.1016/J.ACTAMAT.2006.09.009.

[55] K. Fraser, L. I. Kiss, L. St-Georges, and D. Drolet, “Optimization of friction stir weld joint quality using a meshfree fully-coupled thermo-mechanics approach,” *Metals (Basel)*, vol. 8, no. 2, Feb. 2018, doi: 10.3390/MET8020101.

[56] S. Solhjoo, “Revisiting the Common Practice of Sellars and Tegart’s Hyperbolic Sine Constitutive Model,” *Modelling 2022, Vol. 3, Pages 359-373*, vol. 3, no. 3, pp. 359–373, Aug. 2022, doi: 10.3390/MODELLING3030023.

[57] G. G. Stubblefield *et al.*, “Ballistic Evaluation of Aluminum Alloy (AA) 7075 Plate Repaired by Additive Friction Stir Deposition Using AA7075 Feedstock,” *Journal of Dynamic Behavior of Materials*, vol. 9, no. 1, pp. 79–89, Mar. 2023, doi: 10.1007/s40870-022-00363-6.

[58] C. J. T. Mason *et al.*, “Process-structure-property relations for as-deposited solid-state additively manufactured high-strength aluminum alloy,” *Addit Manuf*, vol. 40, Apr. 2021, doi: 10.1016/j.addma.2021.101879.

[59] R. S. Mishra, R. S. Haridas, and P. Agrawal, “Friction stir-based additive manufacturing,” *Science and Technology of Welding and Joining*, vol. 27, no. 3. Taylor and Francis Ltd., pp. 141–165, 2022. doi: 10.1080/13621718.2022.2027663.

[60] R. S. Mishra and M. Komarasamy, *Physical Metallurgy of 7XXX Alloys*. Elsevier, 2016. doi: 10.1016/b978-0-12-809465-5.00002-7.

[61] M. Schöbel, P. Pongratz, and H. P. Degischer, "Coherency loss of Al 3(Sc,Zr) precipitates by deformation of an Al-Zn-Mg alloy," *Acta Mater*, vol. 60, no. 10, pp. 4247–4254, Jun. 2012, doi: 10.1016/j.actamat.2012.04.011.

[62] A. Zubelewicz, "Century-long Taylor-Quinney interpretation of plasticity-induced heating reexamined," *Scientific Reports 2019 9:1*, vol. 9, no. 1, pp. 1–7, Jun. 2019, doi: 10.1038/s41598-019-45533-0.

[63] V. L. Popov, "Thermal Effects in Contacts," *Contact Mechanics and Friction*, pp. 199–205, 2010, doi: 10.1007/978-3-642-10803-7_13.

[64] B. H., "Theoretical Study of Temperature Rise at Surfaces of Actual Contact under Oiliness Lubricating Conditions," *Proc. Instn. Mech. Engrs. (General discussion on lubrication and lubricants)*, vol. 2, pp. 222-, 1937, Accessed: Mar. 11, 2024. [Online]. Available: https://cir.nii.ac.jp/crid/1573668924965107328

[65] J. C. Jaeger and J. C. Jaeger, "Moving sources of heat and the temperature at sliding contacts," *Journal and proceedings of the Royal Society of New South Wales*, vol. 76, no. 3, pp. 203--224, May 1943, doi: 10.5962/p.360338.

[66] K. J. Zwick and M. Tate, "Flash Temperature Theory," *Encyclopedia of Tribology*, pp. 1182–1194, 2013, doi: 10.1007/978-0-387-92897-5_1312.

[67] D. G. Bansal and J. L. Streator, "A method for obtaining the temperature distribution at the interface of sliding bodies," *Wear*, vol. 266, no. 7–8, 2009, doi: 10.1016/j.wear.2008.08.019.

[68] M. Akbari, D. Sinton, and M. Bahrami, "Moving heat sources in a half space: Effect of source geometry," *Proceedings of the ASME Summer Heat Transfer Conference 2009, HT2009*, vol. 3, pp. 685–694, 2009, doi: 10.1115/HT2009-88562.

[69] R. Mendoza, "In-service Corrosion Issues in Sustainment of Naval Aircraft," 2012.

[70] R. Joey Griffiths, D. T. Petersen, D. Garcia, and H. Z. Yu, "Additive friction stir-enabled solid-state additive manufacturing for the repair of 7075 aluminum alloy," *Applied Sciences (Switzerland)*, vol. 9, no. 17, Sep. 2019, doi: 10.3390/app9173486.

[71] M. E. J. Perry, R. J. Griffiths, D. Garcia, J. M. Sietins, Y. Zhu, and H. Z. Yu, "Morphological and microstructural investigation of the non-planar interface formed in solid-state metal additive manufacturing by additive friction stir deposition," *Addit Manuf*, vol. 35, Oct. 2020, doi: 10.1016/j.addma.2020.101293.

[72] M. E. J. Perry *et al.*, "Tracing plastic deformation path and concurrent grain refinement during additive friction stir deposition," *Materialia (Oxf)*, vol. 18, Aug. 2021, doi: 10.1016/j.mtla.2021.101159.

[73] C. C. De Castro *et al.*, “Tool wear mechanisms and effects on refill friction stir spot welding of AA2198-T8 sheets,” *Journal of Materials Research and Technology*, vol. 20, pp. 857–866, Sep. 2022, doi: 10.1016/J.JMRT.2022.07.092.

[74] Q. Chu *et al.*, “On visualizing material flow and precipitate evolution during probeless friction stir spot welding of an Al-Li alloy,” *Mater Charact*, vol. 144, pp. 336–344, Oct. 2018, doi: 10.1016/J.MATCHAR.2018.07.026.

[75] “Wrought Aluminum Alloys: Atlas of Fractographs,” in *Fractography*, ASM International, 2018, pp. 414–439. doi: 10.31399/asm.hb.v12.a0000621.

Appendix 1

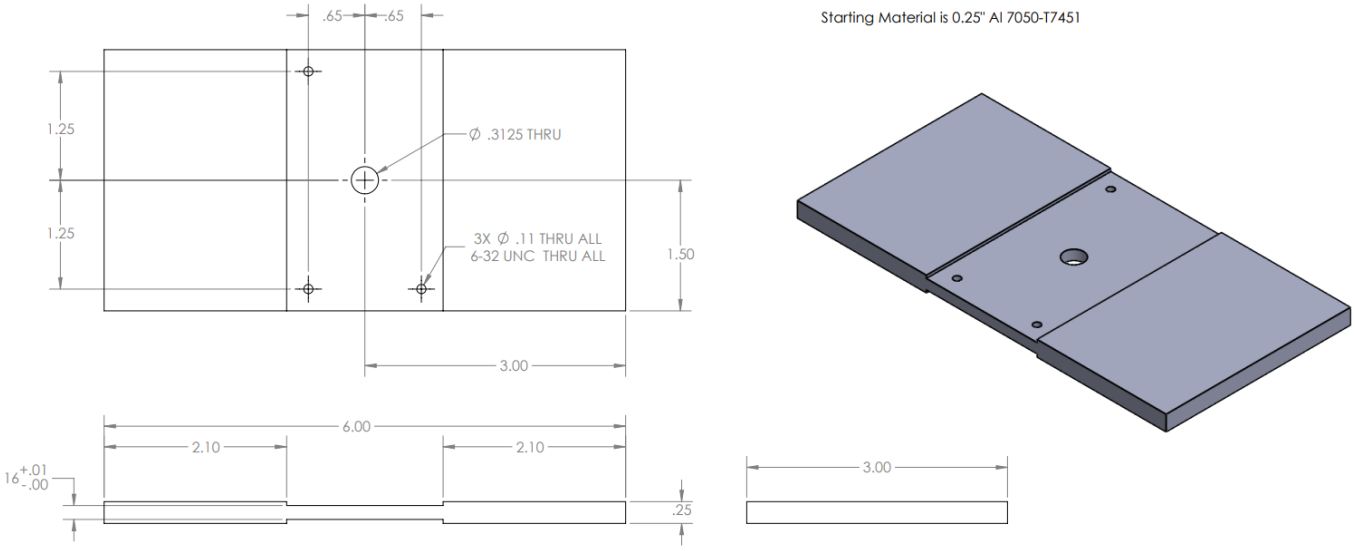
.65
.65
1.25
1.25
Ø .3125 THRU
3X Ø .11 THRU ALL
6-32 UNC THRU ALL
1.50
3.00
6.00
2.10
2.10
16 +.01 -.00
.25
Starting Material is 0.25" Al 7050-T7451
3.00

5 Chapter 5: Conclusions and Future Work

5.1 Temperature Measurement

Chapter two presents a characterization of the heat generation and distribution in a stationary AFSD print. It is shown that the proportion of energy that goes either into the tool or the substrate is dependent on both the tool type and the temperature field. This means that measuring the temperature at a point along the tool and claiming that measurement is simply some number of degrees different than the stir is false. The complexity of the relationship between a tool temperature measurement and the stir temperature has meaning for quality control claims. Any QC claim that implies two different geometries should have the same material properties because they were processed with the same sensor temperature is false. At best, a constant sensor temperature between two prints of the same geometry means that there was probably no variation between runs, however, this is not a guarantee. Changes in the thermal conditions (e.g. convection, substrate mounting) will skew a sensor's temperature reading and if a control loop is driven from this temperature, it may be able to compensate. In other words, a theoretical print could be achieved at a given rotation rate and temperature combination but a change in the convection either on the tool, in the cooling jacket, or on the substrate could mean that the second build is printed at the same temperature but at a different rotation rate since the controller will adapt to try to maintain the same measured value.

A possible way to overcome this was presented in Chapter Two as well. Using the temperature profile along a tool it is possible to calculate the heat flux going into it at each moment in time when the temperature is sampled. Based on this heat flux and the calculated contact heat transfer coefficient, the driving force for the calculated heat flux can be estimated. In essence, this driving force for heat flux is the average temperature of the stir. This method compensates for anything that may change the proportion of heat flux going into the tool since the tool's resistance to heat flow is a constant value. Based on the work in Chapter Three this heat flux-informed temperature calculation may only be applicable when the tool is relatively thermally diffusive such as a single-piece tool, or the heat generation is primarily from plastic deformation rather than tool to stir friction. If too much heat is generated on the boundary, the assumptions about the contact heat transfer conditions fall apart since a sliding contact has a zero-jump temperature condition. A more diffusive tool allows for the heat generated on the boundary to spread out faster, allowing for a better calculation of the driving temperature.

5.2 Tool Considerations

Much of Chapter Three is dedicated to a discussion of the effects of tool construction. The manufacturing tolerances of the tool along with surface preparation and thermocouple mounting can cause discrepancies between two nominally identical tools. The current generation of three-piece tools has pros and cons associated with it. On one hand, the three-piece design creates a conductive break, reducing the amount of power going into the tool that must be carried out by the water jacket. Reducing the heat into the tool also reduces problems associated with the thermal softening of the incoming feedrod leading to jamming. Since the separate face component serves to stop the transmission of thermal energy, it is much hotter than the corresponding region in a single-piece tool. It is believed that the increased temperature relative to the single-piece tool leads to a change in the portion of the heat that is generated by friction

versus plastic deformation due to a change in the stick-slip coefficient. With the introduction of pins on the face to force more plastic deformation, more of the total heat is generated inside of the stir rather than on the boundary. This change in the location and transmission of heat leads to the difference between the measured embedded thermocouple and the effective stir temperature gaining more uncertainty. In other words, the difference in temperature between an embedded thermocouple and the stir is no longer just a function of the amount of heat flux into the tool, it is also a function of the dominant heat generation mechanism. This uncertainty is compounded by any manufacturing discrepancies which will lead to differences in the embedded thermocouple measurement due to internal contact differences.

5.3 Heat Generation

The heat generation in the AFSD process is a complex phenomenon related to the geometry and processing conditions for a given print. The best approximation without an active power control scheme is simply considering a fixed percentage of the spindle's output mechanical power. In general, this power trends with a higher volumetric flow rate leading to a higher power. The ratio of mechanical power to thermal power was investigated in Chapters two and three and it was experimentally confirmed to be a relatively fixed fraction. However, at any given time this power could increase or decrease depending on geometric effects as shown in Chapter Three. When approaching an edge at a sufficiently low Peclet number, the heat has time to propagate forward. When this heat has nowhere to go, such as at a wall, this will lead to a decrease in input power due to the corresponding temperature rise softening the material. At the same time, this wall will force more heat into the tool as the more favorable conduction path leading to both a true and perceived rise in temperature. In more complex prints, this ratio change can have a considerable effect. Consider the case of temperature control, such as that implemented on the L3 Meld Machine from MELD Manufacturing. The rotation rate is driven by a PID controller to raise or lower the temperature read by an embedded thermocouple. If, for example, a tall thin geometry is to be built over several hours in an open-air chamber. As this print progresses it acts more like a heat exchanger fin. More area for convection is added and a faster natural convection condition is created. The increased convection will make the substrate increasingly diffusive relative to the start of the build reducing the fraction of the heat going into the tool. The tool thermocouple will begin to read a lower value based on a smaller fraction of the heat flux and the controller will interpret that as a decreasing temperature; correspondingly increasing the spindle rotation rate. In this way, a build that has nominally the same tool thermocouple temperature could be processed completely differently from the bottom to the top where the rotation rate increases across the entire build. At the same time the opposite effect can occur where the substrate becomes less diffusive due to geometry and more heat is forced into the tool, lowering the rotation rate until the stir cannot be maintained. This effect has implications for R&D applications as well. Embedded tool thermocouple readings of any kind can only be considered relative to similar geometries and even then, changing process parameters like traversal rate will skew the comparison.

As investigated in Chapter Three as well, more questions about the stick-slip coefficient were raised than answered. Based on the observations: 1) The three-piece tool has radial and rotational conduction asymmetries. 2) For a sliding contact generating heat there must be a zero-jump

temperature condition on the boundary. 3) The tool has four distinct regions that come around every 42ms at 350RPM. The form of the frictional heat generation function is more complex than the linear or simple exponential fits that have been suggested. This is because any given point on the surface, near the outer radius will alternately see a tool sector that is generating heat and sapping it away, quickly followed by one that generates heat without much heat flux into the tool. That point on the stir may experience an oscillatory temperature, with a frequency on the order of twice the rotation rate. At the same time, the actual velocity difference as a function of radius and the radial location where slip begins to occur must be considered. It may even be possible based on the nonlinearity of the material response that material could stick underneath the non-conductive sectors of the tool due to the temperature rise associated with the lack of conduction leading to a decrease in flow stress followed by slipping underneath the more conductive sector. In any case, much more work will need to be done to understand this effect. Questions are also raised about what the metallurgical meaning behind any type of diffused temperature reading might be. If there are large temperature gradients expected large strain gradients will be expected as well. It is understood that the 7xxx series alloys of interest are strain-sensitive so there may be a poorly understood metallurgical effect.

5.4 Structural Repair and Active Cooling

In Chapter Three an extensive body of work studying the AFSD repair of corroded bolt holes was expanded. This was a significant step forward within a multi-year effort. It was found that the shape of the backing used for a repair and its subsequent material flow constraints had little to no effect on the fatigue life or microstructure of the repair. This gives hope that the exact geometric repair strategy is not hugely important to the fatigue life of the repair. At the same time, it was found that by modifying the thermal boundary and applying active cooling at the end of the stir the fatigue life could be improved dramatically over a stir that did not have active cooling. This cooling caused the precipitates to retain a more favorable morphology. Additionally, since the repair spends less time in the thermally active temperature region during cooling, heterogeneous nucleation and grain boundary nucleation are reduced. In addition to the attenuation of some of the intergranular fracture modes, the reduction of heterogeneous nucleation primes the material for an artificial aging step. This aging could be more beneficial for the fatigue life than the 3-month natural age used in this work.

Considering moving this repair to an actual component, the work shown here indicates that thermal generation is a constant with respect to spindle mechanical power, but that input power is a function of the temperature field in a fully coupled manner. To predict the thermal field caused by a repair on a given component, either experimental validation or a fully flushed-out process model would need to be completed. Without either of these things, the true thermal affected zone of the component would not be known and thermal protection like active or passive cooling devices could not be applied with precision. Regardless of this beforehand knowledge, some type of cooling will be necessary to move this to a large component without risking its global properties if no post-deposition heat treatment is applied. If it is determined that a post-repair heat treatment can be applied, then the options for repair strategy and thermal protection open considerably as only areas that see enough shear to force particle coherency loss would be at risk of significant heterogeneous nucleation.

5.5 Future Work

From the results shown here a few key questions are raised on the fundamentals of heat generation within AFSD. What is the function of stick and slip and what process variables affect it? What could this function mean for the temperature distribution of the stir? Can this process be controlled in a meaningful way that allows for the highly repeatable and controlled process necessitated for aerospace use?

To explore these questions, the first research push will need to be focused on the contact state between the tool and the stir. Understanding the stick-slip coefficient and the heat generated by friction will be very important to make good models with physical relevance. If forms of the heat generation function can be estimated, the methods shown in Chapter Three could likely be used as a first-pass filter ruling out functions that don't match the temperature distributions seen in the tool. To consider the second and third questions better constitutive models of the flowing material are needed. Many material models do not properly account for the effects of the large difference in the minimum and maximum strain rates and temperatures that are possible in this process or the rapid softening and loss of heat generation as the material gets closer to melting. These lead to overprediction of the temperature and spurious viscosity fields. Additionally, fluid treatments of the material need to consider the discontinuity presented by yield stress fluids since for a voxel of stirring material on the outside of the stir, at a low total stress, quantities related to it existing as a fluid are no longer well defined. If these questions about the modeling of the flow can be answered and related to metallurgy it may be possible to make the significant advances needed for aerospace use.

On the application-driven repair side of the work, more metallurgy-based questions arise. Can the microstructure be tailored using thermal control? What are thermal bounds for a known good or known bad repair?

These questions may have a somewhat more straightforward answer, and the scope of small-scale repairs provides a more controlled and limited testbed to scale the technology rather than full-scale, from-scratch builds. Driving an understanding of the difference between AFSD precipitation and traditionally processed precipitation forward using position-dependent small angle x-ray scattering (SAXS) is a good candidate for immediate study. A repair could be completed, cooled, placed into ice, and subjected to a SAXS beam with a heated stage. Observing the size distribution of the precipitates through time along with some TEM could answer fundamental questions about the effect of severe plastic deformation processes. Additionally, the effect of the known fatigue life enhancement of engineered residual stress should be applied and studied. This may be a case where the simple addition of a process already used by the Navy may add a significant benefit to the repair.